POLITECNICO DI TORINO

Master's Degree in Aerospace Engineering

Master's Degree Thesis

Preliminary Design and Numerical Validation of a Pintle Injector through 0D Modeling and CFD analysis

Supervisors

PROF. EMANUELE MARTELLI

ING. LEONARDO STUMPO

ING. DOMENICO SIMONE

ING. DOMENICO MOLINARO

Candidate

MARCO BRANCATO

April 2026

Abstract

The current landscape of the New Space Economy dictates the development of cutting-edge propulsion technologies capable of combining high technical performance with a significant reduction in operational costs. Precisely from these stimuli arises the need to investigate in detail the physics governing the pintle injector. This technology is currently the subject of intense study precisely as a function of cost reduction, as it is perfectly suited for next-generation, fully reusable launchers, which require a wide thrust range to utilize the same engines for both the energetic ascent phase and the delicate landing maneuvers. Among the peculiarities of the pintle, the ability to operate with variable geometry stands out, allowing for thrust modulation (throttling) without drastically affecting the complexity of the feed system. The aim of this thesis is to bridge the methodological gap existing between rapid preliminary design and detailed fluid dynamic validation. Following an in-depth investigation into the operating principle of the pintle and the differences compared to other types of launcher injectors, 0D modeling was performed. The development of the numerical 0D model aimed to define the optimal injector geometry starting from thrust requirements and system constraints. A scatter analysis was conducted on geometric parameters to understand their influence on objective quantities such as the Sauter Mean Diameter (SMD), vaporization length, and spray angle. A strongly innovative element of the proposed methodology is the direct integration of convective heat transfer models within the 0D optimization cycle, overcoming the limitations of standard design codes that often neglect thermal loads in the preliminary phase. Specifically, the calculation of thermal loads was modeled by treating the flow on the pintle tip as an impinging jet and assimilating the injector head region to that of a Backward-Facing Step around which the flow recirculates. By leveraging these fluid dynamic analogies and the related empirical correlations (e.g., Katti-Prabhu), it was possible to quantify the heat transfer coefficient based exclusively on geometric and flow initialization parameters. Subsequently, a higher-detail validation was performed via CFD (Computational Fluid Dynamics) simulations using OpenFOAM software. The simulations allowed for an in-depth analysis of the flow behavior inside the pintle injector, evaluating the formation of the central recirculation zone (CRZ), the distribution of pressures and temperatures, as well as the effectiveness of mixing between propellants.

Table of Contents

1 Introduction **1**

1.1 Objectives 2

1.2 Thesis Structure 2

2 The Pintle Injector **5**

2.1 Introduction to the Pintle-Type Injector 5

2.1.1 Overview of Operational Advantages and Technological Limitations 6

2.1.1.1 Strengths of the Architecture 6

2.1.1.2 Critical Challenges and Limitations 6

2.2 Historical and Technical Review of Pintle Engines 7

2.2.1 From Origins to Apollo: The Lunar Module Descent Engine . 7

2.2.2 Scalability and Commercial Applications: From TRW to SpaceX 7

2.2.3 Modern Applications: Lunar Exploration 8

2.3 Injection Mechanics and Spray Formation 8

2.4 The Crucial Role of Recirculation Zones 9

2.5 Extensive Throttling Capability 10

2.5.1 Variable Area Injector Mechanism 10

2.5.2 Kinematic Movement Architectures 11

2.5.3 Actuation Technologies 12

2.5.3.1 Electromechanical Actuation 12

2.5.3.2 Integrated Hydraulic Actuation (Fuel-draulics) . . . 12

2.5.4 Quantitative Performance Analysis 13

2.5.5 Comparison with the limitations of fixed-area injectors 13

2.6 Design Simplicity, Reliability, and Reduced Costs 14

2.6.1 Single-Element vs. Multi-Element Philosophy 14

2.6.2 Impact on Production and Development 15

2.6.3 Proven In-Flight Reliability 15

2.7 Thermal Management: Overheating and Ablation of the Pintle Tip . 16

2.8 Propellant Selection: Gaseous Methane and Liquid Oxygen 16

2.9 Geometric Characterization 17

2.9.1 Pintle Diameter (D_p) 17

2.9.1.1 Influence on Stability 17

2.9.1.2 Design Correlations 18

2.9.2 Tip Diameter (D_{pt}) and Profile 18
2.9.2.1 Tip Geometry 18
2.9.2.2 Thermal Integrity 19
2.9.3 Annular Gap (δ_{ann}) 19
2.9.4 Radial Inlet Configuration 19
2.9.4.1 Parameters and Aspect Ratio 20
2.9.4.2 Multiple Row Arrangement 20
2.9.4.3 Circular Holes and Penetration 20
2.9.5 Skip Distance (L_s) 20
2.10 Analysis of Dimensionless Parameters 21
2.10.1 Blockage Factor (BF) 21
2.10.1.1 Atomization Regimes 21
2.10.2 Total Momentum Ratio (TMR) 21
2.10.2.1 Definition and Spray Angle 22
2.10.2.2 Optimal TMR: Gas-Liquid vs Liquid-Liquid 22
2.10.3 Local Momentum Ratio (LMR): Definition and Importance . 22
2.10.4 Experimental Analysis: Study by Jin et al. (2022) 22
2.10.4.1 Decoupling of the Discharge Coefficient (C_d) 22
2.10.4.2 Mixing Optimization and Spray Angle 23
2.11 Summary of Key Parameters 23

3 Theoretical Background 24
3.1 Fundamentals of Gasdynamics and Rocket Propulsion Physics 24
3.1.1 Thermodynamics of the Ideal Rocket Engine 24
3.1.1.1 Thrust Generation and Specific Impulse 25
3.1.2 Dimensionless Performance Parameters: c^* and C_F 26
3.1.2.1 The Characteristic Velocity (c^*) 26
3.1.2.2 The Thrust Coefficient (C_F) 27
3.1.3 Mass Flow Derivation via Mixture Ratio (O/F) 27
3.1.3.1 Thermochemical Analysis 27
3.1.3.2 Selection of Optimal O/F and Mass Flow Calculation 28
3.1.3.3 Design Flow Splitting 28
3.2 Atomization Physics and Sauter Mean Diameter (SMD) 29
3.2.1 The Concept of Sauter Mean Diameter (D_{32}) 29
3.2.2 Breakup Mechanisms and Weber Number 30
3.2.3 Empirical Correlations for Pintle Injectors: The Min Son Model 30
3.2.4 Vaporization Physics: The Classical D^2 Law 31
3.2.4.1 Physical Interpretation of the Spalding Number . . 31
3.2.5 Vaporization Distance Model (Modified D^2 Law) 32
3.3 Optimization Theory: Convex Quadratic Programming (CQP) . . . 33
3.3.1 The Role of Scatter Analysis 33
3.3.2 Mathematical Foundations of CQP 33

4 Design Methodology and Numerical Analysis **34**
4.1 Research Objectives and Code Architecture 34
4.2 Preliminary Design and 0D Model 35
4.2.1 Thermodynamic Fundamentals and Basic Assumptions 35
4.2.2 Iterative Thermochemical Sizing Procedure (CEA) 35
4.2.2.1 Phase 1: Nominal Point and Nozzle Geometry . . . 35
4.2.2.2 Phase 2: Iterative Loop for Off-Design Analysis . . 35
4.2.2.3 Final Results and Flow Rate Calculation 36
4.2.3 Injection Velocity Calculation and Initial Geometry 36
4.3 Performance Analysis via Scatter Analysis 37
4.3.1 Design Space Exploration 37
4.3.2 Empirical Atomization Models (SMD) 37
4.3.3 Vaporization Modeling (X_{vap}) 37
4.3.4 Spray Angle Modeling 37
4.3.5 Scatter Analysis Results 38
4.3.5.1 Effect of Pintle Angle 38
4.3.5.2 Effect of Annular Pressure Drop 40
4.3.5.3 Effect of Pintle Pressure Drop 42
4.3.5.4 Effect of Pintle Diameter 43
4.4 Thermal Model Integration (h_c) 45
4.4.1 Pintle Tip: Katti-Prabhu Correlation 46
4.4.2 Heat Transfer Models in the Three Zones 46
4.4.2.1 Scatter Analysis Results on hc 48
4.5 Multi-Objective Optimization and 3D Visualization 50
4.5.1 Convex Quadratic Programming (CQP) 50
4.5.2 Optimization Philosophies 51
4.5.3 Sensitivity Analysis in Weight Space 51
4.5.3.1 3D Visualization Results 51
4.5.3.1.1 Impact on Spray Angle 51
Impact on Spray Angle 51
4.5.3.1.2 Impact on SMD 53
Impact on SMD 53
4.5.3.1.3 Impact on Xvap 55
Impact on Xvap 55
4.5.4 Optimization Results for the Baseline Philosophy 57

5 Numerical Modeling of Two-Phase Flows **59**
5.1 Theoretical Framework for Spray Modeling 59
5.2 The Eulerian-Lagrangian Model 60
5.2.1 Governing Equations 61
5.2.1.1 Turbulence Modeling 64
5.2.2 Droplet Dynamics 65
5.2.3 Droplet Vaporization Model: D^2 Law 66

5.2.4 Momentum Source Term 68
5.2.5 Energy Source Term 69

6 CFD Simulation and Heat Transfer Analysis 70
6.1 CFD Modeling Strategy 70
6.2 Computational Domain and Geometry 71
6.3 Boundary Conditions 72
6.4 Mesh Sensitivity Study 72
6.5 Flow Field Analysis 73
6.5.1 Design variables comparison 75
6.6 Heat Flux Evaluation 77
6.6.1 Extraction of Wall Quantities 77
6.6.2 Heat Flux Model Based on Turbulent Wall Laws (Han & Reitz) 77
6.6.3 Analysis of the Heat Flux Distribution Predicted by the Han-Reitz Model 78
6.6.4 Jet Impingement Heat Transfer Model (Katti–Prabhu) 81
6.6.5 Heat Flux Model Comparison 81
6.6.6 Parameter Fitting and Model Validation 84
6.6.7 Influence of Mesh Resolution on Heat Flux Fitting 85
6.6.8 Discussion and Key Findings 87

7 Conclusions 89

A Appendix A 91
A.1 Summary of Pintle Engine Characteristics 91

B Appendix B 93
B.1 Finite Volume Method 93
B.1.1 Solution Algorithms 94

Bibliography 97

List of Figures

1.1 Pintle scheme [1] 1

2.1 Pintle injector [2] 5
2.2 Shower injector [3] 5
2.3 jet structure [9] 9
2.4 Vortex structure [10] 10
2.5 LMDE pintle injector scheme [12] 11
2.6 variable thrust LRE IFRGG[13] 13
2.7 pintle geometric section [17] 17
2.8 Shortened LOX passage and reduced skip ratio [20] 18
2.9 Active cooling system incorporated for pintle tip[20] 18
2.10 Deflector for displacement of the impingement point[20] 18
2.11 Deflector and a cooled pintle tip [20] 19
2.12 Canted slot configuration[18] 19
2.13 Sawtooth configuration[18] 20
2.14 three different blockage factor[23] 21

3.1 break-up scheme[27] 29
3.2 break up models examples[28] 30

4.1 pintle angle [17] 38
4.2 Sauter Mean Diameter (SMD) as a function of the pintle angle (θ_{pt}). 38
4.3 Vaporization distance (X_{vap}) as a function of the pintle angle [deg] (θ_{pt}). 39
4.4 Spray angle as a function of the pintle angle (θ_{pt}). 39
4.5 Sauter Mean Diameter (SMD) as a function of the annular pressure drop. 40
4.6 Vaporization distance (X_{vap}) as a function of the annular pressure drop. 41
4.7 Spray angle as a function of the annular pressure drop. 41
4.8 Sauter Mean Diameter (SMD) as a function of the pintle pressure drop. 42
4.9 Vaporization distance (X_{vap}) as a function of the pintle pressure drop. 42
4.10 Spray angle as a function of the pintle pressure drop. 43
4.11 pintle diameter [17] 43
4.12 Sauter Mean Diameter (SMD) as a function of the pintle diameter (D_{pt}). 44
4.13 Vaporization distance (X_{vap}) as a function of the pintle diameter (D_{pt}). 44
4.14 Spray angle as a function of the pintle diameter (D_{pt}). 45

4.15 temperature field on the pintle tip [31] 45
4.16 Katti and Prabhu experimental setup [32] 46
4.17 three zones of heat transfer [32] 46
4.18 backward facing step flow [33] 47
4.19 Sensitivity of hc to variations in pintle diameter 48
4.20 Sensitivity of hc to variations in annular pressure drop 48
4.21 Sensitivity of hc to variations in pintle angle 49
4.22 Sensitivity of hc to variations in pintle pressure drop 49
4.23 optimizer logic [17] 50
4.24 spray angle solution space fixing the weight of α [17] 52
4.25 spray angle solution space fixing the weight of SMD [17] 52
4.26 spray angle solution space fixing the weight of X_{vap} [17] 53
4.27 SMD solution space fixing the weight of α [17] 54
4.28 SMD solution space fixing the weight of SMD [17] 54
4.29 SMD solution space fixing the weight of X_{vap} [17] 55
4.30 X_{vap} solution space fixing the weight of α [17] 56
4.31 X_{vap} solution space fixing the weight of SMD [17] 56
4.32 X_{vap} solution space fixing the weight of X_{vap} [17] 57

5.1 Schematization of flow regimes in a spray and the primary and secondary atomization process [34] 61
5.2 scheme of forces, mass and heat exchanged at a liquid-gas interface [34] 66

6.1 Computational fluid domain used in the CFD simulations 71
6.2 pintle body detail (in grey) and oxygen inlet (in blue) 71
6.3 mesh detail comparison: coarse (top), intermediate (center), and fine (bottom) 73
6.4 $\overline{CH_4}$ mass fraction distribution 73
6.5 $\overline{O_2}$ mass fraction distribution 74
6.6 $\overline{OH}$ mass fraction distribution 74
6.7 $\overline{T}$ distribution 74
6.8 Streamlines colored by axial velocity $\overline{U_x}$ 74
6.9 $\overline{p}$ distribution 75
6.10 Spray envelope extracted from CFD parcels and linear fitting used to estimate the spray half-angle. 76
6.11 Heat flux predicted by Han-Reitz model 78
6.12 temperature field near step 79
6.13 density field near step 79
6.14 temperature field near the chamber symmetry axis 80
6.15 density field near the chamber symmetry axis 80
6.16 Heat flux comparison between the Han–Reitz formulation and the Katti–Prabhu model before parameter fitting 82
6.17 Local error distribution between the Katti-Prabhu model and the CFD-based Han-Reitz heat flux before parameter fitting 82

6.18 Heat flux comparison after calibration of the Katti-Prabhu model parameters 83
6.19 Local error distribution after parameter fitting 83
6.20 a1 coefficient of Katti and Prabhu model linear fitting 84
6.21 b1 coefficient of Katti and Prabhu model linear fitting 84
6.22 heat flux comparison on pintleTip with an isothermal temperature on pintle tip of 950K 85
6.23 heat flux comparison on pintleTip with finer mesh 86
6.24 error percentage between the two model after fitting with finer mesh 86

B.1 SIMPLE Algorithm Flowchart [38] 95
B.2 PISO Algorithm Flowchart [38] 95
B.3 PIMPLE Algorithm Flowchart [38] 96

List of Tables

2.1 Summary of Key Parameters 23

4.1 Results of thermochemical sizing at various throttling levels (including C^*). 36
4.2 Optimization philosophies considered in the design procedure 51
4.3 Main injector parameters obtained from the baseline optimization philosophy 58

5.1 Classification of flow regimes for sprays as a function of volumetric fraction. 61

6.1 Comparison between CFD results and 0D model predictions for key spray parameters 76

A.1 Detailed comparison of engines based on Pintle Injector technology. . 92

Acronyms

BF	Blockage Factor.
CEA	Chemical Equilibrium with Applications.
CFD	Computational Fluid Dynamics.
CQP	Convex Quadratic Programming.
FSO	Face Shutoff Only.
FVM	Finite Volume Method.
GCH_4	Gaseous Methane.
IFRGG	Integrated Flow Regulator/Gas Generator.
LH_2	Liquid Hydrogen.
LMDE	Lunar Module Descent Engine.
LMR	Local Momentum Ratio.
LNG	Liquified Natural Gas.
LOX	Liquid Oxygen.
LRE	Liquid Rocket Engine.
LVDT	Linear Variable Differential Transformer.
MMH	Monomethylhydrazine.
MON	Mixed Oxides of Nitrogen.
NASA	National Aeronautics and Space Administration.
PDE	Partial Differential Equation.
PIMPLE	PISO-SIMPLE Hybrid Method.
PISO	Pressure-Implicit with Splitting of Operators.
PWM	Pulse Width Modulation.
RANS	Reynolds-Averaged Navier-Stokes.
RP-1	Rocket Propellant-1 (Refined Kerosene).

SIMPLE	Semi-Implicit Method for Pressure-Linked Equations.
SIMPLEC	SIMPLE-Consistent.
SMD	Sauter Mean Diameter (D_{32}).
TMR	Total Momentum Ratio.

Nomenclature

Symbol	Description
A	Cross-sectional area
A_e	Nozzle exit section area
A_t	Nozzle throat area
B	Spalding transfer number
B_M	Spalding mass transfer number
c^*	Characteristic velocity
C_d	Discharge coefficient or drag coefficient
C_F	Thrust coefficient
c_p	Specific heat at constant pressure
c_v	Specific heat at constant volume
D	Generic diameter
$\mathcal{D}$	Effective diffusion coefficient
D_{32}	Sauter Mean Diameter (SMD)
D_p	Pintle diameter (central post)
D_{pt}	Pintle tip diameter
E	Specific total energy
e	Specific internal energy
F	Engine thrust
g_0	Standard gravitational acceleration
h	Specific enthalpy
h_c	Convective heat transfer coefficient
h_{fg}	Latent heat of vaporization
I_{sp}	Specific impulse
J	Cost function (optimization) or Diffusive flux
k	Thermal conductivity
K_{vap}	Vaporization constant
L_{open}	Pintle opening distance
L_s	Skip Distance
m	Mass
$\dot{m}$	Mass flow rate
Nu	Nusselt number
O/F	Mixture ratio (Oxidizer/Fuel)

Symbol	**Description**
p	Pressure
p_c	Combustion chamber pressure
Pr	Prandtl number
q	Dynamic pressure or Heat flux
R	Specific gas constant
Re	Reynolds number
S	Generic source term
Sc	Schmidt number
t	Time
T	Temperature
$\mathbf{u}$	Velocity vector
V	Volume
We	Weber number
w_{slot}	Slot width
X_{vap}	Vaporization distance
Y	Mass fraction
z/d	Dimensionless jet-to-plate distance
α	Radial jet inclination angle or thermal diffusivity
Γ	Generic diffusivity coefficient
γ	Specific heat ratio (c_p/c_v)
δ_{ann}	Annular gap thickness
ϵ	Nozzle expansion ratio (A_e/A_t)
θ	Spray angle
θ_{pt}	Pintle tip angle
μ	Dynamic viscosity
ξ	Geometric factor in Min Son model
ρ	Density
σ	Surface tension
τ	Viscous stress tensor
τ_d	Droplet response time
Φ	Volumetric fraction
ϕ	Generic scalar quantity (transport eq.)
ω	Chemical reaction rate

Chapter 1

Introduction

This thesis work is the result of a collaboration between the Polytechnic of Turin and Avio S.p.A., and is situated within the context of scientific research aimed at modeling pintle-type injectors for space propulsion. The current landscape of the aerospace industry has been radically transformed by the advent of the New Space Economy and the entry of private actors—most notably SpaceX—who have imposed a drastic reduction in the costs of access to space. This reduction has been made possible primarily through the paradigm shift introduced by reusable launchers. The reusability strategy imposes stringent requirements on the propulsion system: to allow for the controlled reentry and vertical landing of the first stage, the engine must guarantee extremely high deep throttling capabilities while maintaining combustion stability even at throttled regimes. It is in this context that the pintle injector has demonstrated its technological superiority and versatility.

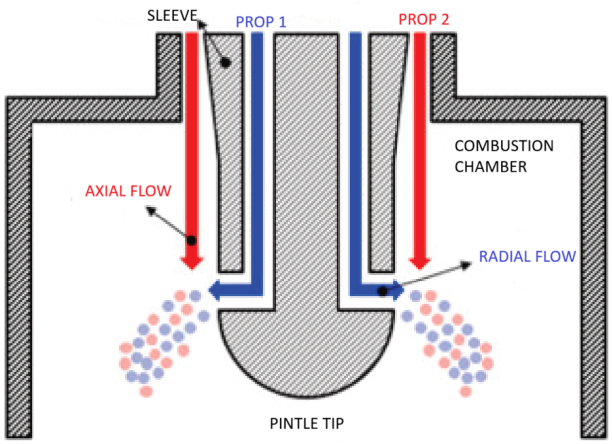

Figure 1.1: Pintle scheme [1]

The injector is a fundamental device designed to mix two distinct fluids and atomize them into extremely small particles. This atomization process is intended to maximize the contact surface between reactants, a necessary condition for ensuring efficient and stable combustion [1].

Unlike traditional injection schemes (such as impinging or coaxial types), the

pintle injector allows for the geometric variation of the outflow area while maintaining excellent atomization and stability characteristics, which are fundamental for reentry maneuvers. The most emblematic example of this application is represented by the Merlin engine family, used on Falcon 9 launchers. The choice of this architecture for the Merlin engine is dictated not only by its performance in terms of throttleability but also by the intrinsic constructive simplicity and robustness of the pintle. These factors further contribute to the reduction of production and maintenance costs, aligning perfectly with the philosophy of low cost and high reliability.

Despite the proven operational success of such systems, the need to investigate the physics governing the pintle injector arises from the necessity to bridge the existing gap between theoretical predictive models and experimental evidence. Currently, accurately predicting the operational behavior of this component represents a complex and non-trivial challenge. This work is founded on a critical analysis of the existing literature, with the objective of extending its results and providing a more comprehensive overview. In the current scenario, the aerospace industry increasingly requires the aid of low-cost predictive models to guide design, reducing reliance on experimental campaigns that entail significant economic burdens. This is made possible by the evolution of computational capabilities, which have recorded substantial progress over the last twenty years. However, while numerical simulation allows for a reduction in experimental costs, it requires considerable computational resources. In this context, it becomes fundamental to complement reduced-order models (simple and fast) with high-fidelity models capable of investigating three-dimensional and coupled phenomena that escape the simplifications of 0D or 1D models. The focus of this thesis will be specifically directed towards the estimation of thermal loads, with the intent of developing efficient methodologies that can provide key indications for the design and optimization of the injector.

1.1 Objectives

The primary objective of this thesis is the identification of the optimal geometric configuration capable of satisfying the stringent system requirements imposed. The adopted methodology involves the use of models of increasing complexity in order to progressively reach a higher level of accuracy. This approach allows for the evaluation of the trade-off between computational costs and result fidelity, ensuring consistent estimates compatible with the physical limits of the analyzed models.

1.2 Thesis Structure

This thesis work is organized into six chapters, supplemented by a technical appendix, which follow the logical flow of the injector design: from the definition of requirements to preliminary modeling, up to detailed fluid dynamic analysis.

- Chapter 1 introduced the reference scenario, describing the industrial collabo-

ration and the scientific motivations underlying the research, with particular emphasis on the need for efficient predictive tools in the context of the New Space Economy.

- Chapter 2 provides the theoretical and technological background. The architecture of the pintle injector is analyzed, describing the flow physics, recirculation zones, and operational advantages such as intrinsic stability. A specific section is dedicated to justifying the choice of the LOX-GCH4 propellant pair, highlighting its advantages in terms of reusability and performance for the application under examination.

- Chapter 3 examines the equations of an ideal rocket, starting from the fundamental laws of thermodynamics and fluid mechanics. Furthermore, the main performance parameters of a pintle injector are presented.

- Chapter 4 describes the 0D modeling and preliminary sizing. The inverse design approach (from thrust to geometry) is presented, along with the sensitivity analysis (scatter plots) used to evaluate the influence of geometric parameters on SMD, spray angle, and vaporization length. A characterizing element of this chapter is the integration of an original thermal model for the pintle tip: the calculation of the convective heat transfer coefficient is detailed by combining empirical correlations for impinging jets (Katti-Prabhu) and fluid dynamic analogies with the backward-facing step.

- Chapter 5 illustrates the mathematical and physical framework for the CFD simulation of two-phase flows. The governing equations for the discrete phase (Lagrangian) and continuous phase (Eulerian) are discussed, focusing on the modification of the Navier-Stokes equations through the introduction of source terms to account for the exchange of mass, momentum, and energy between liquid and gas.

- Chapter 6 presents the CFD simulation and the thermal analysis of the injector. Higher-fidelity simulations performed in OpenFOAM are used to characterize the internal flow field, highlighting the mixing process between methane and oxygen and the formation of recirculation structures responsible for flame stabilization. The numerical results are employed to extract the quantities required for the evaluation of wall heat transfer using the Han–Reitz turbulent wall heat transfer formulation. The resulting heat flux distribution is then used as a reference dataset to calibrate a simplified engineering model based on the Katti–Prabhu correlation. The chapter also investigates the influence of mesh resolution on the accuracy of the predicted heat flux and demonstrates how CFD simulations can be used to develop computationally efficient reduced-order thermal models for preliminary injector design.

- Conclusions summarize the main outcomes of the thesis, highlighting the integration between simplified analytical models and higher-fidelity CFD simu-

lations for the design and thermal assessment of pintle injectors. The chapter discusses the main findings related to spray behavior, flow structures, and heat transfer prediction, emphasizing the development of a computationally efficient reduced-order thermal model calibrated using CFD data.

- Appendix A reports a table of the main engines equipped with a pintle injector and their main technical characteristics.
- Appendix B reports the Navier-Stokes equations in conservative form and specific details regarding the solvers and numerical schemes used in OpenFOAM.

Chapter 2

The Pintle Injector

2.1 Introduction to the Pintle-Type Injector

The pintle-type injector distinguishes itself from traditional configurations by its unique propulsive architecture, characterized by a centralized geometric design and a reduced number of components. The operating principle involves a central body inside which the first propellant flows; this is diverted radially by the geometry of the tip (pintle tip) before entering the combustion chamber, where it impacts the second propellant injected through an external annular ring.

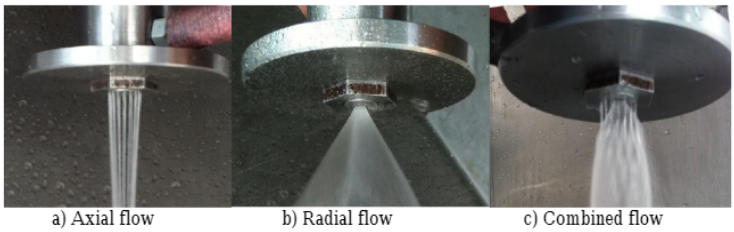

Figure 2.1: Pintle injector [2]

This configuration contrasts sharply with conventional injectors, which consist of a multitude of elements distributed over the entire surface of the injection plate (faceplate). The latter require extremely tight manufacturing tolerances and complex design to ensure flow uniformity and prevent combustion instabilities.

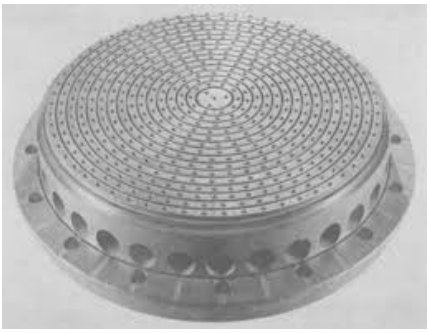

Figure 2.2: Shower injector [3]

The pintle injector has been studied and tested for over 40 years by TRW (now Northrop Grumman). During this period, multiple engines with pintle-type injectors have been developed, ranging from 5lbf thrusters to 650,000 lbf booster engines. A fundamental fact attesting to the reliability of this configuration is the absolute absence of in-flight failures or combustion instabilities, despite scalability over a thrust range of 50,000:1. [4]

2.1.1 Overview of Operational Advantages and Technological Limitations

The adoption of the pintle injector is motivated by a series of intrinsic advantages that resolve historical problems of liquid rocket engines, while introducing specific engineering challenges that require careful consideration.

2.1.1.1 Strengths of the Architecture

The enduring popularity and recent rediscovery of the pintle by "New Space Economy" actors (such as SpaceX with the Merlin engine) derive from four fundamental pillars that make it superior to conventional alternatives in specific mission scenarios:

1. **Efficient Atomization:** the geometric collision mechanism guarantees effective propellant breakup even at relatively low injection pressures.
2. **Intrinsic Stability:** unlike flat-face injectors, which often require baffles or acoustic chambers to dampen combustion instabilities, the pintle demonstrates natural resistance to these phenomena thanks to its recirculation macrostructures.
3. **Throttling Capability:** the ability to vary the outflow geometry allows for deep thrust adjustments (up to ratios of 10:1 or higher) while maintaining high efficiency, a characteristic almost impossible to replicate with fixed-orifice injectors without incurring instabilities.
4. **Manufacturing Simplicity:** the drastic reduction in the number of components and the absence of hundreds of tight tolerances lower production costs and assembly times.

2.1.1.2 Critical Challenges and Limitations

Despite the apparent mechanical simplicity, the physics governing the pintle injector is complex and presents two main limitations that have historically slowed its diffusion outside of specific applications:

- **Localized Thermal Load on the Pintle Tip:** the formation of a high-temperature central recirculation zone results in an intense heat flux directed against the injector tip, requiring advanced thermal management solutions to prevent structural damage.

- **Complexity in Predictive Modeling:** the three-dimensional and turbulent nature of the flow makes accurate simulation via CFD difficult, often forcing an iterative experimental approach for design optimization.

2.2 Historical and Technical Review of Pintle Engines

The history of the pintle injector is marked by milestones that have demonstrated its extraordinary versatility, ranging from delicate lunar landing maneuvers to modern heavy commercial launchers. The evolution of this technology highlights how the pintle design has succeeded in adapting to extremely different thrust scales and propellants, maintaining stability and controllability characteristics intact.

2.2.1 From Origins to Apollo: The Lunar Module Descent Engine

The archetype of the pintle engine is represented by the Lunar Module Descent Engine (LMDE), developed by TRW for the Apollo program with the critical objective of ensuring a soft landing on the lunar surface [5]. The fundamental characteristic required for such a mission was a deep throttling capability, with a 10:1 ratio, which allowed the engine to vary thrust from a maximum of 10500 lbf down to about 1050 lbf. The technical solution adopted involved a mechanical coupling capable of moving a sleeve on the injector and, simultaneously, regulating cavitating valves placed upstream. This mechanism ensured that the mixture ratio and the total momentum ratio (TMR) remained constant throughout the entire flight envelope, using hypergolic propellants such as N_2O_4 and Aerozine 50. The peculiarity of the LMDE is defined by its absolute reliability: it never failed an operational ignition and was decisive as an emergency engine for the crew rescue during the Apollo 13 crisis.

2.2.2 Scalability and Commercial Applications: From TRW to SpaceX

The demonstration that pintle technology could compete with large first-stage engines came in 2000, when TRW developed the TR-106 as part of NASA's Space Launch Initiative [6]. Powered by LOX/LH_2, this engine delivered a thrust of 650000 lbf (2892 kN), positioning itself among the most powerful thrusters ever built. The TR-106 proved the linear scalability of the injector: a single pintle element was able to handle massive flows that, with conventional technologies, would have required thousands of coaxial elements, also allowing the use of economical ablative cooling. This technological heritage was subsequently acquired and perfected by SpaceX for the Merlin engine family. The Merlin evolved from the ablative version 1A to the regenerative 1D. The Merlin 1D, with a thrust of approximately 845 kN at sea level and a specific impulse (I_{sp}) of 311 s in vacuum, exploits the pintle's throttling capability (down to 40% of nominal thrust) to execute the complex reentry and vertical landing maneuvers of the Falcon 9 first stage [7]. In parallel, the versatility

of the pintle on a smaller scale was demonstrated by the Kestrel engine of the Falcon 1 second stage, an ablatively cooled pressure-fed unit.

2.2.3 Modern Applications: Lunar Exploration

In the context of robotic exploration, the Chinese Chang'e lunar missions (3, 4, and 5) have adopted a variable thrust main engine based on pintle technology. This thruster, with a maximum thrust of 7500 N modulatable down to 1500 N (ratio 5:1), leverages the precision of the pintle flow control system for fine adjustments in the order of 7.5 N, a specification essential for autonomous obstacle avoidance systems during lunar landing [8].

2.3 Injection Mechanics and Spray Formation

The fundamental operating principle of the pintle-type injector is based on the high-energy collision between the axial flow (coming from the annular duct) and the radial flow (diverted by the pintle). This impact, which usually occurs at an angle of 90 degrees, generates intense shear forces that fragment the liquid flows into an aerosol of extremely fine droplets, a process known as atomization. Effective atomization is a prerequisite for rapid vaporization and subsequent complete and efficient combustion. The macroscopic result of this collision is the formation of a characteristic hollow spray cone that propagates inside the combustion chamber. The effectiveness of this process is quantified by key parameters. The first is the Sauter Mean Diameter (SMD), a metric representing the average droplet size weighted by the volume/surface ratio; lower SMD values indicate finer atomization and are generally desirable. The second is the vaporization distance, i.e., the space necessary for liquid droplets to transition to the gaseous state; a shorter distance allows for faster mixing and a longer residence time for chemical reactions. The non-dimensional parameter that predominantly governs the spray geometry, and in particular its opening angle, is the Total Momentum Ratio (TMR). This ratio, defined as the ratio between the momentum of the radial flow and that of the axial flow, determines the balance of forces at impact and, consequently, the trajectory of the atomized droplets. Precise control of the TMR is therefore essential to optimize propellant distribution in the chamber and maximize combustion efficiency.

$$TMR = \frac{\dot{m}_r \cdot v_r}{\dot{m}_a \cdot v_a} \tag{2.1}$$

Where:

- $\dot{m}_r$ is the mass flow rate of the radial flow
- v_r is the velocity of the radial flow
- $\dot{m}_a$ is the mass flow rate of the axial flow
- v_a is the velocity of the axial flow

The resulting spray angle (θ) can be correlated to the TMR through empirical relationships derived from experimental data. One of these relationships, proposed by Cheng [9], is expressed as:

$$\frac{\theta}{2} = \cos^{-1}\left(\frac{1}{1+TMR}\right) \tag{2.2}$$

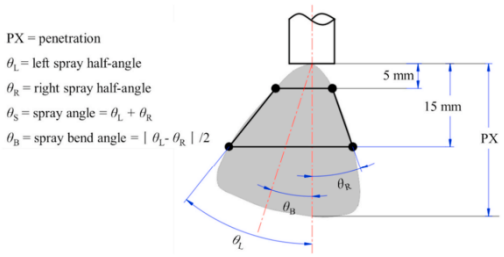

Figure 2.3: jet structure [9]

This equation highlights how an increase in TMR leads to a wider spray angle, favoring better propellant distribution in the combustion chamber. However, it is important to note that TMR optimization must be balanced with other design factors, such as combustion stability and the thermal characteristics of the injector. An in-depth analysis of these parameters is essential for the design of efficient and reliable pintle injectors capable of meeting the specific needs of modern aerospace applications.

2.4 The Crucial Role of Recirculation Zones

A distinctive and fundamental aspect of the pintle injector's operation is the formation of recirculation zones within the combustion chamber. These areas, characterized by swirling and turbulent flows, play a crucial role in ensuring combustion stability and propulsion process efficiency. Recirculation zones form due to the particular geometry of the injector and the dynamics of the flows involved. When propellants are introduced into the combustion chamber, their interaction generates low-pressure regions where the flow tends to return towards the injector. Recirculation zones offer several operational advantages:

- **Combustion Stability**: the recirculation zones help maintain a stable flame, reducing the risk of instabilities that could compromise engine performance.
- **Improved Mixing**: the swirling flows favor more effective mixing between propellants, increasing the contact surface and facilitating complete combustion.

In particular, two main recirculation zones can be distinguished:

- **Core Recirculation Zone:** this zone forms immediately downstream of the pintle tip, along the central axis of the engine. It is dominated by the

radially injected propellant and hot combustion gases. Its primary function is to significantly increase the residence time of propellants in the primary reaction region. The droplets are trapped in this vortex, ensuring they have sufficient time to vaporize and mix completely, which leads to very high combustion efficiency. However, this same zone of stagnant hot gases is the main cause of the severe thermal load on the pintle tip, one of the main design challenges of this technology.

- **Mantle Recirculation Zone:** this second toroidal zone is located in a more external position, near the combustion chamber wall and the injector face. It is predominantly rich in the axially injected propellant. This zone acts as a protective thermal "shield". Cold, unburnt propellant droplets are dragged into this region, where they evaporate upon contact with hot surfaces, absorbing heat and effectively cooling both the injector head and the chamber walls.

These two large recirculation zones act as dampers for dangerous pressure perturbations that could otherwise degenerate into combustion instabilities. Their presence is an intrinsic characteristic of the pintle injector, contributing significantly to its reputation as a highly stable and reliable system for critical space applications.

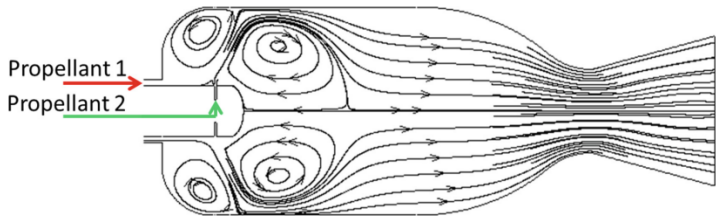

Figure 2.4: Vortex structure [10]

2.5 Extensive Throttling Capability

One of the most celebrated and strategically important features of the pintle-type injector is its exceptional ability to regulate engine thrust over a wide range, a process known as throttling. This capability is not a simple incremental improvement, but an enabling factor that unlocks mission profiles and operational capabilities otherwise impossible to realize with conventional injection architectures. [11]

2.5.1 Variable Area Injector Mechanism

The throttling capability of the pintle derives from its conception as a variable area injector. This is achieved by designing one of its key components, typically the pintle itself or a cylindrical sleeve surrounding it, as a movable part. An actuator, which can be mechanical or hydraulic, controls the axial displacement of this movable component. By moving, it modifies the size of the slot (or slots) through which one or both propellants are injected. By varying the injection area, it is possible to alter the mass flow rate of the propellants and, consequently, the thrust generated by the engine.

The crucial aspect of this mechanism is that it allows for maintaining a sufficiently high pressure drop (ΔP) across the injector even when the flow rate is drastically reduced. This ΔP is fundamental for preserving the kinetic energy necessary for good atomization and mixing, thus ensuring stable and efficient combustion even at the lowest thrust levels. In some particularly advanced configurations, it is possible to implement the FSO (Face Shutoff Only) functionality, i.e., the ability to interrupt propellant flow directly at the injector face [4].

2.5.2 Kinematic Movement Architectures

There are two main kinematic configurations for achieving area variation, each with specific design implications:

- **Movable Sleeve:** in this configuration, made famous by the *Lunar Module Descent Engine* (LMDE) of the Apollo program, the central body (*post*) remains fixed, while an external cylindrical sleeve slides axially over it.
  - Advantage: the movement of the sleeve can simultaneously vary both the effective height of the radial slots (central flow) and the section of the annular gap (external flow), if the parts are shaped in a coordinated manner.
  - *LMDE Example:* the sleeve was mechanically connected to the flow regulation valves (*cavitating venturis*) via an actuation arm ("throttle arm"). This rigid mechanical connection ensured that the mixture ratio remained constant during thrust transients[12].

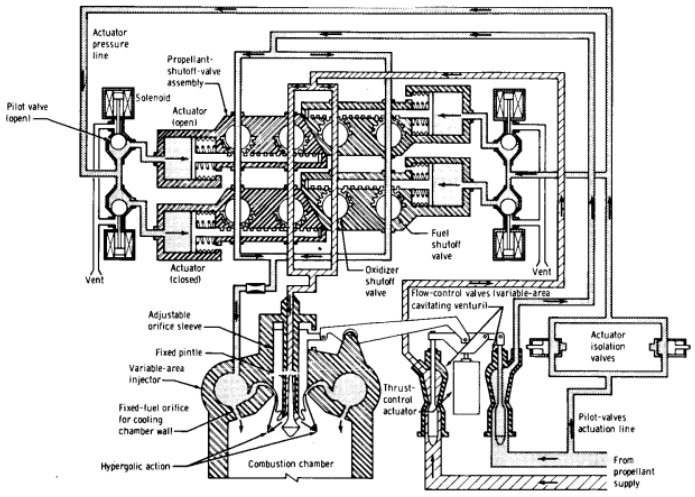

Figure 2.5: LMDE pintle injector scheme [12]

- Movable Central Pintle: the central body itself moves axially relative to a fixed external seat.

2.5.3 Actuation Technologies

The force required to move the movable element must overcome fluid dynamic loads (propellant pressure), seal friction, and inertial forces.

2.5.3.1 Electromechanical Actuation

Electric motors (DC or stepper) coupled to worm screws or jacks are used to convert rotary motion into linear translation. This is the system used in the LMDE.

2.5.3.2 Integrated Hydraulic Actuation (Fuel-draulics)

In more advanced architectures, oriented towards mass reduction and high dynamic response (as in modern landers or IFRGG systems - *Integrated Flow Regulator/Gas Generator*), electromechanical actuation is replaced by servo-assisted systems that use the rocket propellant itself as the working fluid. This approach is often defined as *fuel-draulic*.

- **Force Balance Principle:** in this configuration, the pintle is not rigidly constrained to a mechanical actuator, but acts as a "floating" piston. Its axial position is determined by the dynamic equilibrium between fluid dynamic forces acting on the injector head (generated by combustion pressure, P_{gg}) and a control pressure (P_c) modulated in a rear chamber located behind the pintle.
- **PWM and Control:** the regulation of the control pressure P_c is not achieved via heavy hydraulic pumps, but by bleeding a fraction of high-pressure propellant and modulating its entry into the control chamber via high-speed solenoid valves managed by PWM (*Pulse Width Modulation*). By varying the duty cycle of the valve, the system alters the pressure acting on the back of the pintle, forcing its displacement towards a new equilibrium position.
- **Feedback and Performance:** since the fluid is subject to non-linearities, precise control requires a closed-loop based on linear position sensors (LVDT) integral to the pintle. Recent studies on these integrated architectures demonstrate excellent response capabilities, with settling times of less than 0.3 s for the full excursion and stable chamber pressure control with limited overshoot (within $\pm 3\%$), eliminating the need for heavy electric motors and simplifying the overall engine design[13].

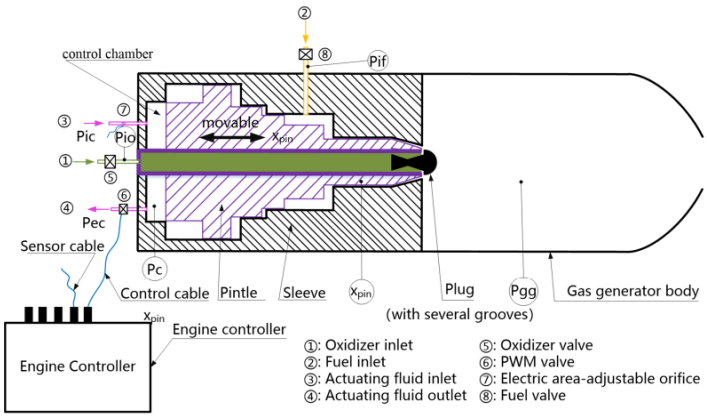

Figure 2.6: variable thrust LRE IFRGG[13]

2.5.4 Quantitative Performance Analysis

The throttling performance demonstrated by engines based on pintle injectors is remarkable and far exceeds that of fixed-area injectors. Historical and modern examples highlight the scope of this capability:

- The Apollo Lunar Module Descent Engine (LMDE), the first crewed engine to use a pintle, had a throttling ratio of 10:1, allowing it to go from a maximum thrust of about 45 kN to a minimum of 4.5 kN for precision lunar landing. [5]
- An engine developed by TRW (now Northrop Grumman Corporation) for the US Army's SENTRY program demonstrated an exceptional throttling ratio of 19:1, also capable of executing very short pulses of only 8 milliseconds at any thrust level. [4]

This operational flexibility is indispensable for a vast range of aerospace applications. Planetary landers require the ability to brake from high speeds, slow down, hover at near-zero thrust (hovering) for hazard detection, and finally descend in a controlled manner. Other applications include orbital rendezvous and docking, precision maneuvers, and trajectory control for missile defense vehicles. A fundamental advantage is that the pintle design maintains high combustion efficiency and complete insensitivity to low-frequency instabilities (known as "chug") along the entire throttling range.

2.5.5 Comparison with the limitations of fixed-area injectors

To fully appreciate the advantage of the pintle, it is useful to compare it with conventional fixed-area injectors, such as impinging jet or coaxial types. These designs have a geometrically fixed injection area, which inextricably links flow rate to pressure drop. Consequently, their throttling range is extremely limited, typically confined to a ratio of 2:1 or, in the best cases, 3:1. If one attempts to reduce thrust beyond this limit in a fixed-area injector, the mass flow rate decreases, and with it, the pressure drop across the orifices collapses. Below a critical threshold of ΔP, the

energy available for atomization becomes insufficient. Droplets become larger, mixing worsens, combustion efficiency drops drastically, and, most dangerously, the engine becomes highly susceptible to combustion instabilities that can lead to catastrophic failure. The pintle-type injector, being variable area, overcomes this fundamental limit. By reducing the injection area while decreasing the flow rate, it is able to decouple the flow rate from the pressure drop, maintaining near-constant and optimal injection conditions over a much wider thrust range. This deep throttling capability is not just an engine performance advantage, but an enabling factor at the mission architecture level. It makes operational profiles possible that would be unfeasible or extremely inefficient with fixed-thrust engines. Consider again the example of a lunar lander: to execute the braking, descent, and hover sequence, a vehicle with fixed-thrust engines would require a complex and heavy system, composed of multiple engines of different thrusts or based on imprecise and stressful "bang-bang" control (short ignitions and shutdowns). The pintle-type injector allows a single engine to execute all these phases continuously, efficiently, and precisely. This advantage extends beyond the engine itself: it simplifies the vehicle's entire propulsion system, reduces the total mass required, and drastically increases mission flexibility and safety. It is a clear example of how a single innovation at the component level can redefine capabilities at the system level.

2.6 Design Simplicity, Reliability, and Reduced Costs

In a field as complex as aerospace engineering, simplicity is often synonymous with reliability and economic convenience. The pintle-type injector embodies this principle, offering an elegant and robust solution that contrasts sharply with the intrinsic complexity of many other injection architectures. This simplicity manifests at the design, production, and optimization levels, translating into tangible advantages in terms of costs, reliability, and development times.

2.6.1 Single-Element vs. Multi-Element Philosophy

The fundamental difference between a pintle-type injector and most other types of injectors lies in its single-element architecture. The entire injection and primary mixing process is handled by a single, large central structure. A complete pintle-type injector can consist of a very limited number of parts, in some cases just five main components, excluding seals and hardware. This design philosophy is in stark contrast to that of multi-element injectors, such as impinging jet or coaxial types. The latter consist of a complex injection plate, on which hundreds, or even thousands, of small orifices or coaxial elements are machined with very high precision. Every single element must be drilled, aligned, and often welded with extremely tight tolerances to ensure uniform flow and correct mixing. The complexity of such a system grows exponentially with the number of elements.

2.6.2 Impact on Production and Development

The drastic reduction in the number of parts and geometric complexity has a deep and positive impact on the entire engine life cycle:

- **Production and Assembly:** the manufacturing of a single element, although requiring precision, is intrinsically simpler and less expensive than the production and inspection of thousands of small holes. The assembly is faster and quality control is more manageable, reducing the probability of manufacturing defects such as clogged or misaligned orifices.
- **Development and Optimization:** the process of optimizing engine performance is remarkably simplified. In a multi-element system, modifying spray or mixing characteristics might require redesigning and manufacturing an entire, very expensive injection plate. With a pintle-type injector, optimization can be achieved by modifying only two relatively simple and low-cost parts: the pintle geometry and that of the annular sleeve. This allows for a more agile and iterative development approach, accelerating timelines and reducing costs.

These factors combine to significantly lower the overall development and qualification costs of an engine. TRW estimates indicated that a rocket engine based on a pintle-type injector could be developed and produced at a cost 50-75% lower than a comparable liquid propellant booster based on more conventional technologies. [14]

2.6.3 Proven In-Flight Reliability

The relationship between simplicity and reliability is a fundamental principle of engineering. A system with fewer components intrinsically has fewer potential points of failure. The pintle-type injector is a shining example of this principle in action. Its mechanical robustness and operational simplicity translate directly into high reliability. The operational history of this technology is exceptional and serves as definitive proof of its reliability. In decades of use, ranging from Apollo missions to modern commercial launchers, hundreds of engines equipped with pintle injectors have been flown without a single in-flight failure attributable to the injector itself ever occurring. The most iconic example remains the performance of the Lunar Module Descent Engine (LMDE) during the dramatic Apollo 13 mission [15]. After the explosion of an oxygen tank in the service module, the crew had to rely on the LMDE engine, not designed for that purpose, to execute the critical burns that would bring them safely back to Earth. The perfect and reliable performance of the engine in that emergency situation consecrated the pintle-type injector as a symbol of engineering robustness.

2.7 Thermal Management: Overheating and Ablation of the Pintle Tip

The main and most critical weakness of the pintle injector is the thermal management of its tip. The same core recirculation zone, which is fundamental for obtaining high combustion efficiency and stability, is also the cause of an extremely concentrated and severe thermal load. The hot combustion gases, at temperatures that can exceed 3000 K, are continuously recirculated and directly impact the pintle tip surface, creating one of the most hostile thermal environments inside the engine. This phenomenon can lead to overheating, melting, and ablation (erosion) of the tip material, compromising the injector geometry and potentially leading to catastrophic failure. The problem is particularly acute in engines utilizing "clean" burning and high-temperature propellants, such as oxygen/methane (LOX/LCH4) or oxygen/hydrogen (LOX/LH2), where the formation of protective soot is minimal or absent. Resolving this challenge requires sophisticated engineering solutions:

- **Advanced Materials:** use of high-temperature resistant superalloys (e.g., niobium or rhenium-based) or advanced ceramic materials for the tip.
- **Active Cooling:** design of complex internal cooling channels within the pintle, through which one of the cryogenic propellants flows to remove heat.
- **Optimized Geometries:** the use of a "deflector" on the tip to shift the spray impingement point and the recirculation zone can increase tip life, but often at the expense of a decrease in combustion efficiency.

2.8 Propellant Selection: Gaseous Methane and Liquid Oxygen

Numerous technical studies have highlighted how the use of methane, or liquefied natural gas (LNG, with methane content up to 98%), as a replacement for kerosene (RP–1), offers a series of significant advantages in rocket propulsion systems. From the perspective of energy performance, the use of methane allows for a sensible increase in the global efficiency of the launcher, with payload mass increases that can exceed 20–30% for the same initial vehicle mass. This benefit is linked primarily to the lower average molecular weight of the combustion products and the higher hydrogen content compared to kerosene. Compared to liquid hydrogen (LH_2), methane presents a lower specific impulse, but offers significantly higher density, which translates into smaller volume tanks, lower structural penalties, and overall simpler cryogenic management. This compromise between performance and density makes methane particularly attractive for applications in which volumetric efficiency and system complexity reduction play a central role. A further relevant advantage is represented by the thermal behavior of methane in regenerative cooling systems. For the same heat flux removed from the combustion chamber, it is possible to obtain the same cooling effect

with a methane flow rate approximately halved compared to kerosene, thanks to its thermophysical properties. This entails an indirect increase in specific impulse and greater flexibility in the design of the cooling circuit. From a chemical standpoint, it has been experimentally observed that methane does not lead to the formation of carbonaceous residues or soot (carbon black) in fuel-rich gas generators, unlike what happens with kerosene. The absence of coking phenomena eliminates one of the main limitations to the reliability and reusability of rocket engines, opening the possibility of employing indifferently different engine cycles, including oxidizing or fuel-rich gas generator cycles, dual gas generator configurations, and more complex schemes. This aspect results particularly critical for reusable applications, as it drastically reduces inspection, maintenance, and refurbishment operations between one flight and the next. From an environmental profile, methane presents greater cleanliness of combustion products compared to kerosene, as well as lower toxicity of propellant components in case of accidental leaks or draining operations. These characteristics contribute to reducing the environmental impact of launch operations and simplify ground management of the propulsion system [16].

2.9 Geometric Characterization

The geometry of a pintle injector determines the spatial distribution of the propellants. Sizing revolves around specific diameters that serve as reference lengths for dimensionless correlations.

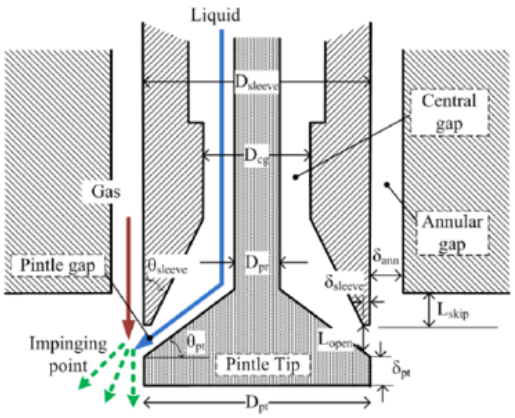

Figure 2.7: pintle geometric section [17]

2.9.1 Pintle Diameter (D_p)

The diameter of the central post (D_p) is the primary dimension that defines the scale of the injector and acts as a central body.

2.9.1.1 Influence on Stability

The pintle diameter is fundamental for the creation of the Central Recirculation Zone (CRZ). A larger diameter favors a wider CRZ, improving flame anchoring and

stability at low flow regimes [18] [19].

2.9.1.2 Design Correlations

In equations for calculating the *Blockage Factor* (BF) and dimensionless *Skip Distance*, D_p appears in the denominator as a normalization factor.

2.9.2 Tip Diameter (D_{pt}) and Profile

Although often coinciding with D_p, the tip diameter can vary in advanced designs [17].

2.9.2.1 Tip Geometry

The tip can be flat, conical, or contoured. A flat tip generates an intense recirculation zone but is thermally burdensome. An aerodynamic tip reduces drag but can weaken flame stabilization [20].

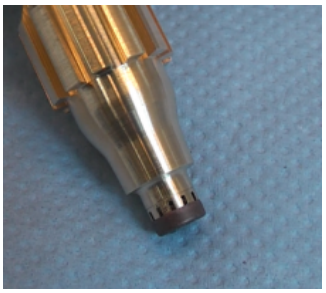

Figure 2.8: Shortened LOX passage and reduced skip ratio [20]

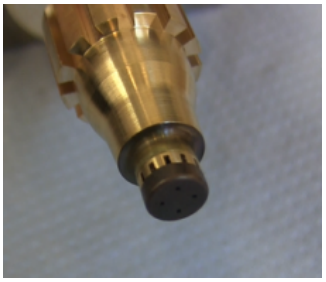

Figure 2.9: Active cooling system incorporated for pintle tip[20]

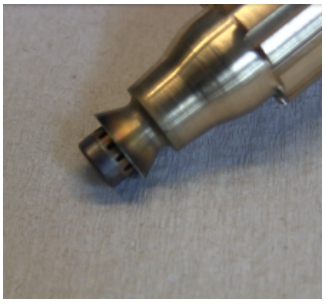

Figure 2.10: Deflector for displacement of the impingement point[20]

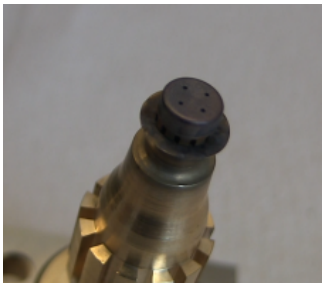

Figure 2.11: Deflector and a cooled pintle tip [20]

2.9.2.2 Thermal Integrity

In high-performance engines, the tip is made of high-conductivity materials (Copper, Cu-Cr alloys) or protected by ablative coatings to withstand the backflow heat flux [18].

2.9.3 Annular Gap (δ_{ann})

The thickness of the annular passage (δ_{ann}) is critical for flow symmetry. It influences the axial velocity of the film (V_a) and its uniformity around the pintle.

2.9.4 Radial Inlet Configuration

The radial propellant inlet can be realized via rectangular holes or slots or via a continuous slit. The choice affects jet distribution and atomization characteristics [21] [18].

Figure 2.12: Canted slot configuration[18]

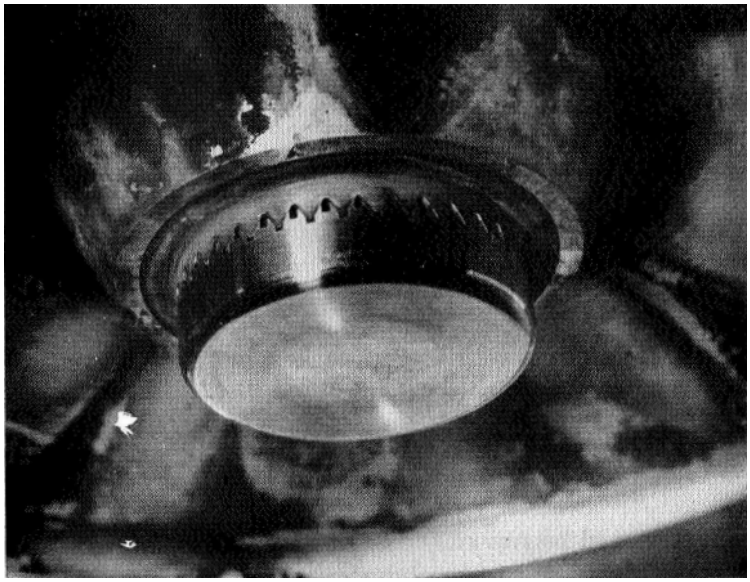

Figure 2.13: Sawtooth configuration[18]

2.9.4.1 Parameters and Aspect Ratio

A high Aspect Ratio ($AR = h/w$, with h and w being dimensions of the rectangular slots) favors jet stability. However, slots that are too narrow increase viscous pressure losses and the risk of clogging [21].

2.9.4.2 Multiple Row Arrangement

In LOx/GCH_4 engines, double-row configurations are used: the primary penetrates the annular film for combustion, the secondary provides film cooling to the tip [21].

2.9.4.3 Circular Holes and Penetration

Circular holes offer superior C_d and greater penetration. However, they leave larger gaps between jets, reducing mixture uniformity immediately downstream.

2.9.5 Skip Distance (L_s)

The distance between the annular exit and the radial orifices (L_s) is a crucial parameter for film formation and jet stability [22].

- Excessive L_s: if the distance is too long, wall friction significantly slows down the film. The axial velocity (V_a) at the impact point decreases, reducing the available axial momentum. This leads, by conservation of momentum, to an increase in the resulting spray angle and less efficient atomization.
- Design Criterion: the consolidated rule of thumb suggests that the dimensionless ratio L_s/D_p should be kept around 1 or lower ($L_s/D_p \leq 1$) [22].

2.10 Analysis of Dimensionless Parameters

Along with geometric parameters, there are key dimensionless parameters that govern pintle injector performance. These are TMR (Total Momentum Ratio), LMR (Local Momentum Ratio), Discharge Coefficient (C_d) and BF (Blockage Factor).

2.10.1 Blockage Factor (BF)

The BF is the fraction of the pintle perimeter occupied by the orifices:

$$BF = \frac{N \cdot w_{slot}}{\pi D_p} \tag{2.3}$$

2.10.1.1 Atomization Regimes

- **BF $<$ 0.3 (Blow-through):** poor mixing, the annular flow passes between the jets.
- **BF 0.3 - 0.6:** optimal regime. The radial jets form an almost continuous barrier. The annular flow is forced to impact the radial jets, maximizing momentum transfer and droplet breakup energy. However, the value should not be too high in order to protect the pintle tip [23].

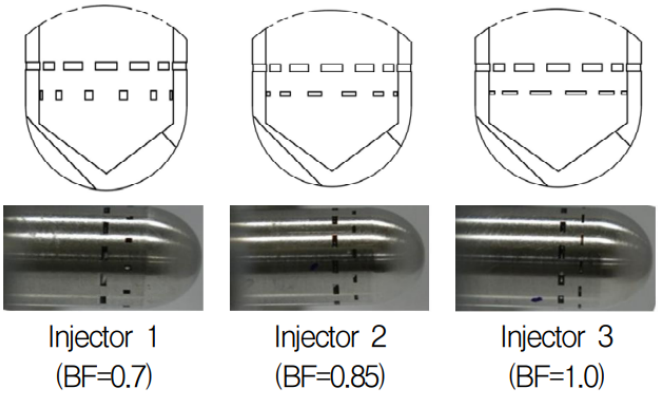

Figure 2.14: three different blockage factor[23]

2.10.2 Total Momentum Ratio (TMR)

This is the ratio between the momenta of the radial and axial flow:

$$TMR = \frac{q_r}{q_a} = \frac{\dot{m}_r \cdot V_r}{\dot{m}_a \cdot V_a} \tag{2.4}$$

In configurations where radial jets are not perfectly perpendicular but inclined by an angle α with respect to the normal, the formula includes a trigonometric correction term [17]:

$$TMR = \frac{\dot{m}_r \cdot V_r \cdot \cos(\alpha)}{\dot{m}_a \cdot V_a + \dot{m}_r \cdot V_r \cdot \sin(\alpha)} \tag{2.5}$$

It is a crucial parameter influencing spray angle and mixing.

2.10.2.1 Definition and Spray Angle

The TMR is the ratio between the momentum of the radial and axial flow. The theoretical correlation for the angle θ is:

$$\theta = \arccos\left(\frac{1}{1+TMR}\right) \tag{2.6}$$

A high TMR opens the spray, a low TMR closes it.

2.10.2.2 Optimal TMR: Gas-Liquid vs Liquid-Liquid

While for liquid-liquid propellants $TMR \approx 1$ was sought, for Gas-Liquid pairs (e.g., Gaseous Methane) the efficiency peak is often found between $0.3 < TMR < 0.7$, thanks to the aerodynamic breakup induced by the high gas velocity [17].

2.10.3 Local Momentum Ratio (LMR): Definition and Importance

While TMR represents a global balance of inertial forces, it fails to capture the complexities of local interaction in discrete orifice configurations (slots or holes). To accurately describe the physics of atomization point by point, the *Local Momentum Ratio* (LMR) is introduced, defined as the ratio between momentum fluxes (or dynamic pressures, q) calculated on the areas of effective interaction:

$$LMR = \frac{q_{r,loc}}{q_a} = \frac{\dot{m}_{r,loc} \cdot V_{r,loc}}{\dot{m}_a \cdot V_a} \tag{2.7}$$

This parameter is the true driver of spray morphology, governing the penetration of the radial jet into the annular film.

2.10.4 Experimental Analysis: Study by Jin et al. (2022)

A recent experimental study conducted by Jin et al. [24] on a gas-liquid pintle injector element (air-water) provided crucial quantitative evidence regarding the hydraulic independence of channels and the optimization of injection parameters.

2.10.4.1 Decoupling of the Discharge Coefficient (C_d)

A fundamental result emerging from the study concerns the hydraulic stability of the injector. The experimental tests demonstrated that the external motion field (annular gas flow) does not significantly influence the hydraulics of the radial orifices. In particular:

- The C_d of the liquid line was found to be independent of the LMR value and the gas impact pressure.
- The value of C_d primarily depends on the geometry and diameter of the orifice itself (d_o).

This evidence of hydraulic decoupling significantly simplifies the mathematical modeling of the injector, allowing the two feed lines to be treated as separate systems even in the presence of strong aerodynamic interaction downstream.

2.10.4.2 Mixing Optimization and Spray Angle

The analysis of the spatial distribution of the spray allowed for identifying optimal operating conditions:

- **Optimal Point ($LMR \approx 1$):** in this condition, the radial penetration of the liquid coincides almost perfectly with the extension of the annular gas film. This maximizes mixing efficiency, avoiding both *blow-through* (LMR too low) and excessive impact on the wall (LMR too high).
- **Correlation for Spray Angle (θ):** the authors proposed a correction to classical predictive models, highlighting that at low LMRs, the lateral expansion of the jet introduces deviations with respect to one-dimensional theory. The derived empirical relationship is:

$$\tan(\theta) \propto LMR^{0.5819} \tag{2.8}$$

The exponent 0.5819 indicates that the sensitivity of the spray angle to flow rate variations is less than linear. This "damped" behavior is a positive factor for combustion stability, especially during *deep throttling* phases where injection conditions vary drastically.

2.11 Summary of Key Parameters

The main functional parameters of the pintle injector are reported below in Table 2.1, with their definitions, effects on performance, and optimal operating ranges.

Table 2.1: Summary of Key Parameters

Parameter	Symbol	Effect and Optimal Range
Total Momentum Ratio	TMR	Determines angle α. Range optimal $0.3 - 0.7$ (Gas-Liq).
Blockage Factor	BF	Mixing efficiency. Range optimal $0.35 - 0.60$.
Skip Distance Ratio	L_s/D_p	Film/thermal stability. Keep ≤ 1.0.
Local Momentum Ratio	LMR	Local spray angle predictor. Range optimal $LMR \approx 1$.

Chapter 3

Theoretical Background

In this chapter, the fundamental theoretical concepts related to liquid propellant rocket engines are presented. The expressions related to ideal rockets will be discussed. All of this serves to arrive at a 0D model, the results of which will be discussed in subsequent chapters.

3.1 Fundamentals of Gasdynamics and Rocket Propulsion Physics

The design of an injection system for a liquid rocket engine (LRE) requires a rigorous understanding of the thermodynamic and gasdynamic principles governing the conversion of chemical energy into propulsive thrust. In this context, the injector is not an isolated component, but the critical interface element that determines the efficiency of the combustion reaction. This section explores the equations governing rocket physics, focusing on the relationships necessary to derive mass flow rates from thrust requirements and to analyze engine behavior under deep throttling conditions.

3.1.1 Thermodynamics of the Ideal Rocket Engine

To establish a tractable mathematical model during the preliminary design phase, the "ideal rocket" hypothesis is adopted. This theoretical construct, extensively detailed in classical literature such as Sutton [25] and in university lecture notes [26], is founded on a series of simplifying assumptions that allow thermodynamic principles to be expressed through closed-form algebraic relationships. The pivotal assumptions for the ideal rocket model include:

- **Fluid Homogeneity:** the combustion products are considered a homogeneous and gaseous mixture.
- **Ideal Gas:** the fluid mixture follows the ideal gas laws.
- **Adiabaticity:** the expansion process in the nozzle is adiabatic, meaning it occurs in the absence of heat exchange with the walls.

- **Isentropic Flow:** the absence of friction and dissipative phenomena within the flow is assumed.
- **Chemical Equilibrium:** the chemical composition is assumed to be in equilibrium or frozen during expansion.
- **One-dimensionality:** the gaseous flow possesses exclusively an axial velocity component.
- **Uniformity:** gas velocity, temperature, pressure, and density present a uniform profile across every cross-section of the nozzle.
- **Steadiness:** transient effects are negligible; the propellant mass flow rate is constant and steady over time.
- **Continuity:** no shock waves or other fluid dynamic discontinuities are present in the flow.

Although practical experience demonstrates that real performance deviates from ideal values (typically with a deficit between 6% and 10% due to divergence, boundary layer, and finite chemical kinetics losses), the ideal model provides the indispensable basis for calculating the macroscopic parameters of the engine.

3.1.1.1 Thrust Generation and Specific Impulse

Thrust F, defined as the resultant force acting on the vehicle due to the expulsion of propulsive gases, is described by the fundamental equation of rocket propulsion. This equation combines the contribution of the change in fluid momentum with the contribution of static pressure forces acting on the nozzle exit surface:

$$F = \dot{m}u_e + (p_e - p_a)A_e \tag{3.1}$$

Where:

- $\dot{m}$ represents the total mass flow rate of the expelled propellants [kg/s].
- u_e is the average gas velocity at the nozzle exit plane, assumed axial and uniform [m/s].
- p_e is the static pressure of the fluid at the exit plane [Pa].
- p_a is the external ambient pressure [Pa].
- A_e is the area of the nozzle exit section [m^2].

This expression highlights two distinct operating regimes. The first term, $\dot{m}u_e$, is the momentum contribution, which dominates thrust generation in engines with high efflux velocity. The second term, $(p_e - p_a)A_e$, is the pressure contribution. When the exit pressure exactly equals the ambient pressure ($p_e = p_a$), the nozzle is

said to be adapted, and thrust is maximized for a given expansion ratio. However, in an engine intended for *throttling*, where the chamber pressure p_c varies widely, maintaining perfect adaptation is impossible without a variable geometry nozzle. Consequently, theoretical analysis must consider performance penalties deriving from under-expansion ($p_e > p_a$) or over-expansion ($p_e < p_a$) of the gas during thrust modulation. The overall efficiency of the propulsion system is condensed into the Specific Impulse parameter (I_{sp}), which represents the thrust generated per unit weight of propellant consumed per second. Analytically:

$$I_{sp} = \frac{F}{\dot{m} g_0} \tag{3.2}$$

Where g_0 is the standard gravitational acceleration ($9.81\,\mathrm{m/s^2}$). This parameter is the primary figure of merit for comparing different propellant combinations and engine cycles, as it directly reflects the thermochemical and gasdynamic efficiency of the system.

3.1.2 Dimensionless Performance Parameters: c^* and C_F

To decouple the analysis of combustion chamber efficiency from that of the nozzle, rocket theory introduces two fundamental parameters: the characteristic velocity (c^*) and the thrust coefficient (C_F).

3.1.2.1 The Characteristic Velocity (c^*)

The characteristic velocity c^* is a parameter that depends exclusively on the thermodynamic properties of the propellants and combustion efficiency, being independent of the nozzle geometry downstream of the throat. It is defined operationally as:

$$c^* = \frac{p_c A_t}{\dot{m}} \tag{3.3}$$

Where p_c is the stagnation pressure in the combustion chamber and A_t is the area of the nozzle throat section. This relationship is of crucial importance in the design flow, as it allows for directly linking the target chamber pressure and throat geometry to the required mass flow rate. From a theoretical standpoint, assuming an isentropic ideal gas, c^* can be expressed as a function of gas properties:

$$c^* = \frac{\sqrt{\gamma R T_c}}{\gamma \sqrt{\left(\frac{2}{\gamma+1}\right)^{\frac{\gamma+1}{\gamma-1}}}} \tag{3.4}$$

In this equation:

- γ is the specific heat ratio (c_p/c_v) of the combustion gases.
- R is the specific gas constant (R_{univ}/MW_{gas}).
- T_c is the adiabatic flame temperature in the combustion chamber.

Analysis of this equation reveals that to maximize c^*, and thus minimize the propellant mass necessary for a given maneuver, it is necessary to maximize the combustion temperature T_c and minimize the average molecular weight of the products MW_{gas}. This principle guides the selection of the mixture ratio (O/F), since variations in the oxidizer/fuel ratio alter both T_c and the chemical composition of the gases.

3.1.2.2 The Thrust Coefficient (C_F)

While c^* measures chamber combustion efficiency, the thrust coefficient C_F measures the nozzle's aerodynamic efficiency in converting the stagnation enthalpy of combustion gases into axial kinetic energy, thus maximizing the generated thrust. Thrust can be rewritten as:

$$F = C_F A_t p_c \tag{3.5}$$

The analytical expression for C_F in a one-dimensional isentropic flow is:

$$C_F = \sqrt{\frac{2\gamma^2}{\gamma-1}\left(\frac{2}{\gamma+1}\right)^{\frac{\gamma+1}{\gamma-1}}\left[1-\left(\frac{p_e}{p_c}\right)^{\frac{\gamma-1}{\gamma}}\right]} + \frac{(p_e - p_a)}{p_c}\frac{A_e}{A_t} \tag{3.6}$$

This complex equation demonstrates that C_F is a function of the nozzle expansion ratio ($\epsilon = A_e/A_t$), the pressure ratio (p_e/p_c), and the specific heat ratio γ. Optimization of C_F requires a balance between nozzle geometry and operating conditions, especially in a variable thrust engine where p_c and therefore p_e vary significantly.

3.1.3 Mass Flow Derivation via Mixture Ratio (O/F)

The sizing of the pintle injector begins with the determination of the oxidizer and fuel mass flow rates necessary to cover the entire flight envelope, from the minimum thrust level (*deep throttling*) to the nominal maximum thrust. The logical process, supported by the use of chemical equilibrium codes such as NASA CEA (*Chemical Equilibrium with Applications*), follows these analytical steps:

3.1.3.1 Thermochemical Analysis

The CEA software is used to analyze the combustion reaction between the chosen propellants (e.g., Liquid Oxygen and Gaseous Methane). Once the chamber pressure p_c is fixed, the trend of the theoretical characteristic velocity c^* is calculated as the mixture ratio O/F varies.

$$CH_4 + 2O_2 \rightarrow CO_2 + 2H_2O \tag{3.7}$$

$$\frac{O}{F} = \frac{2 \cdot 2 \cdot 16}{12 + 4 \cdot 1} = 4 \tag{3.8}$$

Although the stoichiometric ratio for this reaction is 4, the maximum I_{sp} is typically obtained with slightly fuel-rich mixtures ($O/F < 4$), where the lower molecular

weight of the products compensates for the slightly lower flame temperature.

3.1.3.2 Selection of Optimal O/F and Mass Flow Calculation

The determination of propellant mass flow rate is the first step for hardware sizing. The iterative process adopted in this work sets the design point at the nominal maximum thrust condition (F_{max}), from which the fixed geometric characteristics of the engine are derived.

1. **Thermochemical Simulation (CEA):** having fixed the maximum design chamber pressure $p_{c,max}$ and assumed optimal expansion ($p_e = p_a$), a range of mixture ratios is analyzed. The O/F that maximizes the characteristic velocity c^* is identified.

2. **Extraction of Ideal Parameters:** corresponding to the optimal O/F, the value of the theoretical Specific Impulse (I_{sp}) and characteristic velocity (c^*) are extracted from the thermochemical code.

3. **Calculation of Maximum Flow Rate:** given the maximum required thrust (F_{max}), the total design mass flow rate is derived from the definition of Specific Impulse:
$$\dot{m}_{tot,max} = \frac{F_{max}}{I_{sp} \cdot g_0} \tag{3.9}$$
Where g_0 is the standard acceleration of gravity ($9.81\,\mathrm{m/s^2}$).

4. **Throat Sizing (A_t):** using the maximum flow rate just calculated, the critical nozzle area (throat) necessary to maintain the desired pressure $p_{c,max}$ is sized:
$$A_t = \frac{\dot{m}_{tot,max} \cdot c^*}{p_{c,max}} \tag{3.10}$$
Fundamental Note: since the engine is designed with a fixed geometry, the value of A_t calculated in this phase is considered constant and invariable for all subsequent throttling analyses at reduced thrust regimes.

In this phase, the thrust coefficient C_F is calculated a posteriori as a verification parameter of nozzle efficiency ($C_F = F/(p_c A_t)$), and not as a design input.

3.1.3.3 Design Flow Splitting

The individual flow rates of oxidizer ($\dot{m}_{ox}$) and fuel ($\dot{m}_f$), necessary for sizing the pintle injection areas at maximum power, are derived algebraically from the chosen optimal mixture ratio:

$$\dot{m}_{tot,max} = \dot{m}_{ox} + \dot{m}_f \tag{3.11}$$
$$O/F = \frac{\dot{m}_{ox}}{\dot{m}_f} \tag{3.12}$$

Solving the system, the final expressions used in the calculation model are obtained:

$$\dot{m}_f = \frac{\dot{m}_{tot,max}}{1 + O/F}, \quad \dot{m}_{ox} = \dot{m}_{tot,max} - \dot{m}_f \tag{3.13}$$

3.2 Atomization Physics and Sauter Mean Diameter (SMD)

The injector performs the thermodynamic function of preparing reactants for combustion through the atomization process. The transformation of continuous liquid jets or films into a population of discrete droplets exponentially increases the specific surface area of the propellant, accelerating evaporation and reaction rates. In a pintle injector, this process is governed by the interaction between a radial film (or radial jets) and an axial film, resulting in a complex hollow cone spray morphology.

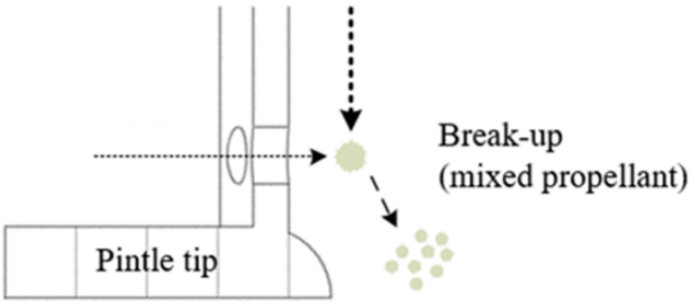

Figure 3.1: break-up scheme[27]

3.2.1 The Concept of Sauter Mean Diameter (D_{32})

Sprays produced by injectors are not monodisperse; they contain droplets of varying sizes distributed statistically. To characterize the efficiency of such a spray for combustion purposes, it is not sufficient to use an arithmetic mean diameter (D_{10}), since vaporization and combustion physics are dominated by surface-to-volume ratios. The reference parameter is the Sauter Mean Diameter (SMD or D_{32}). It is defined as the diameter of a hypothetical spherical droplet that possesses the same volume/surface ratio as the entire polydisperse spray:

$$D_{32} = \frac{\sum N_i d_i^3}{\sum N_i d_i^2} \tag{3.14}$$

Where N_i is the number of droplets with diameter d_i. The physical relevance of D_{32} derives directly from its connection to mass transfer. Since the vaporization rate of a droplet is proportional to its surface area ($\propto d^2$), while the mass to be vaporized is proportional to volume ($\propto d^3$), the volume/surface ratio determines the average "lifetime" of the liquid phase in the chamber. A low SMD value implies a fine spray with a large surface area available for heat exchange, favoring rapid and efficient

combustion.

3.2.2 Breakup Mechanisms and Weber Number

The disintegration of the liquid film in a pintle injector occurs through a staged process: Primary Instability (Kelvin-Helmholtz waves), Primary Breakup (ligament formation), and Secondary Breakup (shattering into fine droplets). The dimensionless parameter governing this balance of forces is the Weber Number (We):

$$We = \frac{\rho_{gas} L_{caratt} (U_{gas} - U_{liq})^2}{\sigma_{liq}} \tag{3.15}$$

Where:

- ρ_{gas} is the density of the gaseous medium.
- $U_{gas} - U_{liq}$ is the relative velocity between phases, the primary driver of *shear*.
- σ_{liq} is the surface tension of the liquid.
- L_{caratt} is the characteristic length, often identified with the pintle opening distance (L_{open}).

A high Weber number ($We \gg 1$) indicates that inertial forces prevail, leading to rapid and effective atomization.

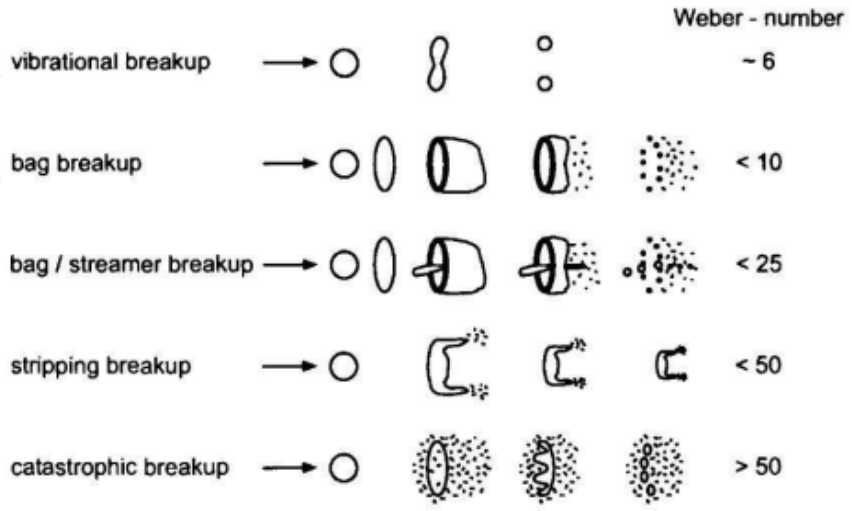

Figure 3.2: break up models examples[28]

3.2.3 Empirical Correlations for Pintle Injectors: The Min Son Model

Given the complexity of two-phase fluid dynamics, SMD prediction often relies on semi-empirical correlations. In the specific context of variable geometry pintle injectors, the work of Min Son et al. [29] provides a robust mathematical model. The correlation for calculating D_{32} is expressed as:

$$D_{32} = L_{open} \cdot \xi^{-1} \cdot \exp\left(-q \cdot We^{0.1}\right) \tag{3.16}$$

Physical analysis of the terms:

- **Linear Dependence on L_{open}:** SMD scales linearly with pintle opening. Increasing L_{open} to increase flow rate increases liquid film thickness, producing larger droplets.
- **Geometric Factor ξ:** defined as $\xi = \frac{90}{90-\theta_{pt}}$, where θ_{pt} is the pintle tip angle. This term models the influence of impact geometry.
- **Exponential Dependence on Weber:** the exponential term indicates that SMD decreases rapidly at low We values but reaches an asymptote at high values.
- **Parameter q:** empirical coefficient calculated as $q = 3.455 - 0.225\xi$.

3.2.4 Vaporization Physics: The Classical D^2 Law

Once atomized, propellant droplets must vaporize completely to participate in the gas-phase combustion reaction. The theoretical starting point is the quasi-steady model of the "D^2 Law" (Godsave-Spalding), according to which the square of the droplet diameter decreases linearly over time:

$$\frac{d(D^2)}{dt} = -K_{vap} \tag{3.17}$$

Where K_{vap} is the vaporization constant (typically expressed in mm^2/s). Integrating the equation between the initial diameter D_0 and complete evaporation ($D = 0$), the characteristic droplet lifetime t_{life} is obtained:

$$t_{life} = \frac{D_0^2}{K_{vap}} \tag{3.18}$$

In the context of rocket propulsion, K_{vap} is a function of the Spalding Transfer Number (B) [30], which quantifies the thermodynamic driving force of the mass transfer process:

$$K_{vap} = \frac{8k_g}{\rho_l c_{p,g}} \ln(1+B) \quad \text{with} \quad B = \frac{c_{p,g}(T_c - T_{sat})}{h_{fg}} \tag{3.19}$$

Where T_c is the combustion gas temperature, T_{sat} is the droplet saturation temperature, and h_{fg} is the latent heat of vaporization.

3.2.4.1 Physical Interpretation of the Spalding Number

From a thermodynamic perspective, the transfer number B represents the fundamental ratio between the energies involved in the phase change. It can be interpreted as

a dimensionless energy balance between the external driving force and the droplet's internal thermal inertia:

$$B = \frac{\Delta h_{sensible}}{\Delta h_{latent}} = \frac{\text{Available Enthalpic Potential}}{\text{Energy Required for Phase Change}} \tag{3.20}$$

Analyzing the fraction terms:

- the numerator $[c_{p,g}(T_c - T_{sat})]$ quantifies the sensible thermal energy available in the high-temperature gaseous environment, ready to flow towards the liquid-vapor interface.
- the denominator (h_{fg}) represents the specific energy "cost" necessary to overcome the liquid's intermolecular forces and transform a unit of mass into vapor.

The magnitude of B thus defines the evaporation regime:

- for high values ($B > 5$–10), typical of combustion in rocket engines, the environmental thermal potential vastly exceeds the required latent heat. In this regime, vaporization is vigorous and limited primarily by mass transport phenomena (diffusion and convection).
- for low values ($B < 1$), the process is energetically costly compared to available heat, resulting in slow evaporation kinetics controlled by heat transfer.

3.2.5 Vaporization Distance Model (Modified D^2 Law)

The classical model provides a temporal magnitude (t_{life}), which is insufficient for geometric chamber sizing. To obtain an explicit spatial coordinate (X_{vap}), it is necessary to integrate droplet velocity in the accelerating flow. In this work, the methodology of Min Son et al. [29] is adopted, which proposes a modified version of the D^2 law. This analytical formulation correlates the vaporization distance to thermofluid dynamic properties and the initial droplet radius:

$$X_{vap} \approx r_{d0}^2 \left[\frac{c_{p,c}\rho_l}{k_c} \frac{\sqrt{\gamma R_c T_c}}{\ln(1+B)} \right] \frac{1}{(2+\varphi)} \tag{3.21}$$

Where:

- $r_{d0} = \text{SMD}/2$ is the initial radius of the representative droplet (based on the Sauter Mean Diameter).
- φ is the interaction parameter, which accounts for forced convection and aerodynamic drag effects on the droplet.
- The term in square brackets represents the thermal characteristic time scaled by the local speed of sound.

Eq. 3.21 highlights a quadratic dependence on radius ($X_{vap} \propto r_{d0}^2$): this confirms that atomization quality (low SMD) is the dominant factor for reducing the required characteristic length L^* maximizing efficiency c^* and preventing combustion instabilities.

3.3 Optimization Theory: Convex Quadratic Programming (CQP)

The design of a pintle injector involves resolving intrinsic conflicts between performance parameters and geometric constraints (e.g., minimum SMD vs maximum allowable ΔP). In this work, the *Convex Quadratic Programming* (CQP) methodology is adopted, following the approach of Cha, Andersson, and Bohlin [17].

3.3.1 The Role of Scatter Analysis

Before formal optimization, a scatter analysis is performed. This stochastic method consists of generating a vast number of geometric configurations (varying L_{open}, θ_{pt}, etc.) and calculating their performance. It serves to map the design space and identify a robust starting point (guess) for the optimization algorithm, avoiding local minima. The results and algorithms used are discussed in chapter 4.

3.3.2 Mathematical Foundations of CQP

Quadratic Programming (QP) deals with problems involving a quadratic objective function and linear constraints. The canonical formulation is:

$$\text{Minimize: } J(\mathbf{x}) = \frac{1}{2}\mathbf{x}^T\mathbf{Q}\mathbf{x} \tag{3.22}$$

$$J = \mathbf{x}^T\mathbf{Q}\mathbf{x} = \begin{bmatrix} x_1 \\ x_2 \\ \vdots \\ x_n \end{bmatrix}^T \begin{bmatrix} Q_1 & 0 & \cdots & 0 \\ 0 & Q_2 & \cdots & 0 \\ \vdots & \vdots & \ddots & \vdots \\ 0 & 0 & \cdots & Q_n \end{bmatrix} \begin{bmatrix} x_1 \\ x_2 \\ \vdots \\ x_n \end{bmatrix} \tag{3.23}$$

Where $\mathbf{x}$ is the vector of design variables (geometric and operational) and $\mathbf{Q}$ is the weight matrix. The objective is to minimize J, which represents a general measure of performance.

$$\min_{\mathbf{x}}(J) \Rightarrow \frac{\partial J}{\partial \mathbf{x}} = 0 \tag{3.24}$$

Chapter 4

Design Methodology and Numerical Analysis

4.1 Research Objectives and Code Architecture

The primary objective of this chapter is the development of an integrated numerical methodology for the sizing, optimization, and preliminary thermal verification of a pintle-type injector. Reference was made to the work conducted by Andersson, Cha, and Bohlin in their study on bi-propellant injector design [17], extending the original approach with the prediction of convective thermal loads (h_c). The developed methodology is articulated in the sequential implementation of four distinct computational scripts, which reflect the logical design flow:

1. **Sizing Script (0D Model):** defines the geometric and thermodynamic envelope of the engine based on ideal chemical equilibria and interfacing with NASA CEA libraries (*Chemical Equilibrium with Applications*).

2. **Performance Scatter Analysis:** explores the design space by mapping the non-linear relationships between geometric variables and performance metrics (SMD, Vaporization Distance, Spray Angle).

3. **Thermal Model Integration (h_c):** a module dedicated to the calculation of the convective heat transfer coefficient on the pintle tip, employing advanced semi-empirical correlations (Katti-Prabhu).

4. **Optimizer with 3D Visualization:** implementation of a convex quadratic programming (CQP) algorithm to minimize a weighted cost function. This module is enriched by a three-dimensional visualization system to analyze the robustness of the solution as optimization weights vary.

This modular structure allows for separating hydraulic optimization from thermal verification, ensuring that the final configuration meets combustion efficiency requirements while respecting material limits imposed by local heat fluxes.

4.2 Preliminary Design and 0D Model

4.2.1 Thermodynamic Fundamentals and Basic Assumptions

The first script constitutes the preliminary sizing engine. It implements a zero-dimensional (0D) model assuming adiabatic combustion in chemical equilibrium. The design operating conditions are set for a demonstrator engine with a thrust $F = 1000N$ and a throttling capability of 5:1, fueled by Liquid Oxygen (LOX) and Gaseous Methane (GCH_4) [17].

4.2.2 Iterative Thermochemical Sizing Procedure (CEA)

To determine the theoretical performance and mass flow rates required at various throttling levels, an iterative calculation procedure interfaced with the NASA CEA code (*Chemical Equilibrium with Applications*) was implemented. The analysis is divided into two logical phases: the definition of the nominal design point and the off-design analysis for partial thrust levels.

4.2.2.1 Phase 1: Nominal Point and Nozzle Geometry

At the maximum thrust level ($F_{max} = 1000\,\text{N}$), the ideal adaptation condition ($P_e = P_a$) is assumed.

1. **O/F Optimization:** via CEA, the characteristic velocity (c^*) is calculated as the mixture ratio varies. The O/F that maximizes c^* (equal to 2.7 in the case under examination) is selected.

2. **Geometry Freezing:** having fixed the maximum chamber pressure ($P_{c,max}$) and the optimal O/F, the geometric dimensions of the nozzle are calculated, which will remain constant for all operating regimes:

   - Throat area (A_t), sized to guarantee the necessary flow rate at $P_{c,max}$.
   - Nozzle expansion ratio ($\epsilon = A_e/A_t$), calculated to ensure adaptation to ambient pressure only at maximum thrust.

4.2.2.2 Phase 2: Iterative Loop for Off-Design Analysis

For reduced thrust levels (throttling down to 200 N), the geometry (A_t and ϵ) is fixed; therefore, the expansion will no longer be optimal ($P_e \neq P_a$). Since the relationship between thrust and pressure is not perfectly linear due to the variation in nozzle efficiency (C_F), an iterative algorithm is required to determine the exact required P_c:

1. **Initial Guess:** a pressure value is initially assumed within a possible range for that specific thrust and geometry.

2. **Thermochemical Calculation:** with the geometry fixed (ϵ) and the new estimated P_c, CEA is executed to recalculate the thermodynamic parameters

(γ, T_c, c^*) and find the new local optimal O/F, which varies slightly with pressure.

3. **Thrust Verification:** the actual thrust generated with the estimated pressure is calculated:

$$F_{calc} = C_F P_c A_t \tag{4.1}$$

Where C_F is recalculated considering the over-expansion or under-expansion of the flow.

4. **Pressure Tuning (Iteration):** the calculated thrust (F_{calc}) is compared with the target thrust (F_{target}).

- If $F_{calc} < F_{target}$, P_c is incremented.
- If $F_{calc} > F_{target}$, P_c is decremented.

The cycle repeats until the percentage error between desired and calculated thrust falls below a tolerance threshold.

4.2.2.3 Final Results and Flow Rate Calculation

Upon reaching convergence, the correct values of P_c and c^* are obtained for each throttling level (Reference Table). Finally, the oxidizer and fuel mass flow rates are derived by solving the system:

$$\dot{m}_{tot} = \frac{P_c A_t}{c^*}, \quad \begin{cases} \dot{m}_{ox} + \dot{m}_f = \dot{m}_{tot} \\ \dot{m}_{ox}/\dot{m}_f = (O/F)_{opt} \end{cases} \tag{4.2}$$

This approach ensures that the mass requirements provided to the subsequent injector design steps are consistent with the real thermofluid dynamics of the engine in off-design conditions.

Table 4.1: Results of thermochemical sizing at various throttling levels (including C^*).

Target [N]	P_c [bar]	**Calc. Thrust** [N]	C_F [-]	$\dot{m}_{ox}$ [kg/s]	$\dot{m}_f$ [kg/s]	C^* [m/s]
1000	20.00	1000.0	1.415	0.2794	0.1022	1852.2
800	16.46	800.0	1.375	0.2303	0.0842	1849.6
600	12.93	600.0	1.313	0.1812	0.0663	1846.2
400	9.40	400.0	1.205	0.1320	0.0483	1841.5
200	5.87	200.0	0.965	0.0828	0.0303	1834.2

4.2.3 Injection Velocity Calculation and Initial Geometry

The injector architecture envisages LOX flow through the central orifice and gaseous methane through the external ring (annulus), a standard configuration to favor

stability [17]. The calculation of injection velocities requires differentiated treatment for the two phases. For the liquid phase (LOX), assumed incompressible, the velocity derives from Bernoulli's equation, imposing a target ΔP to decouple the supply from chamber instabilities:

$$U_{liq} = C_d \sqrt{\frac{2\Delta P_{inj}}{\rho_{liq}}} \tag{4.3}$$

For the gas phase (GCH_4), treated as isentropic compressible flow, it is necessary to verify that the velocity does not exceed the local speed of sound (choking condition) in the annulus:

$$U_{gas} = \sqrt{2\frac{\gamma}{\gamma-1} R T_{gas} \left[1 - \left(\frac{P_c}{P_{inj}}\right)^{\frac{\gamma-1}{\gamma}}\right]} \tag{4.4}$$

Based on these velocities, the passage areas (A_{ox}, A_{ann}) and fundamental geometric parameters (D_{pt}, δ_{ann}, L_{open}) are sized, imposing manufacturability constraints such as $L_{open} \geq 0.1\,\text{mm}$ [17].

4.3 Performance Analysis via Scatter Analysis

4.3.1 Design Space Exploration

Given the non-linear interdependence between geometry and performance, the second script implements a scatter analysis. Hundreds of geometric configurations are generated within the defined limits ($5\,\text{mm} < D_{pt} < 100\,\text{mm}$, $1 < \Delta p_{pt} < 10$[bar], $1 < \Delta p_{ann} < 10$[bar], $0 < \theta_{pt} < 45$[°]), evaluating them with respect to three critical metrics: Sauter Mean Diameter (SMD), Vaporization Distance (X_{vap}), and Spray Angle (θ).

4.3.2 Empirical Atomization Models (SMD)

SMD is calculated via semi-empirical correlations (equation 3.16), validated for gas-liquid pintle injectors. The dominant parameter turns out to be the Weber number (We), which quantifies the ratio between inertial forces and surface cohesion forces.

4.3.3 Vaporization Modeling (X_{vap})

The vaporization distance is estimated by applying the modified D^2 law (equation 3.21).

4.3.4 Spray Angle Modeling

The spray angle is calculated using the empirical correlation (equation 2.6), dependent on TMR.

4.3.5 Scatter Analysis Results

The observed trends are the same as those seen in the article by J. Cha, E. Anderson, and A. Bohlin.

4.3.5.1 Effect of Pintle Angle

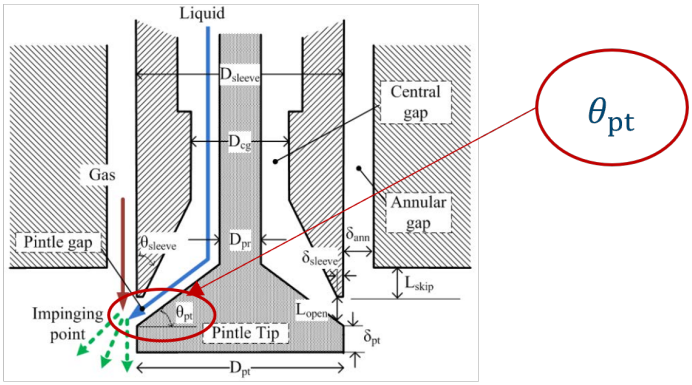

Figure 4.1: pintle angle [17]

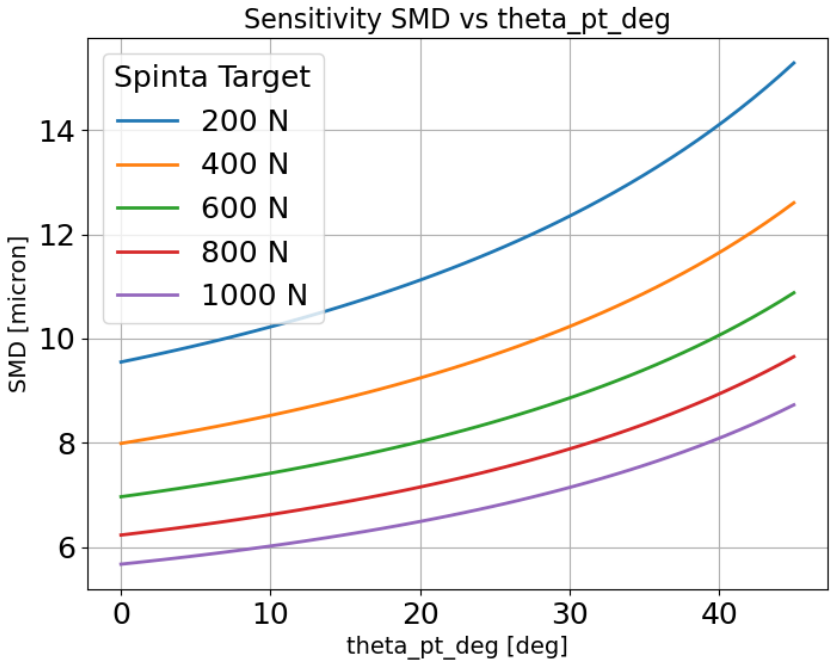

Figure 4.2: Sauter Mean Diameter (SMD) as a function of the pintle angle (θ_{pt}).

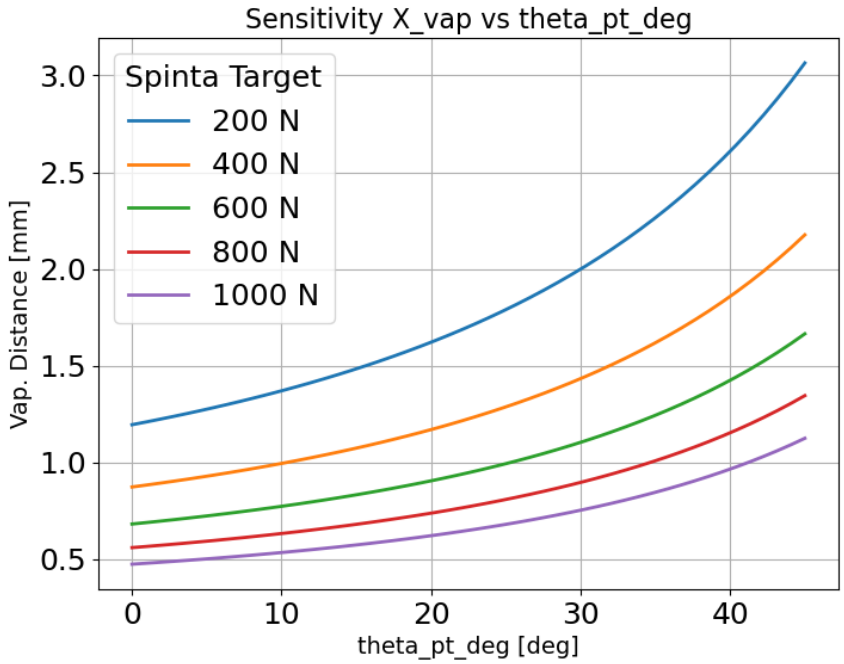

Figure 4.3: Vaporization distance (X_{vap}) as a function of the pintle angle [deg] (θ_{pt}).

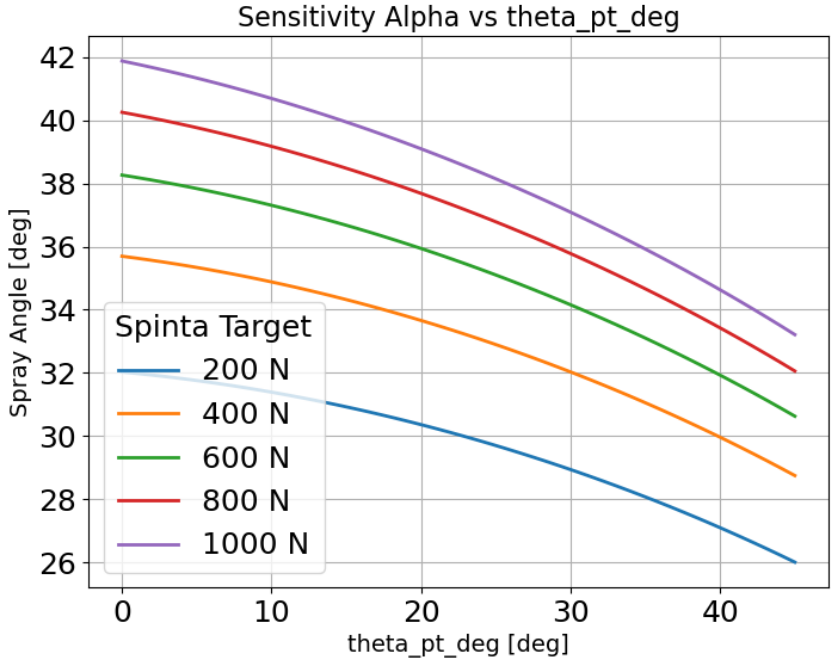

Figure 4.4: Spray angle as a function of the pintle angle (θ_{pt}).

- The SMD parameter increases as the pintle angle increases, and increases as the required thrust decreases.
- The trend of the vaporization length is identical to that of SMD.

- The spray angle decreases as the pintle angle increases and increases as the required thrust increases.

4.3.5.2 Effect of Annular Pressure Drop

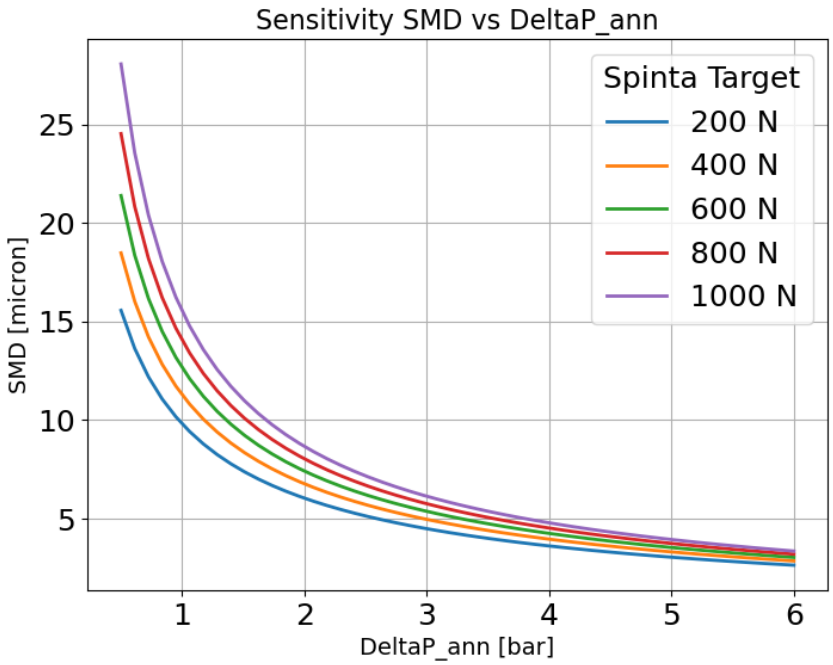

Figure 4.5: Sauter Mean Diameter (SMD) as a function of the annular pressure drop.

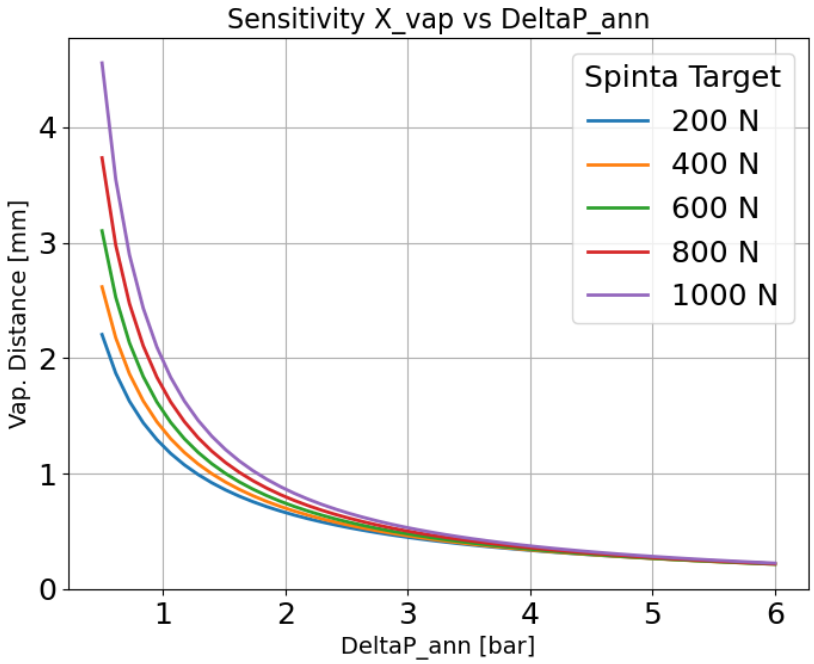

Figure 4.6: Vaporization distance (X_{vap}) as a function of the annular pressure drop.

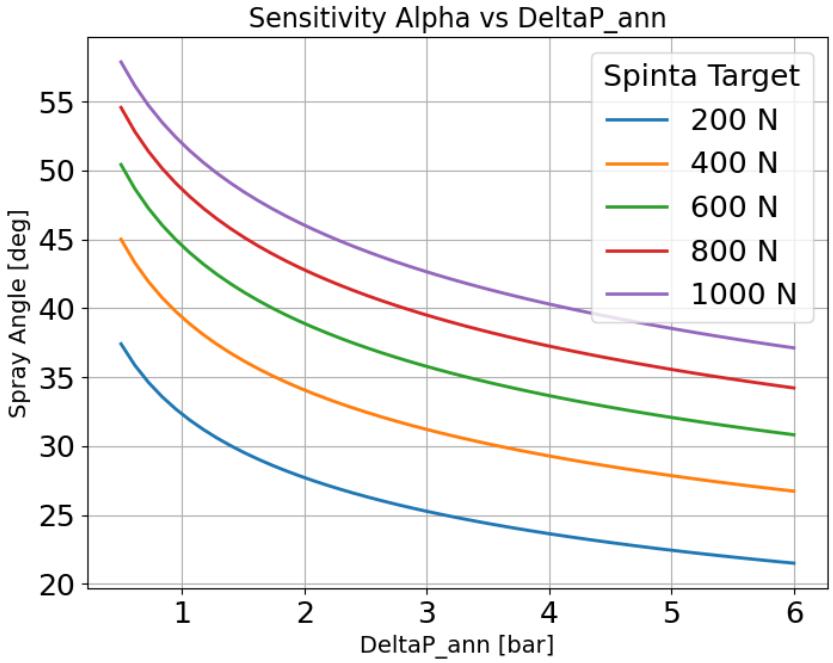

Figure 4.7: Spray angle as a function of the annular pressure drop.

- SMD decreases as Δp_{ann} increases and increases as the required thrust increases.
- The trend of the vaporization length is identical to that of SMD.
- The spray angle decreases as Δp_{ann} increases and increases as the required thrust increases.

4.3.5.3 Effect of Pintle Pressure Drop

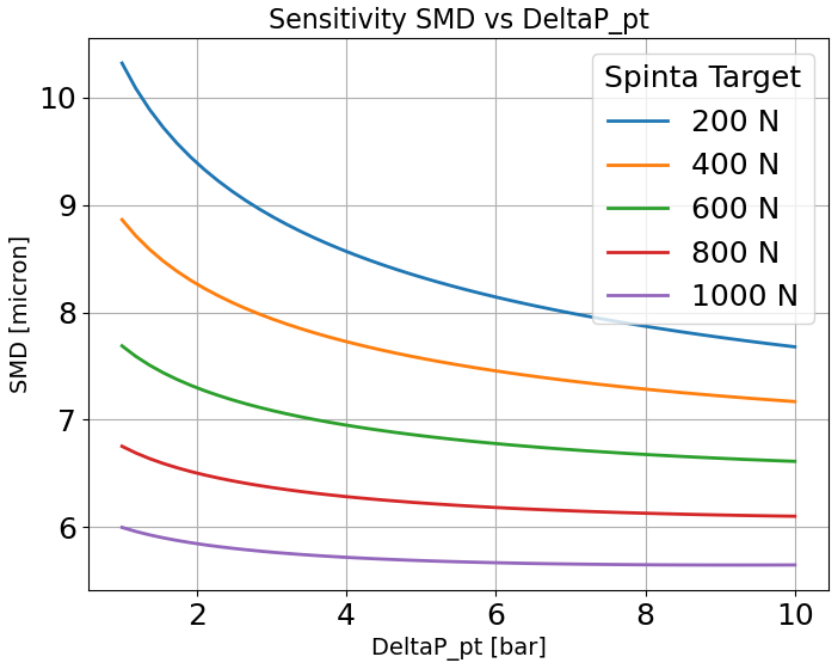

Figure 4.8: Sauter Mean Diameter (SMD) as a function of the pintle pressure drop.

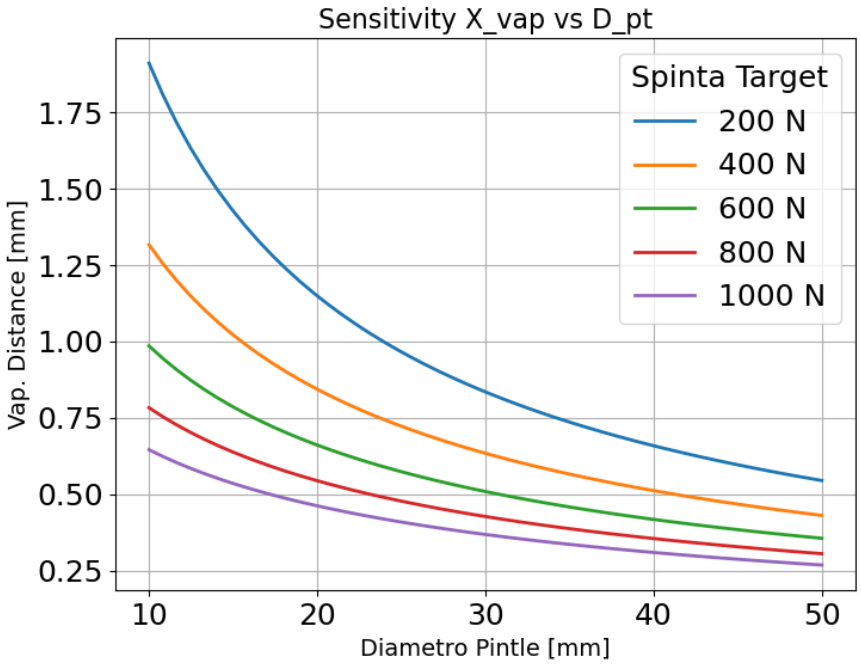

Figure 4.9: Vaporization distance (X_{vap}) as a function of the pintle pressure drop.

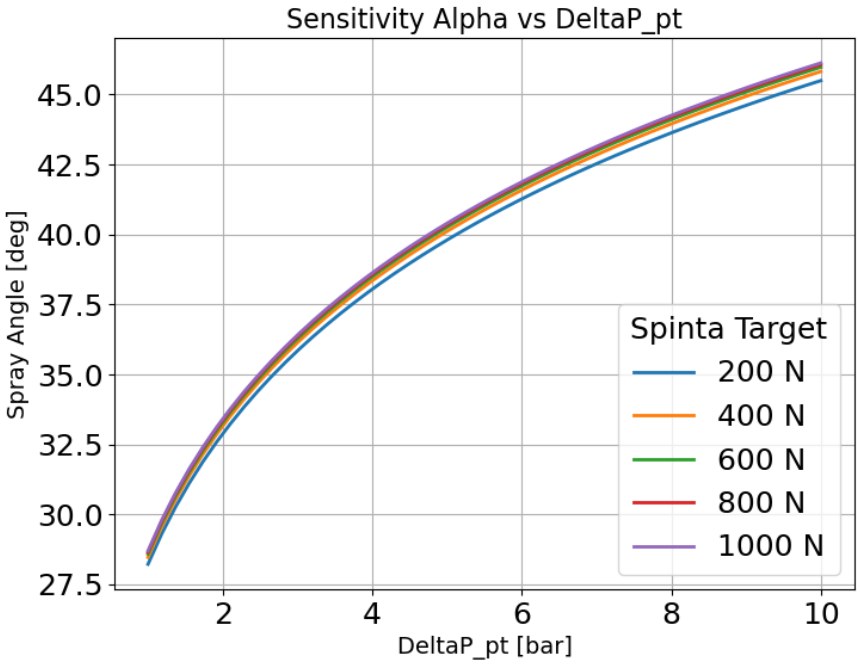

Figure 4.10: Spray angle as a function of the pintle pressure drop.

- SMD decreases as Δp_{pt} increases and increases as the required thrust decreases.
- The trend of the vaporization length is identical to that of SMD.
- The spray angle increases as Δp_{pt} increases and is independent of the required thrust.

4.3.5.4 Effect of Pintle Diameter

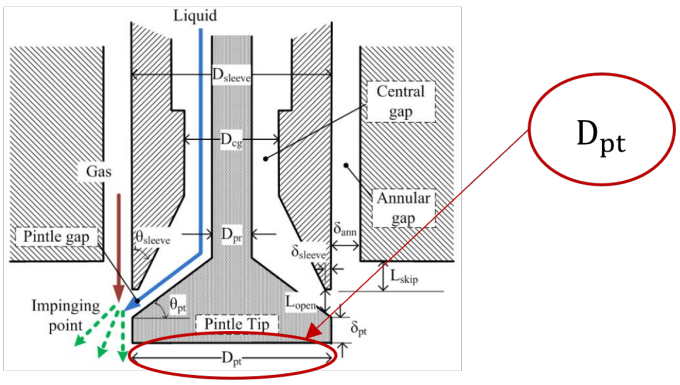

Figure 4.11: pintle diameter [17]

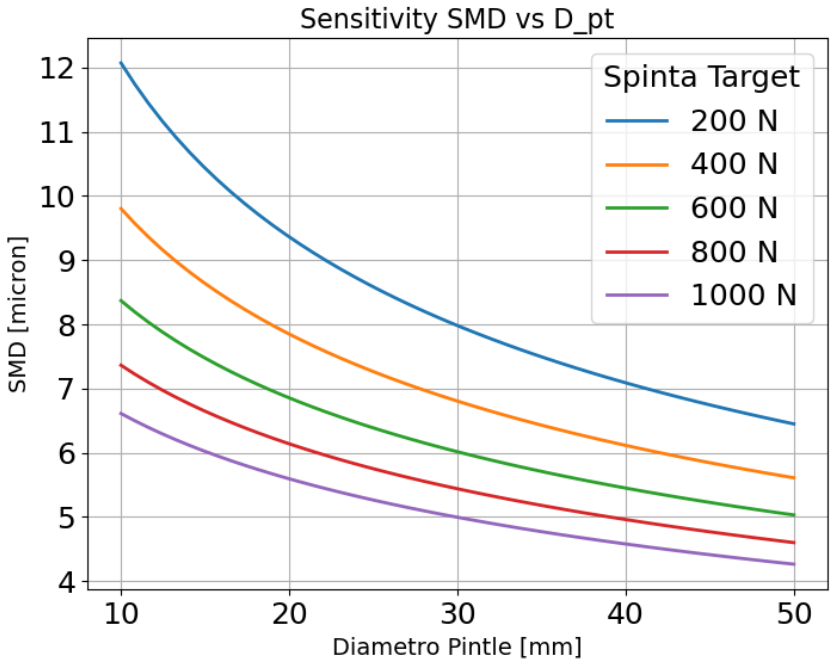

Figure 4.12: Sauter Mean Diameter (SMD) as a function of the pintle diameter (D_{pt}).

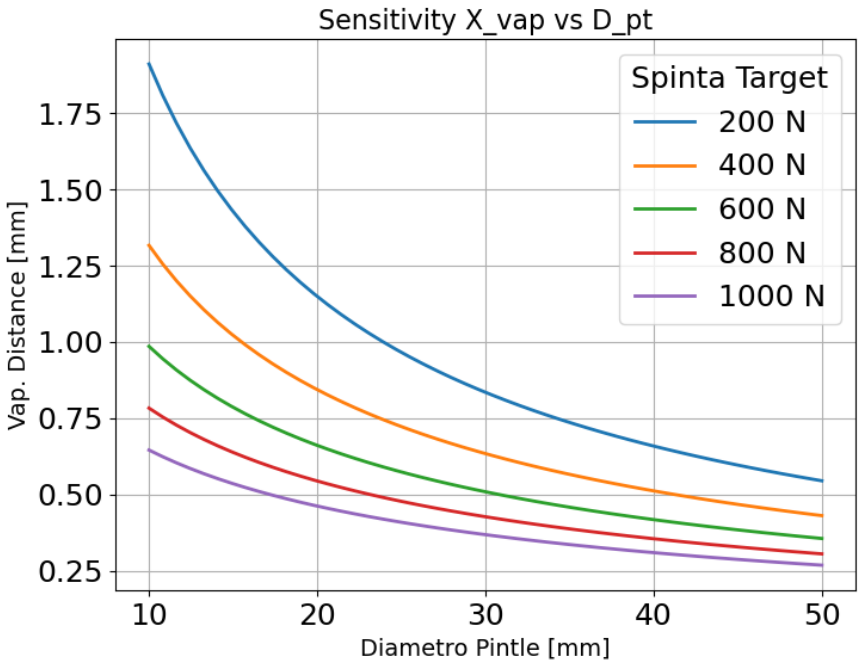

Figure 4.13: Vaporization distance (X_{vap}) as a function of the pintle diameter (D_{pt}).

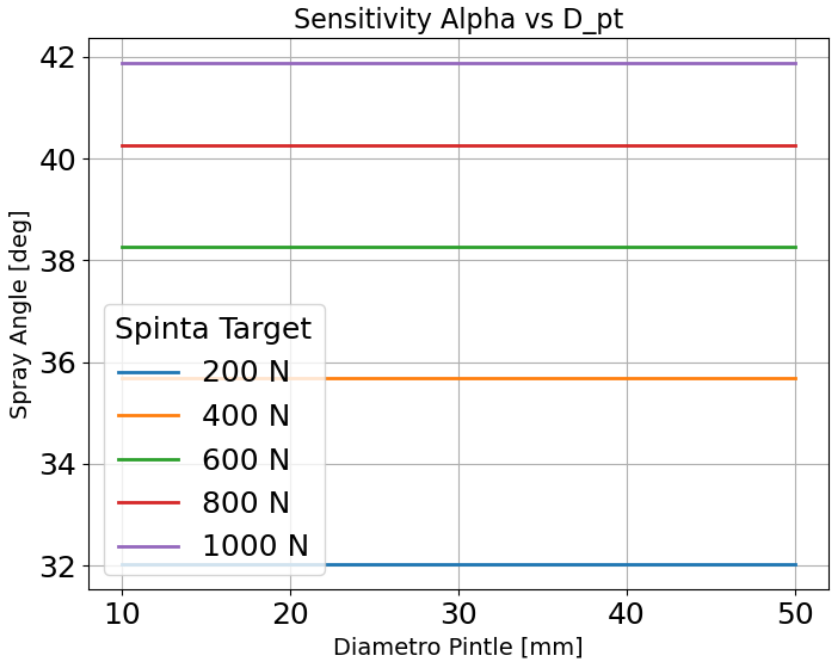

Figure 4.14: Spray angle as a function of the pintle diameter (D_{pt}).

- SMD decreases as the pintle diameter increases and increases as the required thrust decreases.
- The trend of the vaporization length is identical to that of SMD.
- The spray angle increases as the required thrust increases and is independent of the pintle diameter.

4.4 Thermal Model Integration (h_c)

The calculation of the convective heat transfer coefficient (h_c) is the innovative part of this thesis work.

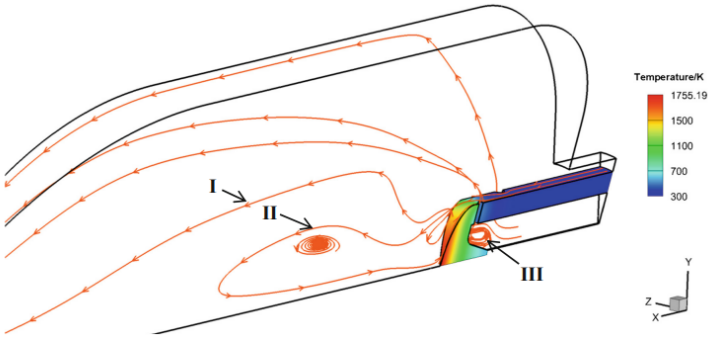

Figure 4.15: temperature field on the pintle tip [31]

4.4.1 Pintle Tip: Katti-Prabhu Correlation

The pintle tip is subject to a recirculation flow comparable to an impinging jet. The Katti and Prabhu correlation [32] is used, discretizing the surface as a function of the dimensionless radial distance r/d.

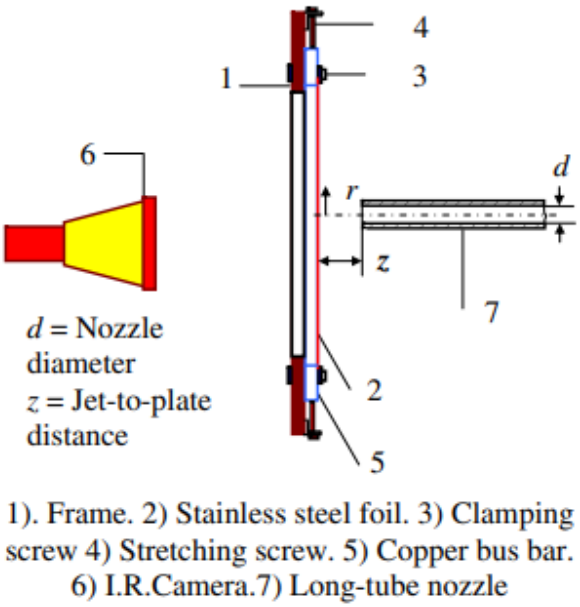

Figure 4.16: Katti and Prabhu experimental setup [32]

4.4.2 Heat Transfer Models in the Three Zones

Based on the fluid dynamic characteristics of the impinging jet, the surface can be divided into three distinct regions [32]: the stagnation region, the transition region, and the wall jet region [32].

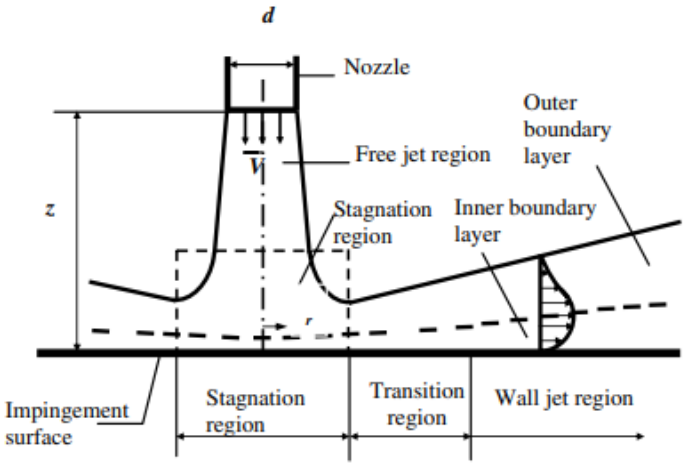

Figure 4.17: three zones of heat transfer [32]

- **Zone 1: Stagnation Region** ($0 \leq r/d \leq 1.0$)

In this zone, the local Nusselt number (Nu) can be expressed as:

$$Nu = a_1 \, Re^{1/2} \, Pr^{1/3} \left(\frac{z}{d}\right)^{-0.11} \left[1 - \frac{(r/d)^2 (z/d)^{-0.2}}{b_1}\right]^{1/2} \tag{4.5}$$

Where a_1 and b_1 are constants that vary depending on the dimensionless jet-to-plate distance (z/d)[32]. At the stagnation point ($r/d = 0$), the formula reduces to:

$$Nu_0 = a_1 \, Re^{1/2} \, Pr^{1/3} \left(\frac{z}{d}\right)^{-0.11} \tag{4.6}$$

- **Zone 2: Transition Region** ($1.0 < r/d < 2.5$)
  In this region, the flow transitions from laminar to turbulent. The empirical correlations developed for the Nusselt number are [32]:
  - For $z/d \leq 3.0$: $Nu = 0.2636 \, Re^{0.6188} \, (z/d)^{-0.0898} \, (r/d)^{-0.074}$
  - For $z/d \geq 4.0$: $Nu = 0.198 \, Re^{0.6632} \, (z/d)^{-0.3702} \, (r/d)^{-0.3702}$
- **Zone 3: Wall Jet Region** ($r/d > 2.5$)
  Heat transfer in this zone is modeled considering turbulent flow over a flat plate with constant heat flux [32]:

$$Nu = 0.0436 \, E \, Re^{0.8} \, Pr^{1/3} \left(\frac{z}{d}\right)^{0.0976} \left(\frac{r}{d}\right)^{-1.0976} \tag{4.7}$$

Where E is an *enhancement factor* varying between 2.3 and 3.0 depending on the distance z/d [32].

To quantify the z/d ratio, i.e., the distance between the nozzle and the face plate, another approximation is used, namely considering the flow created around the pintle as the flow recirculating around a backward-facing step, using the limit value of 7 which is a value found in literature as the reattachment point for turbulent flows [33].

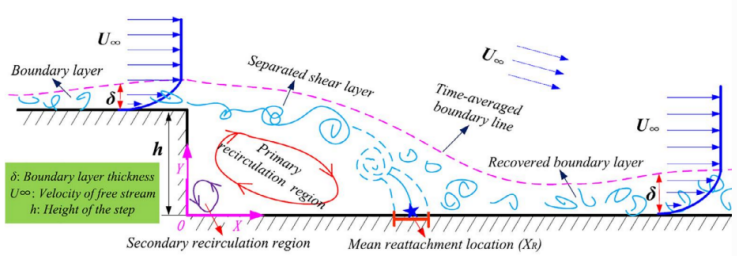

Figure 4.18: backward facing step flow [33]

4.4.2.1 Scatter Analysis Results on hc

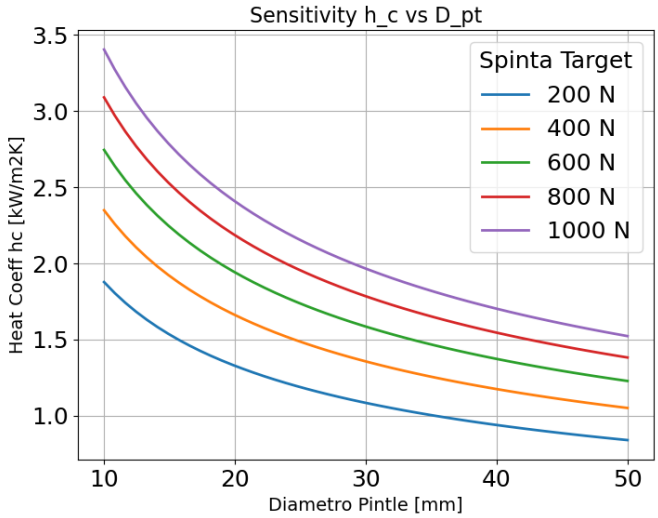

Figure 4.19: Sensitivity of hc to variations in pintle diameter

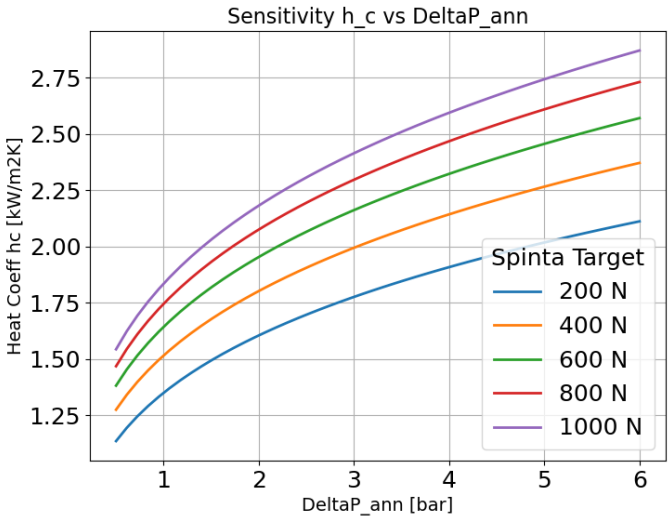

Figure 4.20: Sensitivity of hc to variations in annular pressure drop

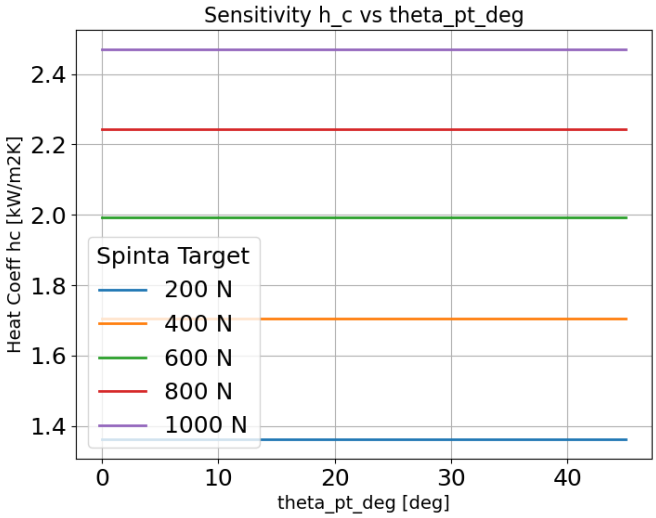

Figure 4.21: Sensitivity of hc to variations in pintle angle

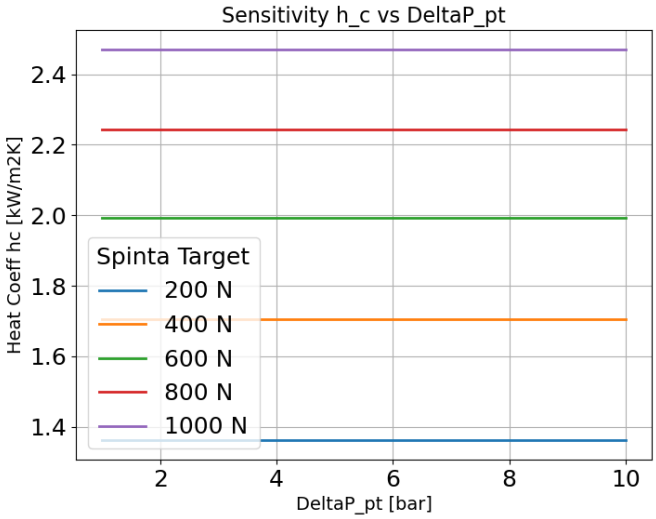

Figure 4.22: Sensitivity of hc to variations in pintle pressure drop

The convective heat transfer coefficient (h_c) on the pintle tip shows the following trends:

- It decreases as the pintle diameter increases.
- It increases as the annular pressure drop increases.
- It is independent of both the pintle pressure drop and the pintle angle.
- It increases as the required thrust increases.

The results obtained show all the limitations of the assumptions made. Therefore, it is fundamental to perform a CFD simulation to validate the results obtained with this simplified model.

4.5 Multi-Objective Optimization and 3D Visualization

4.5.1 Convex Quadratic Programming (CQP)

To select the optimal geometry, a Convex Quadratic Programming algorithm is employed. The objective is to minimize a weighted cost function (J) that combines the four performance metrics (SMD, X_{vap}, θ and h_c):

$$J = w_{SMD}\left(\frac{SMD}{SMD_{ref}}\right)^2 + w_{X_{vap}}\left(\frac{X_{vap}}{X_{vap,ref}}\right)^2 + w_{\theta}\left(\frac{\theta - \theta_{target}}{\theta_{target}}\right)^2 + w_{h_c}\left(\frac{h_c}{h_{c,ref}}\right)^2 \tag{4.8}$$

Where w_i are the optimization weights assigned to each metric, reflecting their relative importance in the specific application context. The procedure involves calculating the cost function for each point generated in the scatter analysis, selecting the configuration that minimizes J. The design variables are non-dimensionalized with respect to reference values to ensure unit consistency in the cost function. Regarding SMD, vaporization length (X_{vap}) and h_c, the goal is to minimize absolute values, while for the spray angle (θ) the aim is to maximize the value, therefore a target value (e.g., 75°) is taken and the deviation from this target is minimized.

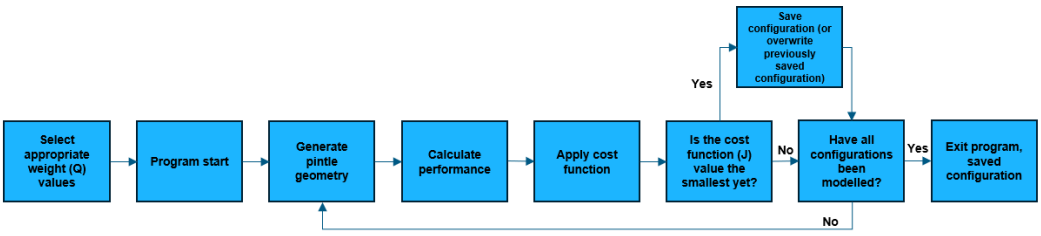

Figure 4.23: optimizer logic [17]

To reduce the solution space, linear constraints are imposed on the design variables.

- **Pressure Drop Constraint:** to prevent low-frequency instability phenomena and ensure decoupling between the feed system and the combustion chamber, a limit is imposed on the relative injection pressure drop [17]:

$$0.05 \leq \frac{\Delta P}{P_c} \leq 0.3 \tag{4.9}$$

- **Minimum Pintle Opening (L_{open}):** in order to ensure component physical manufacturability and flow control precision during throttling, a lower limit is imposed on the pintle opening [17]:

$$L_{open} \geq 0.1\,\text{mm} \tag{4.10}$$

- **Pintle Geometric Limits (D_{pt} and δ_{ann}):** The solution search space is

limited for reasons of size and scalability of the demonstrator engine, defining a range for the tip diameter ($5\,\text{mm} < D_{pt} < 100\,\text{mm}$) and for the gaseous annulus thickness ($0.01\,\text{mm} < \delta_{ann} < 6\,\text{mm}$) [17].

The integration of these constraints within the CQP algorithm allows for identifying "stability plateaus" analyzed through 3D visualization, ensuring that the optimal geometry is not located in proximity to critical or unfeasible regimes.

4.5.2 Optimization Philosophies

The injector design was obtained through a multi-objective optimization procedure in which several performance indicators were simultaneously considered. Different optimization philosophies were explored by assigning different weights to the objective function components. These weights allow the design process to emphasize specific performance aspects, such as improved atomization, reduced vaporization length, increased spray angle, or reduced thermal loads on the injector surfaces.

Table 4.2 summarizes the main optimization philosophies investigated in this work together with the corresponding weighting factors used in the cost function.

Table 4.2: Optimization philosophies considered in the design procedure

Philosophy	Q_D	Q_X	Q_α	$Q_{hc,pi}$
Balanced (baseline)	1	1	1	1
High spray angle priority	1	1	5	0
Thermal load reduction	1	1	1	2

4.5.3 Sensitivity Analysis in Weight Space

After setting up the scatter analysis, a 3D visualization script was implemented to study the optimization weights (w_i). In this analysis, the heat transfer coefficient was not included as a performance metric, as it would have required an additional dimension in the visualization, complicating result interpretation.

4.5.3.1 3D Visualization Results

The following figures show the response surfaces in the solution space obtained by fixing one of the three optimization weights and varying the other two. These graphs allow for identifying regions of stability of the optimal solution in relation to the weights assigned to each performance metric.

4.5.3.1.1 Impact on Spray Angle

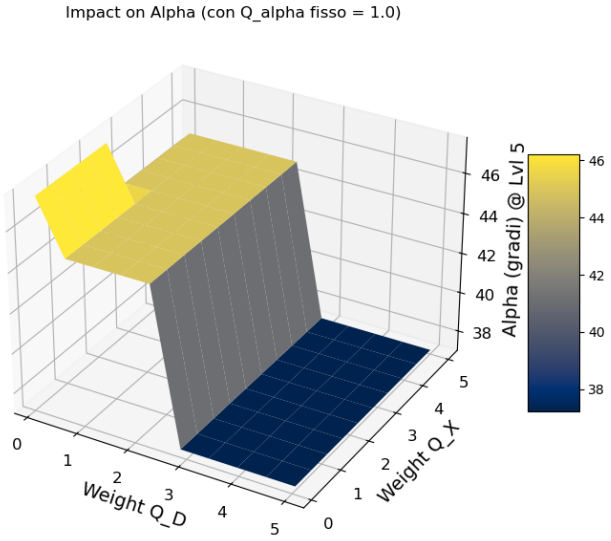

Figure 4.24: spray angle solution space fixing the weight of α [17]

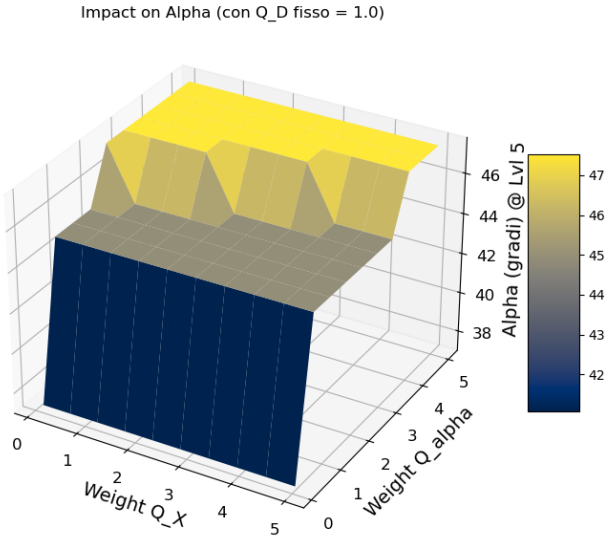

Figure 4.25: spray angle solution space fixing the weight of SMD [17]

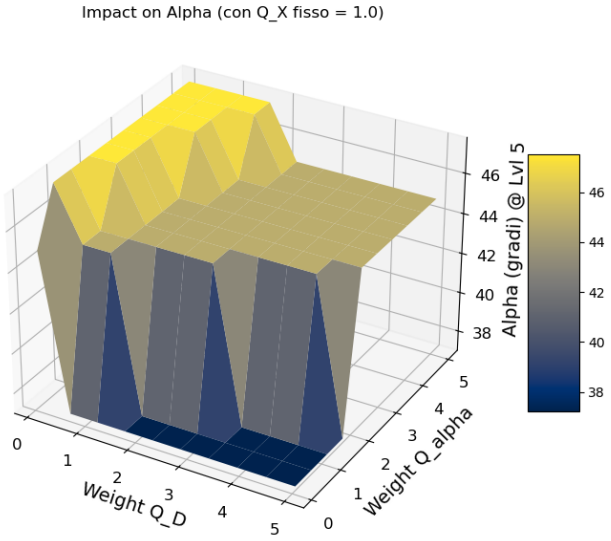

Figure 4.26: spray angle solution space fixing the weight of X_{vap} [17]

- Spray angle decreases as the weight of SMD increases and is independent of the weight of Xvap.
- Spray angle decreases as the weight of the spray angle decreases and is independent of the weight of Xvap.
- Spray angle decreases as the weight of the spray angle decreases and decreases as the weight of SMD increases.

4.5.3.1.2 Impact on SMD

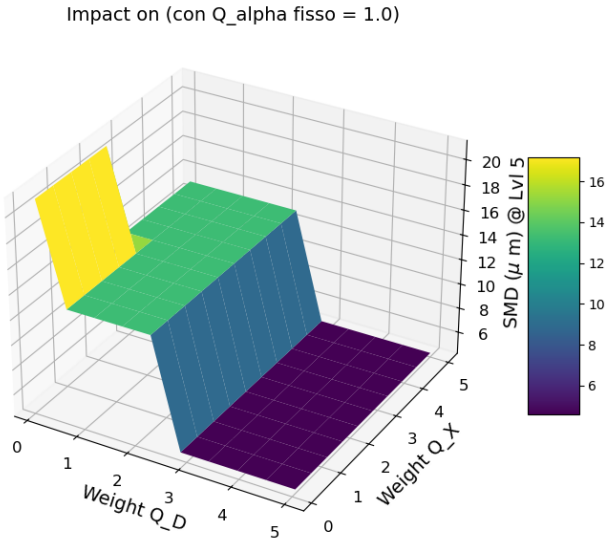

Figure 4.27: SMD solution space fixing the weight of α [17]

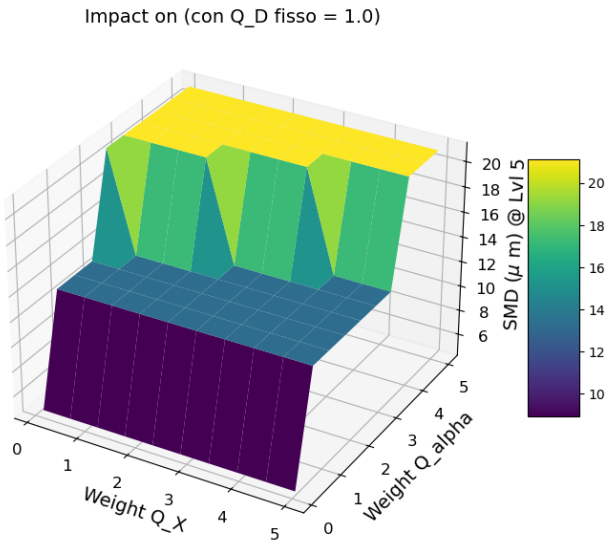

Figure 4.28: SMD solution space fixing the weight of SMD [17]

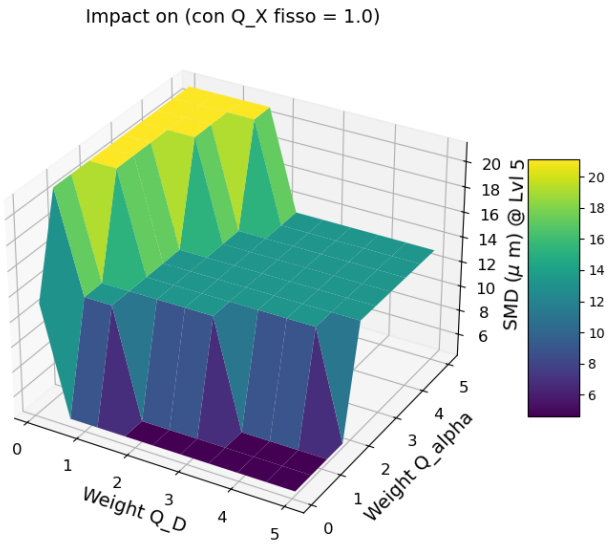

Figure 4.29: SMD solution space fixing the weight of X_{vap} [17]

- SMD decreases as the weight of SMD increases and is independent of the weight of Xvap.
- SMD decreases as the weight of the spray angle decreases and is independent of the weight of Xvap.
- SMD decreases as the weight of SMD increases and decreases as the weight of the spray angle decreases.

4.5.3.1.3 Impact on Xvap

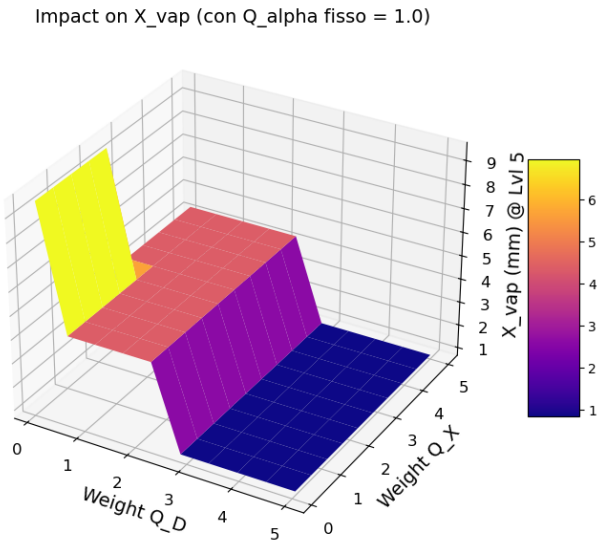

Figure 4.30: X_{vap} solution space fixing the weight of α [17]

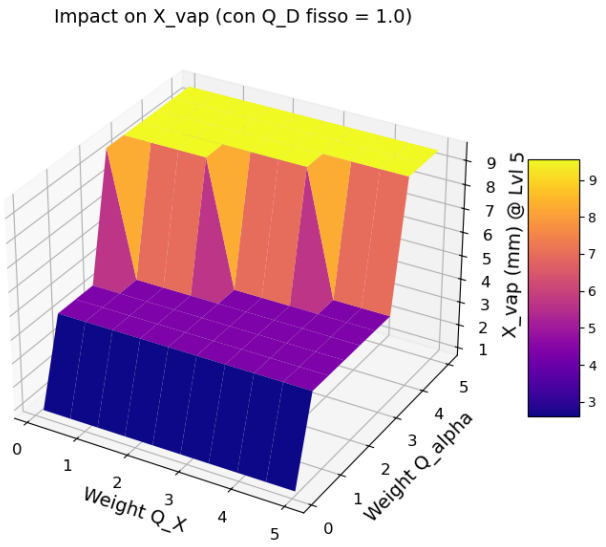

Figure 4.31: X_{vap} solution space fixing the weight of SMD [17]

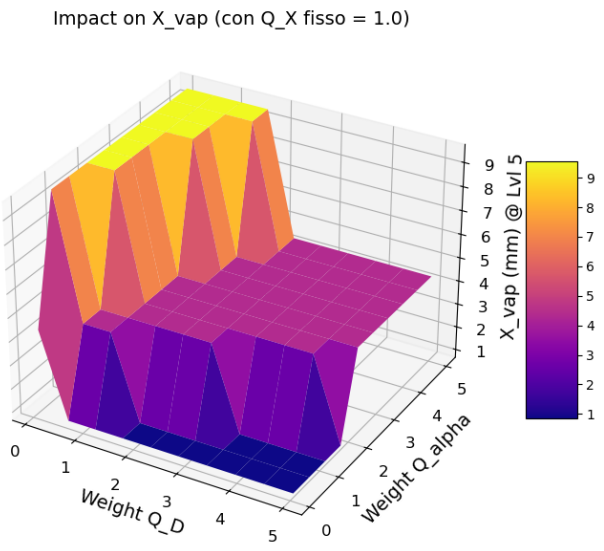

Figure 4.32: X_{vap} solution space fixing the weight of X_{vap} [17]

- X_{vap} decreases as the weight of SMD decreases and is independent of the weight of X_{vap}.
- X_{vap} decreases as the weight of spray angle decreases and is independent of the weight of X_{vap}.
- X_{vap} decreases as the weight of SMD decreases and decreases as the weight of the spray angle decreases.

The sensitivity analysis indicates that the balanced weighting configuration lies within a relatively stable region of the solution space.

For this reason, the balanced philosophy was selected as the baseline configuration for the injector design and for the subsequent analyses presented in this work.

4.5.4 Optimization Results for the Baseline Philosophy

After selecting the balanced optimization philosophy as the reference configuration, the corresponding injector parameters were analyzed across the considered thrust range.

The optimization was performed for five thrust levels between 200 N and 1000 N while maintaining the same propellant combination (LOX/CH_4) and mixture ratio. The main results obtained for the baseline philosophy are summarized in Table 4.3.

Table 4.3: Main injector parameters obtained from the baseline optimization philosophy

Thrust [N]	Pc [bar]	SMD [μm]	Spray angle [°]	X_{vap} [mm]	L_c [mm]	q_{pintle} [MW/m^2]
200	5.52	11.50	29.85	3.07	22.29	1.08
400	9.39	9.07	33.53	1.94	21.28	1.36
600	12.93	7.75	35.87	1.44	20.85	1.65
800	16.46	6.83	37.72	1.13	20.60	1.89
1000	20.00	6.15	39.24	0.92	20.44	2.10

The results show several clear trends as the thrust level increases.

First, the chamber pressure increases from approximately 5.5 bar to 20 bar in order to sustain the higher thrust levels. This increase in chamber pressure leads to higher injection velocities and improved atomization.

As a consequence, the Sauter Mean Diameter decreases significantly with increasing thrust, from approximately 11.5 μm at 200 N to about 6 μm at 1000 N. This reduction indicates a more efficient breakup process at higher operating conditions.

At the same time, the spray angle progressively increases from about 30° to nearly 40°, promoting enhanced mixing between the propellant streams.

The vaporization length also decreases with increasing thrust level, mainly due to the combined effects of smaller droplet diameters and higher gas velocities, which accelerate the evaporation process.

However, these improvements in atomization and vaporization are accompanied by an increase in thermal loads acting on the pintle tip. The predicted wall heat flux rises from approximately 1 MW/m^2 at the lowest thrust condition to slightly above 2 MW/m^2 at the highest thrust level.

These results highlight the typical trade-off encountered in injector design: higher operating pressures improve atomization and mixing but simultaneously increase the thermal loads acting on the injector components.

Chapter 5

Numerical Modeling of Two-Phase Flows

The design of high-performance injection systems for space propulsion today requires a fundamental methodological transition: overcoming simplified analytical models in favor of computational fluid dynamics (CFD) simulations. Although 0D models, based on the fundamental relations of ideal rocket propulsion, provide a solid basis for preliminary geometric sizing, they present significant intrinsic limitations. These approaches, in fact, are unable to capture the complex physics characterizing a pintle injector, particularly regarding:

- the dynamics of two-phase flows;
- primary and secondary atomization processes;
- the turbulent interactions that define the combustion efficiency and thermal stability of the system.

This chapter aims to detail the theoretical and mathematical framework necessary for modeling the spray produced by a *pintle* injector, focusing on the Eulerian-Lagrangian approach.

5.1 Theoretical Framework for Spray Modeling

The numerical analysis proposed here adopts a decoupled description for the involved phases. The gaseous phase (carrier phase) is treated according to an Eulerian perspective by solving the fluid dynamics governing equations, while the dispersed phase (propellant droplets) is tracked through a Lagrangian approach. In this context, the discussion will delve into the following key aspects.

1. **Governing Equations:** formulation of conservation equations for the gaseous phase and definition of source terms deriving from the interaction with the liquid phase.
2. **Phenomenological Laws:** analysis of the behavior of individual droplets, with particular reference to kinematics and mass and heat transport processes.

3. **Vaporization Models:** implementation of the D^2 law to describe the temporal evolution of droplet diameter.

4. **Heat Transfer:** use of the Ranz-Marshall correlation for the determination of exchange coefficients in a convective environment.

This modeling apparatus allows for accurately characterizing the evolution of the spray and its subsequent mixing, which are determining elements for the overall performance of the thruster.

5.2 The Eulerian-Lagrangian Model

The Eulerian-Lagrangian approach is based on the discretization of the dispersed phase into a set of representative particles, or parcels, each of which embodies the average properties of a group of real droplets. These particles are tracked in the fluid domain, while the continuous phase is resolved via the Navier-Stokes equations modified to include particle effects. When a liquid jet interacts with a gaseous fluid, it breaks first into filaments and subsequently into droplets, a process known as atomization. This entire process is induced by instabilities known as Kelvin-Helmholtz and Rayleigh-Taylor instabilities [34]. Once formed, the droplets undergo further secondary fragmentation processes, which contribute to defining the spray's size distribution. The Kelvin-Helmholtz instability manifests due to the velocity difference between the liquid and the surrounding gas, while the Rayleigh-Taylor instability occurs when a denser fluid (liquid) is accelerated into a less dense fluid (gas). These instabilities contribute to the primary atomization process, i.e., the initial breakup of the liquid jet into filaments and droplets. Subsequently, droplets may undergo a secondary atomization process, in which larger droplets fragment further into smaller droplets due to aerodynamic forces exerted by the surrounding gaseous flow. In this thesis work, secondary atomization will not be modeled. External forces act on the droplet surface opposing the surface attraction forces that tend to keep the droplet cohesive, the resultant of which is called surface tension σ. In a two-phase flow, we can distinguish three main interaction regimes between the two phases.

- **Dense Regime:** particles are close enough to influence each other, but do not touch. In this case, it is necessary to consider interaction effects between particles, such as collision and aggregation.

- **Dilute Regime:** particles are sufficiently distant from each other not to influence one another. In this case, the interaction between particles and the continuous phase can be modeled by considering only the forces exerted by the fluid on the single particle.

- **Very Dilute Regime:** particles are so distant from each other that the interaction between particles and the continuous phase can be neglected. In this case, particles can be treated as independent entities moving in the fluid without influencing each other.

The three different regions are characterized by a range of particle fractional volume Φ:

$$\Phi_l = \frac{V_l}{V_{tot}} \tag{5.1}$$

with V_l being the total volume of liquid particles and V_{tot} the total volume of the considered domain. The following table summarizes the classification of regimes as a function of the volumetric fraction [34]:

Table 5.1: Classification of flow regimes for sprays as a function of volumetric fraction.

Flow Regime	**Volumetric Fraction** (Φ_l)
Dense Spray	$\Phi_l > 10^{-3}$
Dilute Spray	$10^{-6} < \Phi_l < 10^{-3}$
Very Dilute Spray	$\Phi_l < 10^{-6}$

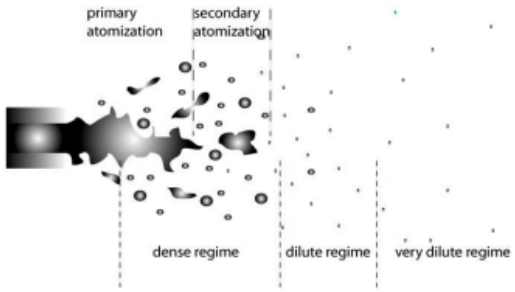

Figure 5.1: Schematization of flow regimes in a spray and the primary and secondary atomization process [34]

5.2.1 Governing Equations

The continuous gaseous phase is described by the Reynolds-Averaged Navier-Stokes (RANS) equations. These equations express the conservation of mass, momentum, energy and chemical species, including source terms that account for the interaction with the dispersed phase.

$$\frac{\partial \rho}{\partial t} + \nabla \cdot (\rho \mathbf{u}) = S_m \tag{5.2a}$$

$$\frac{\partial (\rho \mathbf{u})}{\partial t} + \nabla \cdot (\rho \mathbf{u} \otimes \mathbf{u}) = \nabla \cdot \tau - \nabla p + \mathbf{S}_p \tag{5.2b}$$

$$\frac{\partial \rho E}{\partial t} + \nabla \cdot (\rho \mathbf{u} E) = -\nabla \cdot \mathbf{q} + \nabla \cdot (\sigma \cdot \mathbf{u}) + S_e + \rho \sum_{i=1}^{N_c} \omega_i \bar{f}_i (\mathbf{u} + V_i) \tag{5.2c}$$

Where the terms appearing in the classical formulation of the Navier-Stokes equations are defined as follows:

- **continuity Equation** (5.2a)**:** ρ represents the fluid density and $\mathbf{u}$ the velocity vector. The term S_m is the mass source due to droplet evaporation;

- **momentum Equation** (5.2b)**:** the term $\nabla \cdot \tau$ represents the viscous stress tensor, ∇p the pressure gradient, and $\mathbf{S}_p$ the momentum source term (exchange of drag forces between phases);
- **energy Equation** (5.2c)**:** E is the total energy per unit mass.
  - $\nabla \cdot \mathbf{q}$: describes heat flow by conduction (Fourier's law):

$$\mathbf{q} = -k\nabla T \tag{5.3}$$

  - $\nabla \cdot (\sigma \cdot \mathbf{u})$: represents the work done by surface forces.
  - S_e: is the thermal energy source term due to sensible and latent heat exchange.
  - $\rho \sum \omega_i \bar{f}_i(\mathbf{u}+V_i)$: represents the energy contribution deriving from external forces and concentration gradients of chemical species.

To complete the description of the fluid field in the presence of evaporation, it is necessary to solve the transport equation for the mass fraction of the vaporized species Y_v. This equation governs the conservation of mass of the chemical species dispersed within the gaseous mixture:

$$\frac{\partial(\rho Y_v)}{\partial t} + \nabla \cdot (\rho \mathbf{u} Y_v) = \nabla \cdot (\rho \mathcal{D} \nabla Y_v) + S_m^p \tag{5.4}$$

In this instantaneous formulation, the terms assume the following physical meaning:

- $\mathcal{D}$: is the effective diffusion coefficient of the gaseous species in the carrier medium.
- The first term on the right represents the diffusive transport of the chemical species, modeled according to Fick's law [35]:

$$J = -\rho \mathcal{D} \nabla Y_v - \frac{\mu}{Sc} \nabla Y_v \tag{5.5}$$

$$Sc = \frac{\mu}{\rho \mathcal{D}} \tag{5.6}$$

Equation (5.4) allows coupling the spray dynamics with the local chemical composition of the gas, a fundamental parameter for the subsequent analysis of the combustion process. The system of governing equations previously exposed requires a set of constitutive relations for the closure of the thermofluid dynamic problem. Assuming perfect gas behavior for the gaseous phase, the relative equation of state is adopted:

$$p = \rho R T \tag{5.7}$$

where p is thermodynamic pressure, T temperature, and R the specific gas constant. For a calorically perfect gas, the specific internal energy e is linked to temperature by the relation:

$$e = c_v T \tag{5.8}$$

with c_v being the specific heat at constant volume. The specific total energy E, which appears in equation (5.2c), is defined as the sum of internal energy and macroscopic kinetic energy of the fluid:

$$E = e + \frac{|\mathbf{q}|^2}{2} \tag{5.9}$$

Regarding the transport model, Sutherland's model is adopted for the dynamic viscosity of the gas as a function of temperature:

$$\mu = \frac{As\sqrt{T}}{1 + \frac{T}{Ts}} \tag{5.10}$$

Where As and Ts are constants specific to the considered gas. For the thermodynamic model, the specific heat at constant pressure c_p is calculated as a function of temperature via a polynomial correlation. The Janaf model is used, which expresses c_p as:

$$c_p = R\left(a_1 + a_2 T + a_3 T^2 + a_4 T^3 + a_5 T^4\right) \tag{5.11}$$

Where the coefficients a_1, a_2, a_3, a_4, and a_5 are specific for each chemical species and are derived from thermodynamic tables, while R is the specific gas constant. Finally, the system is coupled to the dispersed phase through the source terms S_m, $\mathbf{S}_p$, and S_e. These terms represent, respectively, the rates of change of mass, momentum, and energy exchanged between the Lagrangian parcels and the carrier gas:

$$S_m = -\sum_{i=1} \frac{dm_{d,i}}{dt} \delta(\mathbf{x} - \mathbf{x}_{d,i}) \tag{5.12}$$

$$\mathbf{S}_p = -\sum_{i=1} \frac{d(m_{d,i}\mathbf{u}_{d,i})}{dt} \delta(\mathbf{x} - \mathbf{x}_{d,i}) \tag{5.13}$$

$$S_e = -\sum_{i=1} \frac{d(m_{d,i} c_l T_{d,i})}{dt} \delta(\mathbf{x} - \mathbf{x}_{d,i}) \tag{5.14}$$

Where:

- $m_{d,i}$, $\mathbf{u}_{d,i}$, and $T_{d,i}$ are respectively the mass, velocity vector, and temperature of the i-th droplet.
- c_l is the specific heat of the liquid.
- The negative sign indicates that a variation of a property in the liquid phase translates into a source term of opposite sign for the gaseous phase (e.g., mass lost by the droplet due to evaporation is acquired by the gas).

5.2.1.1 Turbulence Modeling

As the Reynolds number increases, gaseous flows tend to become turbulent, characterized by vortices and velocity fluctuations over a wide range of scales. To capture these effects in CFD models, it is necessary to adopt an adequate turbulence model. To resolve all turbulence scales, it would be necessary to adopt a Direct Numerical Simulation (DNS) approach, which is, however, computationally prohibitive for most practical applications. Therefore, recourse is made to turbulence models that approximate the effects of turbulence on mean flow quantities. In particular, in this work, a RANS (Reynolds-Averaged Navier-Stokes) model is used to describe the mean behavior of the turbulent flow. It consists of averaging the Navier-Stokes equations over time, introducing additional terms representing turbulence effects. Adopting the RANS model, any physical quantity ϕ is decomposed into a time average $\overline{\phi}$ and a fluctuation ϕ' according to the following relation:

$$\phi = \overline{\phi} + \phi' \tag{5.15}$$

Where:

- $\overline{\phi}$ is the time average of the physical quantity ϕ.
- ϕ' represents the fluctuation around the mean.
- The time average is defined as:

$$\overline{\phi} = \frac{1}{T}\int_{t}^{t+T} \phi(\tau)d\tau \tag{5.16}$$

  with T representing the time interval over which the average is performed.

This averaging procedure introduces the Reynolds stress into the convective terms of the Navier-Stokes equations, representing the contribution of turbulent fluctuations to the flow momentum.

$$R_{ij} = -\rho\overline{u_i' u_j'} \tag{5.17}$$

This term requires a closure model to be calculated, and for this reason, turbulence models such as the (k-ε) or (k-ω) model are adopted. As a trade-off between computational cost and accuracy, the (k-ε) model is used, which introduces two additional transport equations for turbulent kinetic energy k and its dissipation ε. These equations allow calculating the turbulent velocity field and determining the turbulent viscosity coefficients necessary to close the Reynolds-Averaged Navier-Stokes equations.

$$\frac{\partial(\rho k)}{\partial t} + \nabla \cdot (\rho \mathbf{u} k) = \nabla \cdot \left(\left(\mu + \frac{\mu_t}{\sigma_k} \right) \nabla k \right) + P_k - \rho\varepsilon + Y_M \tag{5.18}$$

$$\frac{\partial(\rho \varepsilon)}{\partial t} + \nabla \cdot (\rho \mathbf{u} \varepsilon) = \nabla \cdot \left(\left(\mu + \frac{\mu_t}{\sigma_\varepsilon} \right) \nabla \varepsilon \right) + C_{1\varepsilon}\frac{\varepsilon}{k}P_k - C_{2\varepsilon}\rho\frac{\varepsilon^2}{k} \tag{5.19}$$

Where:

- P_k is the turbulent kinetic energy production term.
- Y_M represents the contribution to turbulence production due to density variation in the flow.
- μ_t is the turbulent viscosity, calculated as:

$$\mu_t = C_\mu \rho \frac{k^2}{\varepsilon} \tag{5.20}$$

- C_μ, $C_{1\varepsilon}$, $C_{2\varepsilon}$, σ_k, and σ_ε are empirical constants of the model.

Once the equations are integrated, the turbulent viscosity μ_t can be calculated, which is used to calculate the viscous stress tensor τ in the Navier-Stokes equations.

$$\tau_{ij}^R = \rho \overline{u_i' u_j'} \tag{5.21}$$

$$\tau_{ij}^R = 2\mu_T \overline{S}_{ij} - \frac{2}{3}\mu_T (\nabla \cdot \overline{u})\delta_{ij} - \frac{2}{3}\rho k \delta_{ij} \tag{5.22}$$

with:

- $\overline{S}_{ij} = \frac{1}{2}\left(\frac{\partial \overline{u_i}}{\partial x_j} + \frac{\partial \overline{u_j}}{\partial x_i}\right)$ representing the averaged strain rate tensor.
- $2\mu_T \overline{S}_{ij}$ representing the anisotropic component.
- $-\frac{2}{3}\mu_T (\nabla \cdot \overline{u})\delta_{ij}$ is the isotropic component.
- k is the turbulent kinetic energy.

Finally, $\tau_{eff} = \tau + \tau^R$ is the effective viscous stress tensor that accounts for both molecular and turbulent viscosity [35].

5.2.2 Droplet Dynamics

The equations governing droplet dynamics are the same as Newtonian mechanics, adapted to account for specific forces acting on particles in a two-phase flow.

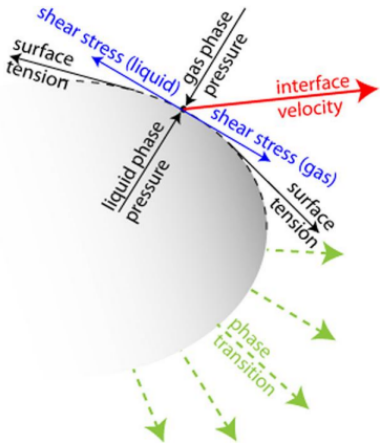

Figure 5.2: scheme of forces, mass and heat exchanged at a liquid-gas interface [34]

The trajectory of each droplet is calculated by solving the equations of motion, which include drag forces, gravity, and other relevant forces. In this context, collision and condensation phenomena are neglected.

$$\frac{d\mathbf{m_d}}{dt} = \dot{m}_d \tag{5.23}$$

where $\mathbf{m_d}$ is the mass and $\dot{\mathbf{m}}_\mathbf{d}$ is the mass source.

$$m_d \frac{\mathbf{u_d}}{dt} = \mathbf{F} \tag{5.24}$$

with F representing the sum of forces acting on the droplet. To determine the droplet position over time, the kinematic equation is solved:

$$\frac{d\mathbf{x_d}}{dt} = \mathbf{u_d} \tag{5.25}$$

where $\mathbf{x_d}$ is the droplet position. This is the approach termed '2-way coupling', in which droplets influence the fluid field and vice versa. There are two other approaches, which are '1-way coupling', where only the fluid field influences the droplets, and '4-way coupling', which also includes interactions between the droplets themselves, such as collisions and aggregations. However, to reach a compromise between accuracy and computational cost, '2-way coupling' is used.

5.2.3 Droplet Vaporization Model: D² Law

To model droplet vaporization, hence the variation of mass over time (equation: 5.23), the D^2 law is adopted, which describes the decrease in droplet diameter over time due to evaporation. The law states that the square of the droplet diameter decreases linearly with time. The main assumptions underlying this model are:

- The droplet is spherical and maintains its shape during evaporation.
- Droplet temperature is uniform and constant over time.

- Evaporation occurs under steady flow conditions.

From the Young-Laplace law, the pressure difference between the inside and outside of the droplet is given by:

$$\Delta P = P_{in} - P_{out} = -\frac{2\sigma}{r_d} \tag{5.26}$$

where σ is the surface tension and r_d the droplet radius. When the droplet radius is small, the internal pressure increases, favoring evaporation. The mass continuity equation for the droplet is:

$$\dot{m}_d = -4\pi r^2 \rho u \tag{5.27}$$

with ρ gas density assumed to be much lower than the liquid density [34]. Equation 5.27 can be rewritten as follows:

$$\frac{dm_d}{dt} = -4\pi r^2 \rho u Y_{fuel} + 4\pi r^2 \rho \mathcal{D}_{fuel} \frac{\partial Y_{fuel}}{\partial r} \tag{5.28}$$

Assuming a steady state, we obtain the following equation:

$$\frac{\partial}{\partial r}\left(\dot{m}_d Y - 4\pi r^2 \rho D \frac{\partial Y}{\partial r}\right) = 0 \tag{5.29}$$

with boundary conditions:

$$Y(r = r_d) = Y_s \tag{5.30}$$

$$Y(r \to \infty) = Y_\infty \tag{5.31}$$

Assuming ρD constant, equation 5.28 is solved as:

$$Y(r) = Y_s + (Y_\infty - Y_s) \frac{\exp\left(\frac{-\dot{m}_d}{4\pi r_d \rho D}\right)\left(1 - \frac{r_d}{r}\right) - 1}{\exp\left(\frac{-\dot{m}_d}{4\pi r_d \rho D}\right) - 1} \tag{5.32}$$

$$\dot{m}_d = \dot{m}_d Y_s + 4\pi r^2 \left[\rho D \frac{\partial Y}{\partial r}\right]_{r=r_d} = \dot{m}_d Y_s + \dot{m}_d (Y_s - Y_\infty) \frac{1}{\exp\left(\frac{-\dot{m}_d}{4\pi r_d \rho D}\right) - 1} \tag{5.33}$$

$$\dot{m}_d = -4\pi r_d \rho D \ln(1 + B_M) \tag{5.34}$$

with $B_M = \frac{Y_s - Y_\infty}{1 - Y_s}$ Spalding number for mass. Substituting the droplet mass $m_d = \frac{4}{3}\pi r_d^3 \rho_d$ and applying the derivative to equation 5.34, we obtain the D^2 law:

$$\frac{d(D^2)}{dt} = -8\frac{\rho D}{\rho_d} \ln(1 + B_M) = -K_v \tag{5.35}$$

valid in a stationary environment. To account for the relative velocity of the particle, equation 5.35 is modified [34]:

$$\frac{d(D^2)}{dt} = -8\frac{\rho D}{\rho_d} \ln(1 + B_M) \cdot Nu_d \tag{5.36}$$

where Nu_d is the droplet Nusselt number, derived from the Ranz-Marshall correlation:

$$Nu_d = 2 + 0.6Re_d^{1/2}Pr^{1/3} \tag{5.37}$$

with Reynolds number:

$$Re_d = \frac{\rho|\mathbf{u} - \mathbf{u_d}|D}{\mu_g} \tag{5.38}$$

where $|\mathbf{u} - \mathbf{u_d}|$ is the relative velocity between the carrier fluid and the droplet, μ_g gas viscosity, and Prandtl number of the carrier fluid defined as:

$$Pr = \frac{c_{p,g}\mu_g}{k_g} \tag{5.39}$$

5.2.4 Momentum Source Term

To obtain the droplet velocity, equation 5.24 is solved, where the total force $\mathbf{F}$ is given by the sum of forces acting on the droplet. The drag force is the main force acting on droplets in a two-phase flow and can be expressed as:

$$\mathbf{F_d} = \frac{1}{2}C_d\rho A_d(\mathbf{u} - \mathbf{u_d})|\mathbf{u} - \mathbf{u_d}| \tag{5.40}$$

where C_d is the drag coefficient, A_d is the projected area of the droplet, ρ is the density of the carrier fluid, and $(\mathbf{u} - \mathbf{u_d})$ is the relative velocity between the carrier fluid and the droplet. The drag coefficient C_d can be calculated in the following ways:

- Schiller-Naumann:

$$C_d = \frac{24}{Re_d}(1 + 0.15Re_d^{0.687}) \quad \text{for } Re_d < 1000 \tag{5.41}$$

$$C_d = 0.424 \quad \text{for } Re_d \geq 1000 \tag{5.42}$$

- Putnam:

$$C_d = \frac{24}{Re_d}(1 + 0.1935Re_d^{0.6305}) \quad \text{for } Re_d < 1000 \tag{5.43}$$

$$C_d = 0.424 \quad \text{for } Re_d \geq 1000 \tag{5.44}$$

Where Re_d is the droplet Reynolds number defined previously. Other forces, such as gravity, can be included depending on the specific conditions of the problem. However, in many high-speed flow cases, the drag force is predominant. The droplet equation of motion becomes:

$$\frac{d\mathbf{u_d}}{dt} = \frac{f}{\tau_d}\mathbf{u_r} \tag{5.45}$$

with τ_d droplet response time defined as:

$$\tau_d = \frac{2\rho_d r_d^2}{9\mu_g} \tag{5.46}$$

and if the Schiller-Naumann correlation is chosen [34], the correction factor f is given

by:

$$f = 1 + 0.15Re_d^{0.687} \quad \text{for } Re_d < 1000 \tag{5.47}$$

$$f = 0.0183Re_d \quad \text{for } Re_d \geq 1000 \tag{5.48}$$

5.2.5 Energy Source Term

To calculate the energy source term S_e due to heat exchange between the droplet and the carrier fluid, the energy equation for the droplet is solved. The rate of change of droplet energy is given by:

$$m_d c_{p,l} \frac{dT_d}{dt} = \dot{m}_d h_v + A_d h(T - T_d) f' \tag{5.49}$$

where m_d is the droplet mass, $c_{p,l}$ is the specific heat at constant pressure of the liquid, $\dot{m}_d$ is the rate of change of droplet mass, h_v is the latent heat of vaporization, A_d is the droplet surface area, h is the convective heat transfer coefficient, T and T_d are respectively the temperature of the carrier fluid and the droplet, and f' is a correction factor to account for evaporation effects. The convective heat transfer coefficient h can be calculated using the Ranz-Marshall correlation:

$$h = \frac{Nu_d k_g}{D} \tag{5.50}$$

where Nu_d is the droplet Nusselt number defined by the Ranz-Marshall correlation (5.37), k_g is the thermal conductivity of the carrier fluid, and D is the droplet diameter.

Chapter 6

CFD Simulation and Heat Transfer Analysis

6.1 CFD Modeling Strategy

To validate the thermal models developed during the preliminary design phase, a set of higher–fidelity Computational Fluid Dynamics (CFD) simulations was performed using the open–source software *OpenFOAM*. The objective of these simulations is not only to reproduce the global flow field inside the injector but also to extract local flow quantities required for the evaluation of heat transfer on the pintle tip surfaces.

The CFD analysis allows the identification of the main flow structures that are typical of pintle injectors. In particular, the simulations highlight the presence of the Central Recirculation Zone (CRZ) downstream of the pintle tip, as well as the outer recirculation regions generated by the interaction between the radial and axial flows. These structures strongly influence the thermal loads acting on the injector components, especially on the pintle tip and on the injector faceplate.

Through the numerical simulations it is therefore possible to obtain detailed information regarding the local velocity field, temperature distribution, turbulence quantities, and wall shear stress. These quantities represent the fundamental input parameters required for the evaluation of the convective heat flux acting on the injector walls.

The CFD results are therefore used as a physically consistent dataset from which the heat flux can be evaluated and compared with simplified engineering models.

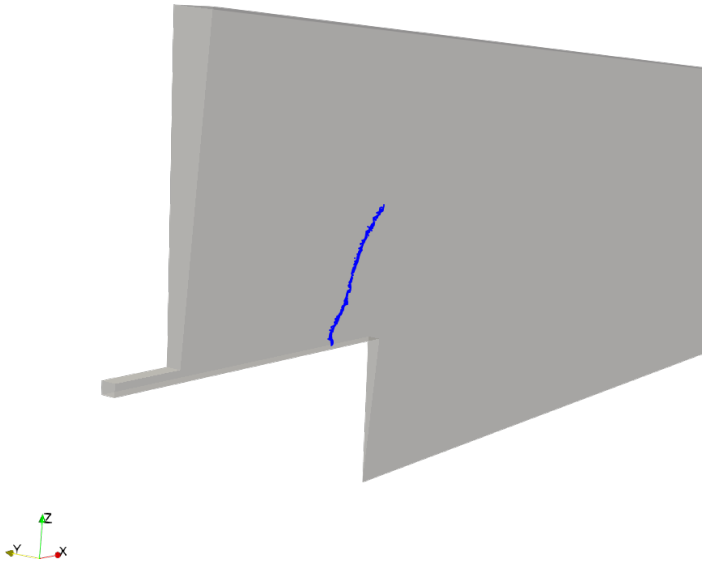

Figure 6.1: Computational fluid domain used in the CFD simulations

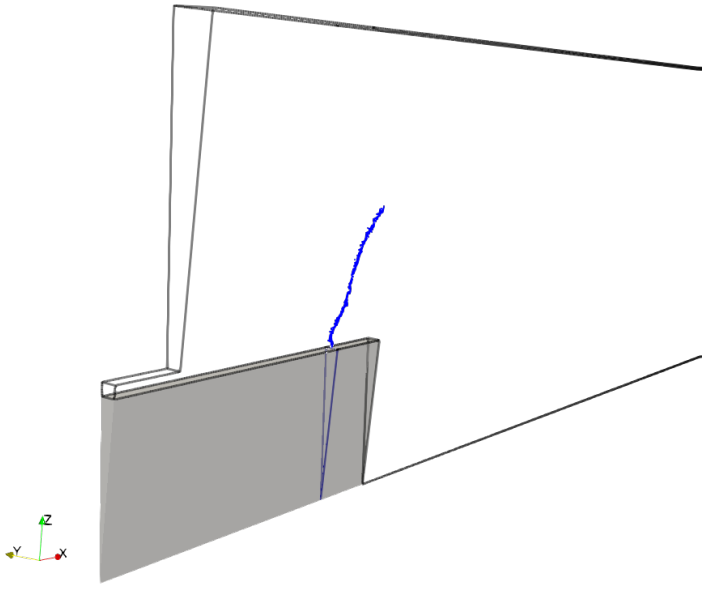

Figure 6.2: pintle body detail (in grey) and oxygen inlet (in blue)

6.2 Computational Domain and Geometry

The computational domain reproduces the internal region of the pintle injector, including the annular injection region, the pintle tip, and the near–field portion of the combustion chamber where the primary mixing between the propellants occurs.

Due to the geometrical symmetry of the injector, the computational domain can be simplified in order to reduce the overall computational cost while preserving the relevant flow physics.

The computational grid was generated using the OpenFOAM utility *blockMesh*, which produces a structured hexahedral mesh. Grid refinement near the walls and in the injection region was achieved through the use of grading, allowing a progressive variation of the cell size while preserving the structured topology of the mesh.

Special attention is devoted to the resolution of the near–wall region, since the accurate prediction of wall shear stress and thermal gradients is essential for the evaluation of heat transfer.

6.3 Boundary Conditions

The simulations employ boundary conditions consistent with the injector operating conditions obtained during the preliminary design phase.

At the injection passages, inlet boundary conditions are imposed in terms of velocity or mass flow rate depending on the specific configuration considered. These conditions reproduce the propellant injection conditions determined during the injector sizing procedure.

At the downstream boundary of the computational domain, a pressure outlet condition is applied to represent the combustion chamber environment.

All walls of the injector are modeled using no–slip boundary conditions. Standard wall functions are employed to model the near-wall region, allowing the boundary layer to be resolved without the need for excessive mesh refinement close to the wall.

6.4 Mesh Sensitivity Study

A mesh sensitivity study was conducted to assess the influence of grid resolution on the numerical results.

Three structured meshes were generated using the *blockMesh* utility: a coarse mesh, an intermediate mesh, and a fine mesh, containing respectively 7630, 30002, and 122080 cells.

All meshes exhibit similar quality metrics, including maximum skewness values around 0.33 and negligible non–orthogonality, ensuring the numerical stability of the simulations.

To evaluate mesh convergence, several probes were placed along the injector axis and the mean temperature was monitored at different locations. The results indicate that the coarse mesh underpredicts the combustion temperature, while the intermediate and fine meshes provide very similar results.

Based on this analysis, the intermediate mesh was selected for the subsequent simulations, since it ensures adequate resolution of the flow and thermal fields while keeping the computational cost at an acceptable level.

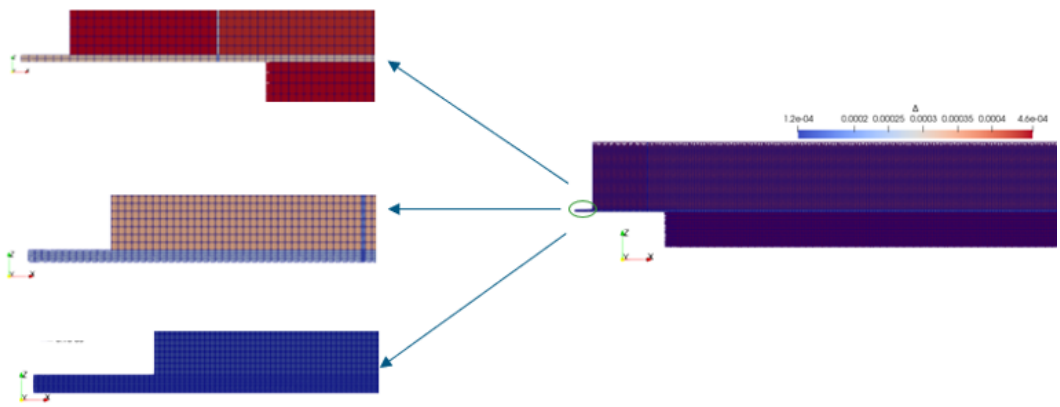

Figure 6.3: mesh detail comparison: coarse (top), intermediate (center), and fine (bottom)

6.5 Flow Field Analysis

The computed flow fields provide insight into the mixing and combustion processes occurring within the injector.

The methane mass fraction distribution, shown in Figure 6.4, highlights the injection of the fuel stream and its rapid mixing with the oxidizer flow. The oxygen mass fraction field, shown in Figure 6.5, confirms the strong interaction between the two streams. The distribution of the OH radical, shown in Figure 6.6, clearly identifies the main reaction zone and the development of the flame downstream of the injection region. The temperature field, shown in Figure 6.7, shows the rapid increase in temperature associated with the combustion process, with peak values located in the mixing region immediately downstream of the injector. Streamline visualization, shown in Figure 6.8, further reveals the presence of recirculation structures near the pintle tip, which contribute to flame stabilization and enhanced mixing between the propellants. The pressure field, shown in Figure 6.9, appears largely uniform throughout the computational domain. Significant variations are observed only in the impingement region between the gaseous methane jet and the liquid oxygen jet, where a localized overpressure develops at the impact point due to the deceleration of the flow. This region is followed by a pressure drop immediately downstream of the jet, associated with flow acceleration and jet deflection.

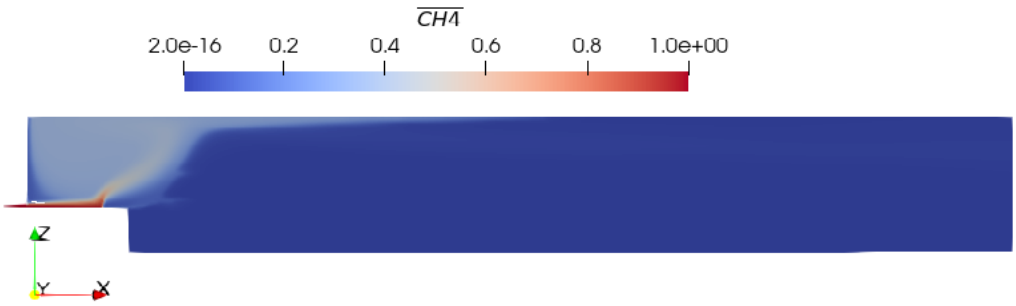

Figure 6.4: $\overline{CH_4}$ mass fraction distribution

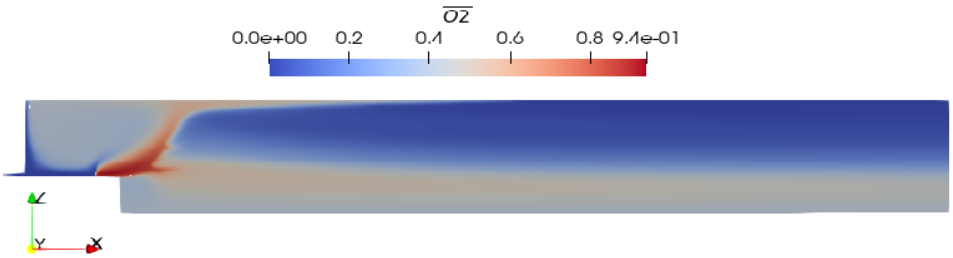

Figure 6.5: $\overline{O_2}$ mass fraction distribution

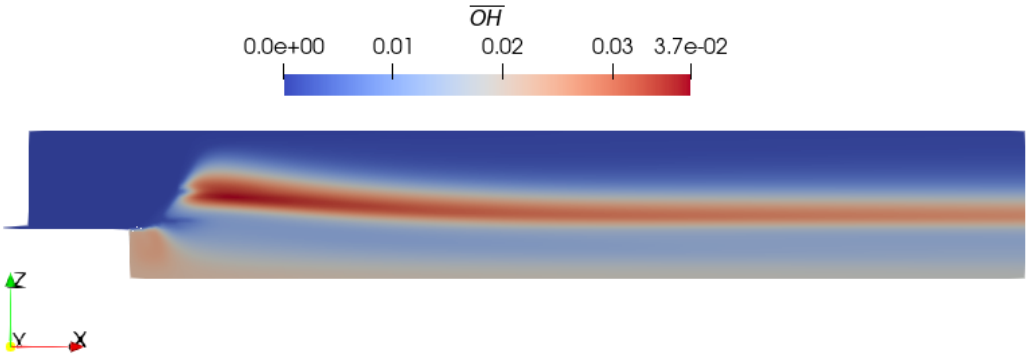

Figure 6.6: $\overline{OH}$ mass fraction distribution

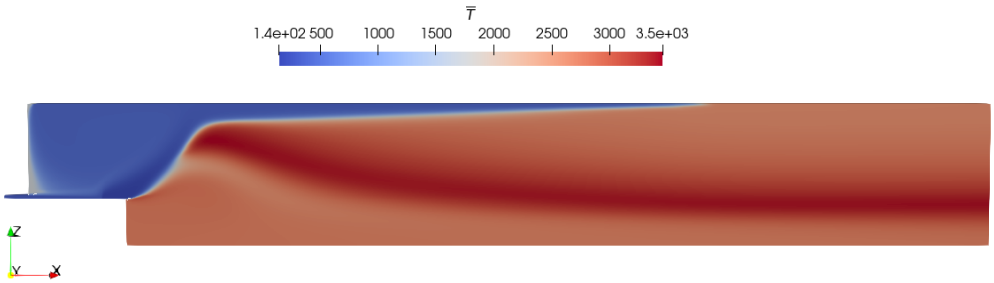

Figure 6.7: $\overline{T}$ distribution

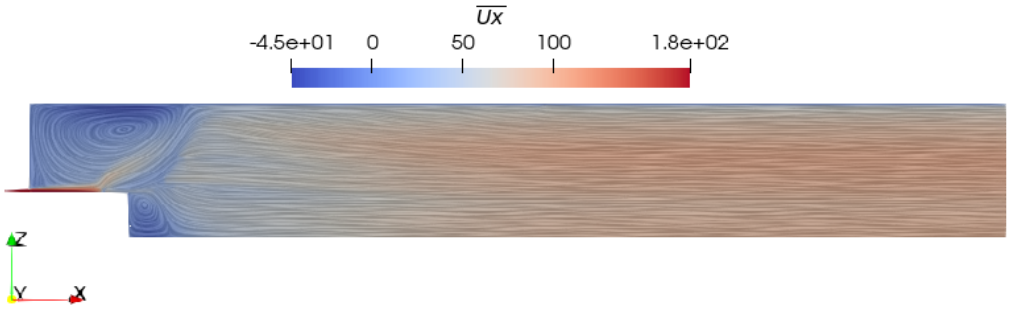

Figure 6.8: Streamlines colored by axial velocity $\overline{U_x}$

Figure 6.9: $\overline{p}$ distribution

6.5.1 Design variables comparison

Spray-related quantities were compared between the 0D model predictions and the CFD results. In particular, the analysis focused on the Sauter Mean Diameter (SMD), the vaporization length, and the spray angle.

The spray angle was evaluated by measuring the opening angle of the spray plume downstream of the injector exit. This quantity is mainly governed by the injector geometry and by the injection conditions, which are consistently defined in both the CFD simulation and the 0D formulation.

In particular, the spray angle from the CFD simulation was evaluated through a post–processing procedure implemented in Python. The Lagrangian parcels obtained from the simulation were analyzed in order to identify the spray envelope. The outer boundary of the spray was reconstructed and a linear fit was applied to determine the average slope of the envelope. From this slope, the corresponding spray half-angle was calculated.

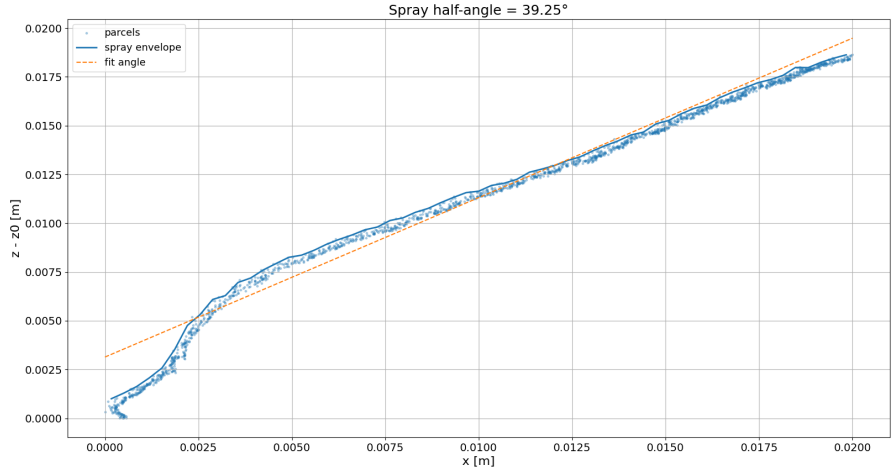

Figure 6.10: Spray envelope extracted from CFD parcels and linear fitting used to estimate the spray half-angle.

The resulting spray half-angle obtained from the CFD analysis is

$$\theta_{CFD} = 39.25^{\circ} \tag{6.1}$$

which is in very good agreement with the theoretical prediction obtained from the Cheng [9] correlation

$$\theta_{Cheng} = 39.24^{\circ} \tag{6.2}$$

For the SMD and the vaporization length, larger discrepancies are found. These quantities are strongly influenced by the detailed interaction between droplets and the surrounding flow field, which is fully resolved in the CFD simulations but only approximated in the simplified 0D formulation.

A summary of the comparison between the two approaches is reported in Table 6.1.

Table 6.1: Comparison between CFD results and 0D model predictions for key spray parameters

	SMD [μm]	Vaporization Length [mm]	Spray Angle [°]
CFD	16.97	2.45	39.25
0D Model	6.15	0.92	39.24
Error	63.75%	62.45%	$\approx 0\%$

The differences observed in SMD and vaporization length can be mainly attributed to the simplified physical assumptions adopted in the 0D model. In particular, the simplified formulation does not account for several effects that are naturally captured in the CFD simulations, such as the presence of a skip distance, variations in the relative velocity between the droplets and the surrounding gas, and the complex interaction between turbulence and droplet evaporation.

These effects significantly influence the droplet breakup and evaporation processes, leading to larger droplets and longer vaporization lengths in the CFD simulations. Since the 0D model relies on simplified correlations and averaged flow properties, it is not able to fully reproduce these local flow phenomena, resulting in the discrepancies observed in Table 6.1.

Nevertheless, the excellent agreement obtained for the spray angle confirms that the geometric and injection parameters are correctly captured by the simplified model.

6.6 Heat Flux Evaluation

6.6.1 Extraction of Wall Quantities

The CFD results provide several quantities required for the evaluation of convective heat transfer at the wall.

- Wall temperature T_w
- Local gas temperature T_g
- Dimensionless wall distance y^+
- Gas density at the wall ρ_w
- Local gas density ρ_g
- Gas specific heat at the wall $c_{p,w}$
- Local gas specific heat c_p, g
- Turbulent kinetic energy k

These quantities are extracted from the CFD solution and used to evaluate the wall heat flux through the turbulent wall heat transfer model described in the following section.

6.6.2 Heat Flux Model Based on Turbulent Wall Laws (Han & Reitz)

The wall heat flux was evaluated using the Han and Reitz turbulent wall heat transfer formulation [36] which relates the heat flux to the turbulent momentum transport in the near–wall region.

The heat flux is expressed as

$$q_w = \frac{u_\tau \, C \, \ln\left(\frac{T_g}{T_w}\right)}{A \ln(y^+) + 2.5} \tag{6.3}$$

where the friction velocity is defined as

$$u_\tau = \sqrt{\frac{\rho_g}{\rho_w}}\, C_\mu^{1/4} \sqrt{k} \tag{6.4}$$

and the energy term is

$$C = \frac{1}{2}\left(\rho_g c_{p,g} T_g + \rho_w c_{p,w} T_w\right) \tag{6.5}$$

6.6.3 Analysis of the Heat Flux Distribution Predicted by the Han-Reitz Model

The wall heat flux distribution predicted using the Han and Reitz formulation, Figure 6.11 shows a non–uniform behavior along the pintle radius. Two regions can be identified where the predicted heat flux exhibits noticeable variations that require further interpretation.

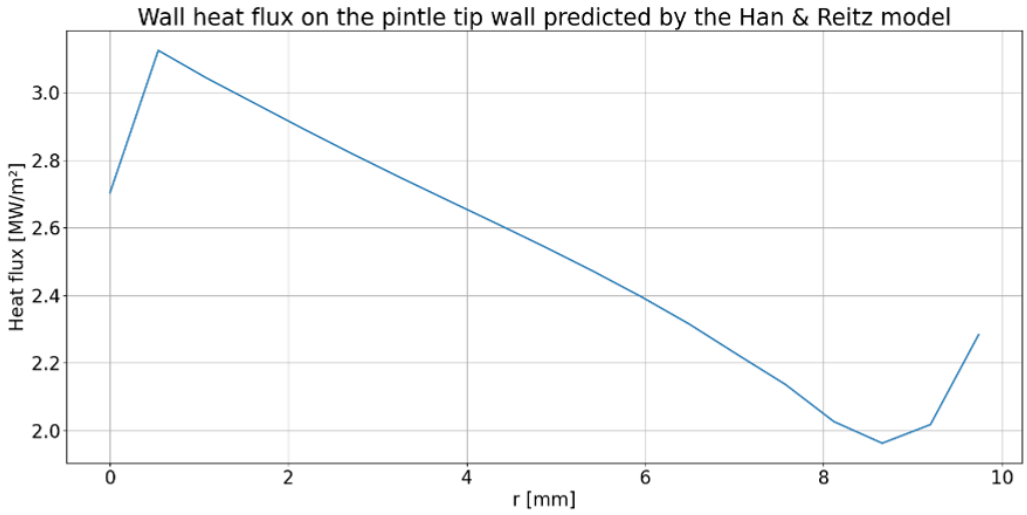

Figure 6.11: Heat flux predicted by Han-Reitz model

The first region is located near the upstream edge of the pintle tip. In this area the wall heat flux is influenced by the upstream axial flow approaching the step between the injector body and the pintle tip. The flow acceleration in this region modifies the local thermal boundary layer and leads to an increase in the convective heat transfer predicted by the wall function model.

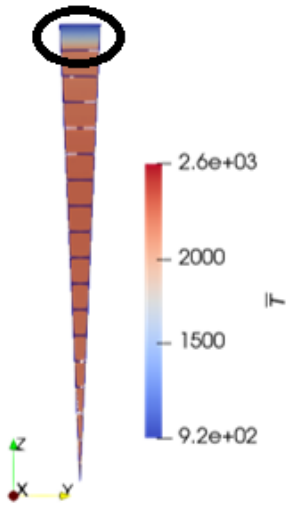

Figure 6.12: temperature field near step

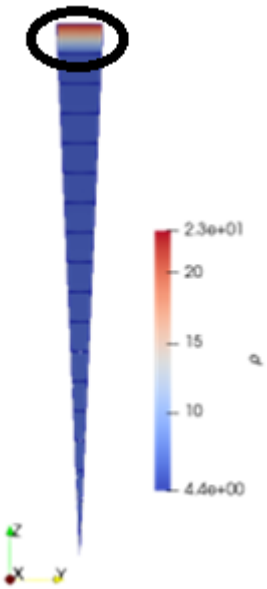

Figure 6.13: density field near step

A second characteristic feature of the heat flux distribution is the sharp variation observed between the wall location and the first computational cell in the near–wall region. This apparent discontinuity is not primarily driven by temperature variations, but rather by changes in the local gas density.

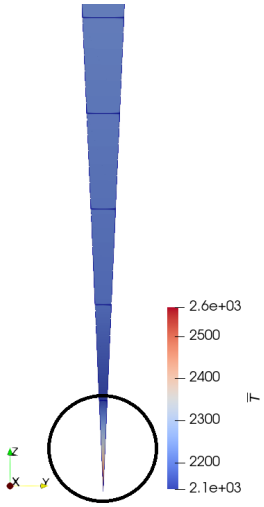

Figure 6.14: temperature field near the chamber symmetry axis

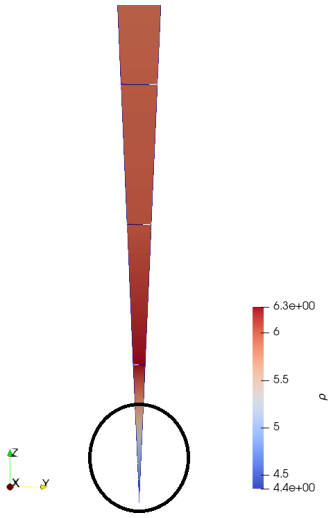

Figure 6.15: density field near the chamber symmetry axis

In the Han and Reitz formulation, the heat flux depends on the friction velocity

$$u_\tau \sim \sqrt{\rho_g} \tag{6.6}$$

which is directly influenced by the local gas density. The density also contributes to the energy term appearing in the model numerator

$$C \sim \rho_g c_p T_g. \tag{6.7}$$

An analysis of the CFD fields shows that between the wall and the first computational cell the gas temperature slightly decreases, while the gas density increases significantly. As a consequence, the density effect dominates the model formulation, leading to an increase in the numerator of the heat flux expression and therefore

producing the local peak observed in the heat flux profile.

This behavior explains the "kink" observed in the heat flux distribution near the wall and highlights the strong sensitivity of the Han and Reitz formulation to density variations in the near–wall region.

Despite these local features, the overall heat flux distribution remains physically consistent with the flow structure predicted by the CFD simulations and provides a reliable reference dataset for the calibration of simplified heat transfer correlations.

For the subsequent analysis and model calibration, the regions close to the geometric boundaries of the pintle tip were excluded from the evaluation of the heat flux distribution.

6.6.4 Jet Impingement Heat Transfer Model (Katti–Prabhu)

The heat flux predicted by the Han and Reitz formulation was then compared with the results obtained using the Katti and Prabhu correlation.

This correlation models the heat transfer as an impinging jet configuration and expresses the Nusselt number as a function of Reynolds number, Prandtl number, and geometric parameters.

$$Nu = f(Re, Pr, z/D) \tag{6.8}$$

The heat transfer coefficient is obtained as

$$h = \frac{Nu\lambda}{d} \tag{6.9}$$

and the heat flux is then

$$\dot{q} = h(T_g - T_w) \tag{6.10}$$

Unlike the Han and Reitz formulation, this approach relies only on global flow quantities and can therefore be applied within a 0D framework.

6.6.5 Heat Flux Model Comparison

The heat flux predicted by the Han and Reitz formulation was used as a reference dataset for the validation of the simplified Katti–Prabhu model.

An initial comparison between the two models, for a fixed pintle tip temperature of 800K, revealed noticeable discrepancies along the pintle radius. The simplified model tends to overpredict the heat flux in the upstream region while underpredicting it toward the outer radius. The local error distribution between the two models before calibration is reported in Figure 6.17.

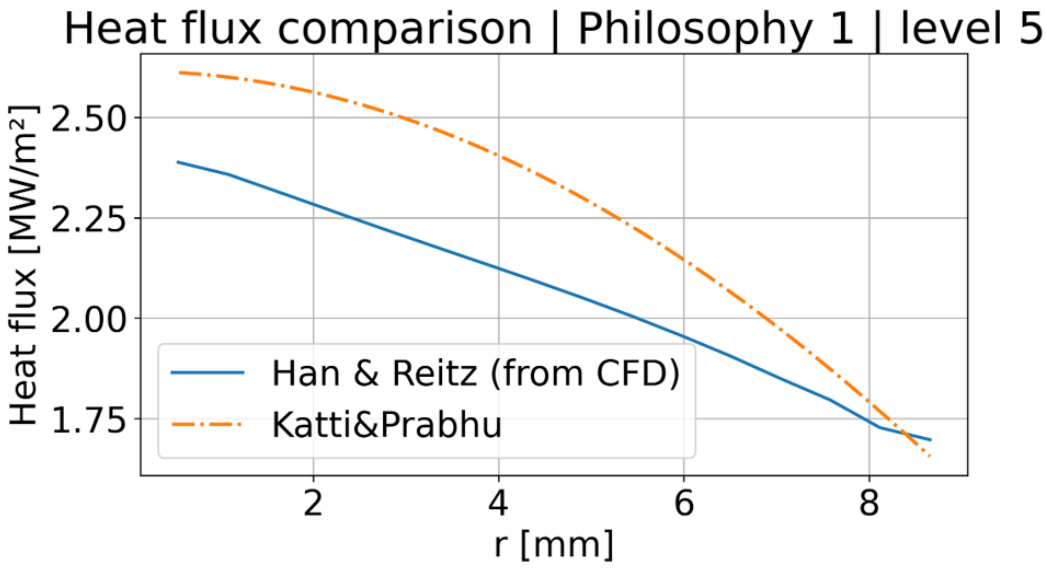

Figure 6.16: Heat flux comparison between the Han–Reitz formulation and the Katti–Prabhu model before parameter fitting

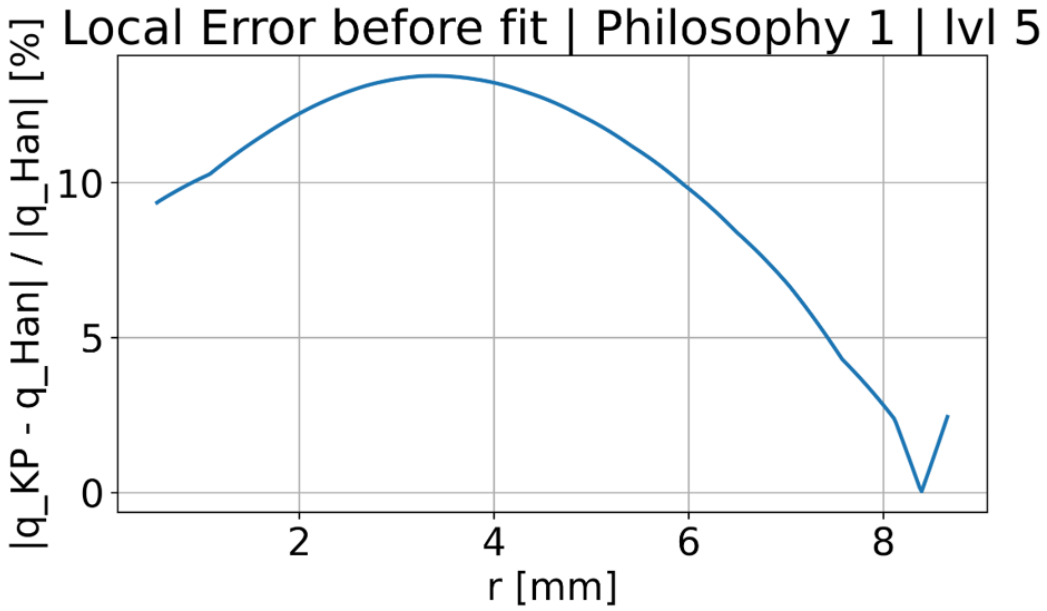

Figure 6.17: Local error distribution between the Katti-Prabhu model and the CFD-based Han-Reitz heat flux before parameter fitting

The ordinate represents the local relative error between the simplified model and the CFD-based heat flux, computed as

$$\epsilon(\%) = \frac{|q_{model} - q_{CFD}|}{q_{CFD}} \times 100 \tag{6.11}$$

To improve the agreement between the two models, a fitting procedure was introduced in which the parameters of the Katti–Prabhu correlation were calibrated using the CFD-based heat flux data.

The resulting comparison between the calibrated Katti–Prabhu model and the

CFD-derived heat flux is shown in Figure 6.18. The corresponding local error distribution after fitting is reported in Figure 6.19.

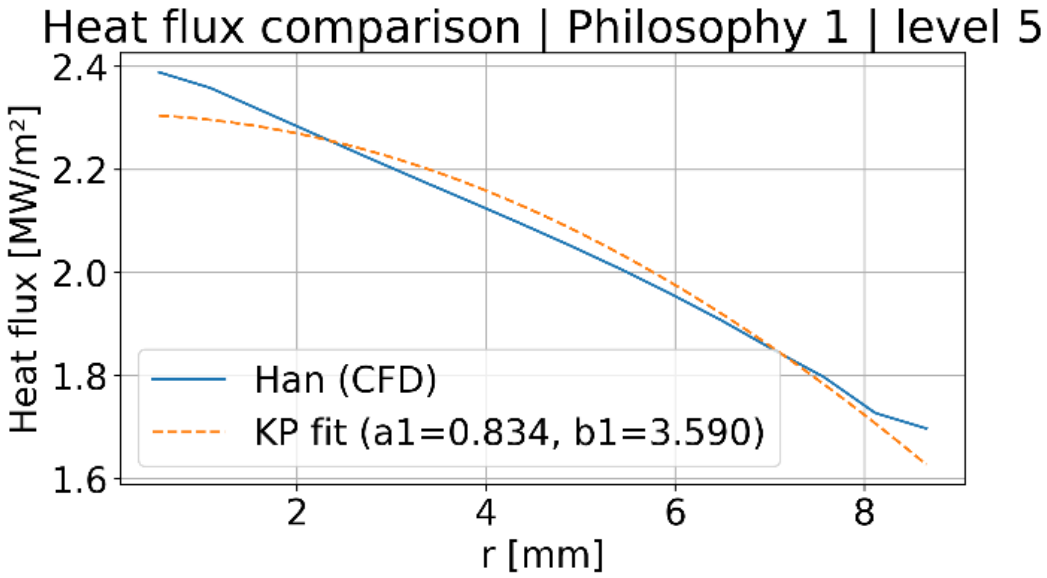

Figure 6.18: Heat flux comparison after calibration of the Katti-Prabhu model parameters

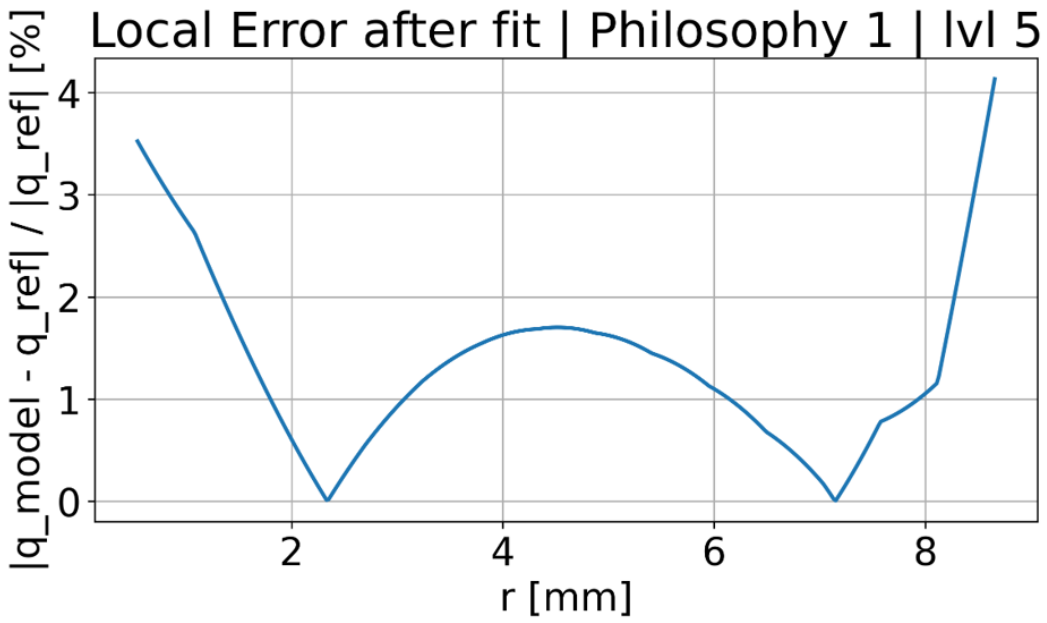

Figure 6.19: Local error distribution after parameter fitting

Before calibration, the simplified Katti-Prabhu model exhibits noticeable deviations from the CFD-based Han-Reitz heat flux, particularly in the central region of the pintle tip. After the parameter fitting, the agreement between the two models significantly improves. The local error is substantially reduced across most of the radial coordinate, confirming that the calibrated correlation is able to accurately reproduce the CFD-derived heat flux distribution.

6.6.6 Parameter Fitting and Model Validation

Additional simulations were conducted for three different wall temperatures (500 K, 800 K and 1100 K). For each case, the parameters of the Katti–Prabhu model were fitted to reproduce the Han and Reitz heat flux obtained from the CFD data.

The fitted parameters show an approximately linear dependence on the wall temperature. A linear interpolation of the model coefficients was therefore derived to predict intermediate conditions.

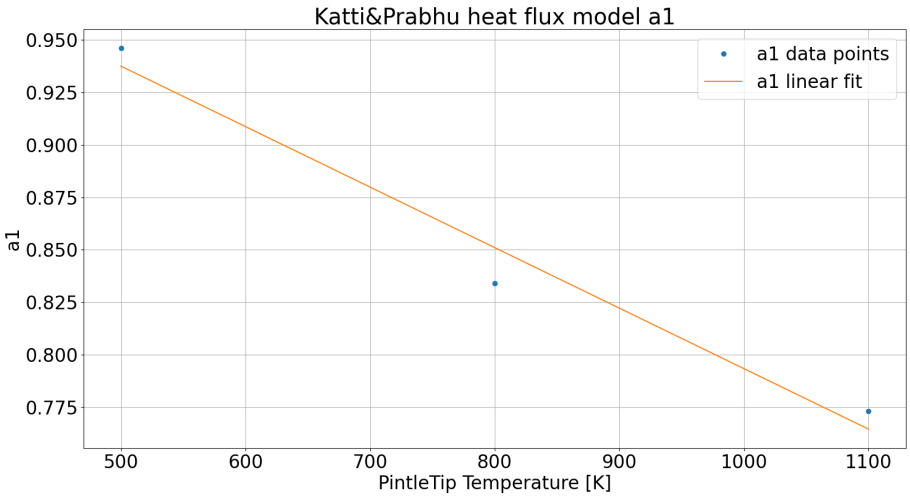

Figure 6.20: a1 coefficient of Katti and Prabhu model linear fitting

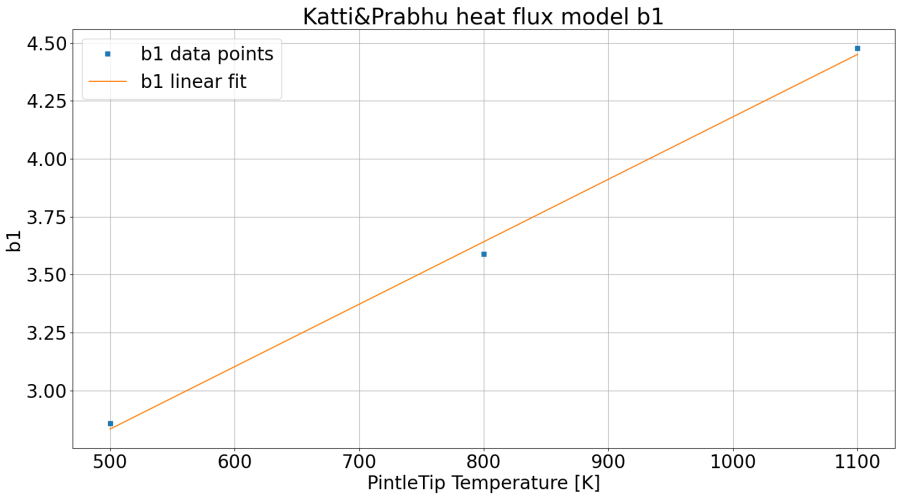

Figure 6.21: b1 coefficient of Katti and Prabhu model linear fitting

To validate this approach, a fourth case at $T_w = 950\,K$ was considered. The interpolated parameters were used in the Katti–Prabhu correlation and the resulting heat flux was compared with the CFD-based Han and Reitz prediction.

The comparison shows excellent agreement between the two approaches, with a maximum error of approximately 5%. This demonstrates that the calibrated correla-

tion provides an accurate yet computationally inexpensive method for estimating the thermal loads acting on the pintle tip.

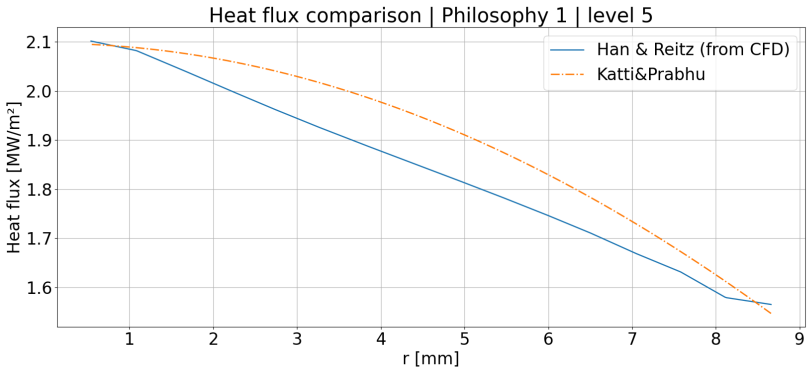

Figure 6.22: heat flux comparison on pintleTip with an isothermal temperature on pintle tip of 950K

6.6.7 Influence of Mesh Resolution on Heat Flux Fitting

In order to assess the influence of the mesh resolution on the calibration of the simplified heat transfer model, the fitting procedure described in the previous section was repeated using the heat flux distribution obtained from the refined CFD mesh.

As discussed in the mesh sensitivity study, grid refinement improves the resolution of the near–wall region and allows a more accurate prediction of the turbulent quantities governing wall heat transfer. Since the Han–Reitz formulation directly depends on these near–wall quantities, the heat flux extracted from the refined mesh provides a more reliable reference dataset for the calibration of the Katti–Prabhu correlation.

The comparison between the CFD-based heat flux and the fitted Katti–Prabhu model obtained using the refined mesh is shown in Figure 6.23.

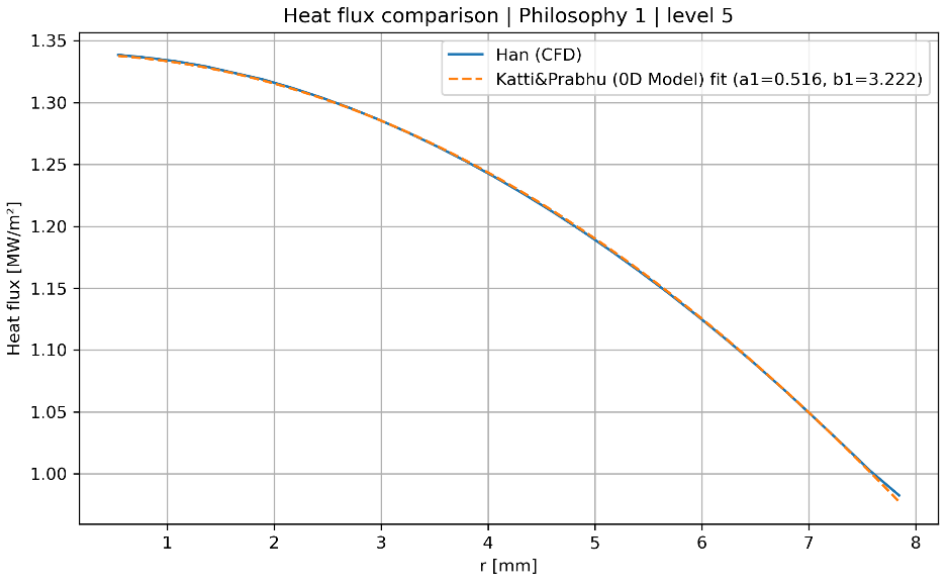

Figure 6.23: heat flux comparison on pintleTip with finer mesh

The agreement between the two curves is improved compared to the previous case, particularly in the central region of the pintle tip.

The corresponding local error distribution is reported in Figure 6.24.

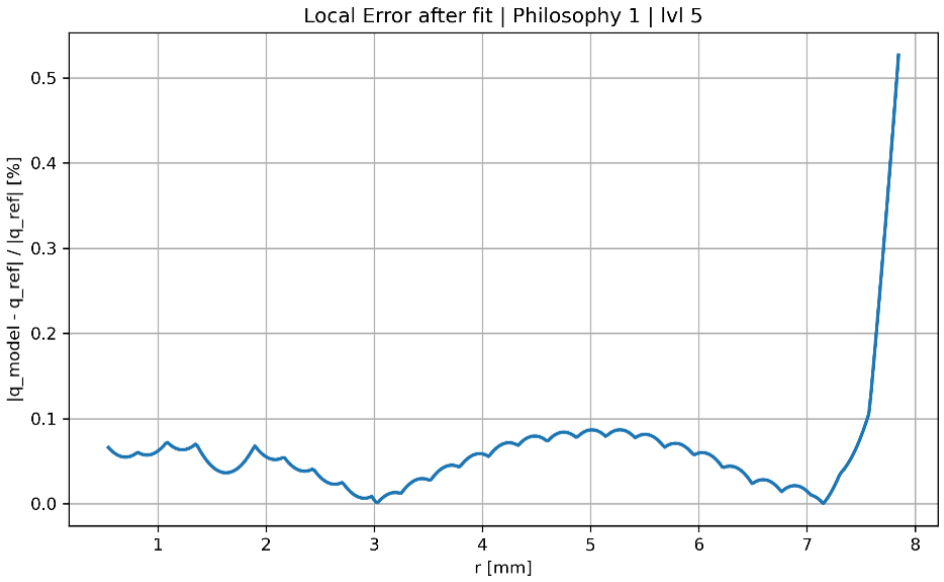

Figure 6.24: error percentage between the two model after fitting with finer mesh

The error remains below approximately 0.5% along most of the radial coordinate, with larger deviations observed only near the outer edge of the domain. These discrepancies are mainly associated with local flow acceleration and edge effects that are difficult to capture with simplified correlations.

Overall, the results confirm that mesh refinement leads to a more accurate CFD prediction of the wall heat flux, which in turn improves the calibration of the simplified heat transfer model. This observation further supports the use of the refined CFD

solution as a reference dataset for the development of the reduced-order thermal model.

6.6.8 Discussion and Key Findings

The CFD simulations provided detailed insight into the flow and thermal processes occurring inside the pintle injector. The numerical results highlighted the presence of characteristic flow structures such as the central recirculation zone downstream of the pintle tip, which contributes to flame stabilization and enhances the mixing between methane and oxygen streams.

The analysis of the species and temperature fields confirmed the rapid mixing of the propellants and the development of the main reaction zone immediately downstream of the injection region. The distribution of OH radicals clearly identified the flame region, while the temperature field revealed the locations of peak thermal loads.

A comparison between the CFD results and the simplified 0D spray model showed excellent agreement in terms of spray angle, confirming that the injector geometry and injection conditions were correctly captured by the reduced-order formulation. Larger discrepancies were observed for the Sauter Mean Diameter and vaporization length, which are strongly influenced by detailed droplet–flow interactions that are only partially represented in the simplified model.

The CFD solution was also used to extract the quantities required for the evaluation of the wall heat flux using the Han–Reitz wall heat transfer formulation. These results were employed as a reference dataset for the calibration of the simplified Katti–Prabhu heat transfer correlation.

The calibration procedure significantly improved the agreement between the simplified model and the CFD-derived heat flux distribution. After parameter fitting, the local error was substantially reduced across most of the pintle radius, demonstrating that the calibrated correlation is capable of accurately reproducing the heat flux predicted by the CFD simulations.

Finally, the influence of mesh resolution on the heat flux calibration was investigated. The results showed that grid refinement improves the accuracy of the CFD-derived wall heat flux and consequently leads to a more reliable calibration of the reduced-order thermal model.

The main advantage of this approach lies in the possibility of replacing computationally expensive CFD simulations with a simplified correlation that retains the essential physical behavior of the system. Once calibrated using CFD data, the reduced-order model can be used to rapidly estimate the thermal loads acting on the injector components during preliminary design iterations.

Overall, the CFD simulations provided a physically consistent dataset that enabled the development and validation of a simplified heat transfer model suitable for preliminary injector design analyses while significantly reducing the computational cost associated with high-fidelity simulations. This workflow enables the use of higher-

fidelity CFD simulations as a calibration tool for the development of computationally efficient thermal models suitable for rapid injector design iterations.

Chapter 7

Conclusions

This thesis investigates the design and thermal analysis of a pintle-type injector for liquid rocket propulsion, combining simplified engineering models with higher-fidelity computational fluid dynamics (CFD) simulations.

The work was developed within a progressive methodological framework aimed at bridging the gap between preliminary design tools and detailed numerical simulations. In the initial phase, the fundamental principles of liquid rocket propulsion were reviewed in order to derive a simplified analytical model suitable for injector sizing. Based on these theoretical foundations, a numerical methodology was developed for the preliminary design and optimization of the pintle injector geometry. The resulting 0D model allowed the identification of key design parameters such as spray angle, droplet size, and vaporization distance.

The limits of simplified approaches were then addressed through the introduction of a computational fluid dynamics framework capable of resolving the complex physical phenomena occurring within the injector. The Eulerian–Lagrangian formulation was adopted to describe the interaction between the gaseous phase and the dispersed droplet phase, allowing the simulation of spray atomization, evaporation, and mixing processes.

Higher-fidelity CFD simulations were performed using the open-source solver OpenFOAM in order to characterize the internal flow field of the injector and to analyze the resulting combustion and thermal behavior. The numerical results highlighted the presence of characteristic flow structures typical of pintle injectors, including the formation of a central recirculation zone downstream of the pintle tip. This flow structure plays a key role in flame stabilization and enhances the mixing between methane and oxygen streams.

The CFD analysis also enabled a detailed comparison between the numerical results and the predictions obtained from the simplified spray model. While an excellent agreement was observed in terms of spray angle, larger discrepancies were identified for the Sauter Mean Diameter and the vaporization length. These differences are mainly attributed to the simplified physical assumptions adopted in the 0D formulation, which cannot fully capture the complex interaction between turbulence, droplet breakup, and evaporation processes.

A major contribution of this work concerns the evaluation of the thermal loads acting on the injector components. The CFD simulations were used to extract the quantities required to compute the wall heat flux using the Han–Reitz turbulent wall heat transfer formulation. The resulting heat flux distribution served as a reference dataset for the calibration of a simplified heat transfer model based on the Katti–Prabhu correlation.

Through a dedicated parameter fitting procedure, the simplified model was calibrated to reproduce the CFD-derived heat flux distribution along the pintle radius. The calibration significantly improved the agreement between the two models, reducing the local prediction error and demonstrating that the simplified correlation can accurately reproduce the thermal behavior predicted by the CFD simulations.

The influence of mesh resolution on the calibration process was also investigated. The results showed that grid refinement improves the accuracy of the CFD-derived wall heat flux and consequently leads to a more reliable calibration of the reduced-order thermal model.

The final outcome of this work is therefore the development of a computationally efficient heat transfer model that retains the essential physical behavior captured by higher-fidelity simulations. Once calibrated using CFD data, this reduced-order formulation can be used to rapidly estimate the thermal loads acting on the injector components during preliminary design iterations.

Overall, the proposed methodology demonstrates how higher-fidelity CFD simulations can be effectively used as a calibration tool for the development of simplified engineering models. This approach enables the integration of detailed physical insight into preliminary design methodologies, significantly reducing the computational cost associated with repeated numerical simulations while maintaining an adequate level of predictive accuracy.

Appendix A

Appendix A

A.1 Summary of Pintle Engine Characteristics

A comparative table summarizing the technical specifications and applications of the main pintle-type injector engines analyzed is presented below.

Table A.1: Detailed comparison of engines based on Pintle Injector technology.

Name	**Period**	**Chamber Pressure [bar]**	**Cycle**	**Vac Thrust [kN]**	**MR**	**Propellants**	**C* [m/s]**	**Isp [s]**	**Throttling**
LMDE	1967-1975	6.89	Blowdown	44	1.6	Aerozine 50 / N_2O_4	1906	311	12%–100%
SpaceX Merlin 1D	2013	97	Gas-Generator	914	2.34	LOX / RP-1	1580	311	40%–100%
SpaceX Kestrel [37]	2004-2009	9.3	Blowdown	31	2.56	LOX / RP-1	1546	317	N/A
TRW TR-106 (LCPE)	2000	–	Gas-Gen. / Ablative	2892 (Sea Level)	6.0	LOX / LH_2	–	–	65%–100%
Chang'e 3 (7500N)	2013	∼12	Pressure-Fed	7.5	1.65	MMH / MON-1	1640	308	15%–110%

Appendix B

Appendix B

B.1 Finite Volume Method

The OpenFOAM software uses the Finite Volume Method (FVM) to solve the partial differential equations (PDEs) governing the simulated physical phenomena. The Finite Volume Method (FVM) is a numerical technique used to solve partial differential equations (PDEs) describing physical phenomena such as fluid flow, heat transfer, and chemical species diffusion. The FVM is based on the subdivision of the computational domain into a set of discrete control volumes, within which the conservation principles of physical quantities are applied.

In this method, the conservation equations are integrated over each control volume, transforming the PDEs into algebraic equations that can be solved numerically. Physical quantities, such as mass, momentum, and energy, are calculated as averages within each control volume, and fluxes through the control volume surfaces are used to update these quantities over time.

The FVM is particularly appreciated for its ability to strictly conserve physical quantities, making it suitable for simulations of complex flows and non-linear phenomena. Furthermore, the FVM is flexible and can be applied to complex geometries and unstructured grids, making it a popular choice in many fields of engineering and computational science. The generic conservation equation for a scalar quantity ϕ in integral form is given by:

$$\frac{\partial}{\partial t}\int_V \rho\phi \, dV + \int_V \nabla(\rho\phi\mathbf{u}) \cdot d\mathbf{V} = \int_V \nabla(\rho\Gamma\nabla\phi) \cdot d\mathbf{V} + \int_V S_\phi \, dV \tag{B.1}$$

with V representing the control volume, ρ the fluid density, $\mathbf{u}$ the velocity vector, Γ the diffusivity coefficient, and S_ϕ the source term associated with the scalar quantity ϕ.

The convective term $\nabla(\rho\phi\mathbf{u})$ represents the transport of the scalar quantity ϕ due to fluid motion, while the diffusive term $\nabla(\rho\Gamma\nabla\phi)$ describes the transport of ϕ due to molecular diffusion. The source term S_ϕ can include contributions from chemical reactions, heat sources, or other problem-specific sources.

Property values are calculated at the centers of the control volumes, while fluxes

through control volume surfaces are evaluated using property values at the volume boundaries. This approach ensures the conservation of physical quantities within each control volume, making FVM a robust and reliable technique for the numerical simulation of complex physical phenomena. At this point, a specific transport equation can be defined for each physical quantity of interest, such as mass, momentum, and energy.

$$\underline{\underline{A}} \cdot \underline{\Phi} = \underline{b} \tag{B.2}$$

where A is the coefficient matrix, Φ is the vector of unknowns, and b is the vector of known terms. Each row of matrix A represents the balance equation for a specific control volume, while the elements of vector Φ correspond to the values of physical properties (such as velocity, pressure, temperature, etc.) at the centers of the control volumes. Vector b contains the contributions of sources and known terms associated with each control volume. Solving this system of algebraic equations allows obtaining a numerical estimate of the physical properties within the computational domain, thus allowing for the analysis and prediction of the behavior of the physical system under examination. This system is solved iteratively, updating property values until the desired convergence is reached. This iterative method produces a numerical error that depends on the spatial and temporal discretization adopted, as well as the specific characteristics of the simulated problem. The accuracy of the numerical solution can be improved by reducing the size of the control volumes (increasing grid resolution) and adopting more sophisticated numerical schemes for the discretization of transport equations. The residual R can be defined as the difference between the left side and the right side of the balance equation for each control volume:

$$\underline{R} = \left| \underline{\underline{A}} \cdot \underline{\Phi} - \underline{b} \right| \tag{B.3}$$

The residual represents the numerical error associated with the current solution of the equation system. During the iterative solution process, the goal is to reduce the residual to a sufficiently low value, indicating that the numerical solution is approaching the exact solution of the balance equations. Convergence is generally reached when the residual falls below a predefined threshold (e.g., 10^{-6} or 10^{-8}), depending on the specific needs of the simulated problem [35].

B.1.1 Solution Algorithms

OpenFOAM offers several algorithms to solve the system of Navier-Stokes equations, including:

- **SIMPLE (Semi-Implicit Method for Pressure-Linked Equations):** An iterative method that solves the momentum and continuity equations sequentially, updating pressure and velocity in each iteration. Figure B.1 shows the flowchart of the SIMPLE algorithm.
- **PISO (Pressure-Implicit with Splitting of Operators):** An explicit method that solves the momentum and continuity equations iteratively, using

multiple pressure corrections to improve convergence. Figure B.2 shows the flowchart of the PISO algorithm.

- **SIMPLEC (SIMPLE-Consistent):** A variant of the SIMPLE method that improves convergence using a more consistent formulation of the balance equations.
- **PIMPLE (PISO-SIMPLE Hybrid Method):** A hybrid method that combines the SIMPLE and PISO approaches, allowing for efficient management of both transient and steady flows. Figure B.3 shows the flowchart of the PIMPLE algorithm.

The choice of algorithm depends on the specific characteristics of the simulated problem, such as the nature of the flow (steady or transient), geometry complexity, and requirements for accuracy and calculation speed.

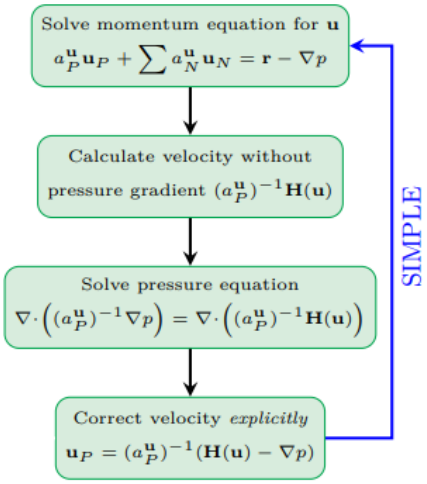

Figure B.1: SIMPLE Algorithm Flowchart [38]

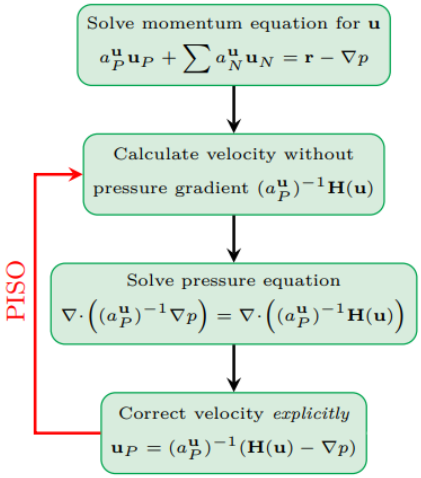

Figure B.2: PISO Algorithm Flowchart [38]

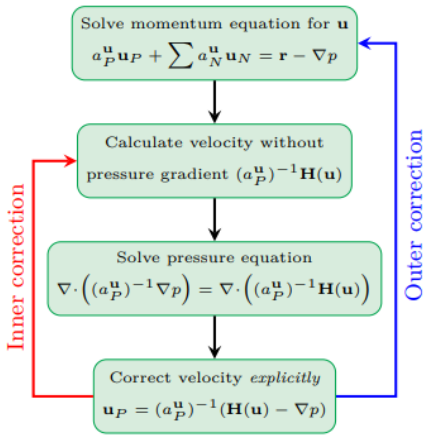

Figure B.3: PIMPLE Algorithm Flowchart [38]

Bibliography

[1] San Diego State University Aerospace. *Pintle Injector Poster*. 2025. URL: https://aerospace.sdsu.edu/design-day/files/2025/pintle_injector_poster.pdf (visited on 12/01/2025) (cit. on p. 1).

[2] MIT Rocket Team. *Topic 6: Injector Design*. URL: https://wikis.mit.edu/confluence/display/RocketTeam/Topic+6%3A+Injector+Design (visited on 03/23/2026) (cit. on p. 5).

[3] Aerospace Notes. *Injectors - Liquid Propellant Rockets*. URL: https://aerospacenotes.com/injectors-liquid-propellant-rockets/ (visited on 03/23/2026) (cit. on p. 5).

[4] Gordon A. Dressler and J. Martin Bauer. "TRW pintle engine heritage and performance characteristics". In: *36th AIAA/ASME/SAE/ASEE Joint Propulsion Conference and Exhibit*. AIAA 2000-3871. AIAA. 2000, p. 3871 (cit. on pp. 6, 11, 13).

[5] W. Bartlett, Z. D. Kirkland, R. W. Polifka, J. C. Smithson, and G. L. Spencer. *Apollo spacecraft liquid primary propulsion systems*. Tech. rep. NASA-TM-X-65048. Accession Number: 70N35721. NASA Manned Spacecraft Center, Feb. 1966. URL: https://ntrs.nasa.gov/citations/19700026405 (cit. on pp. 7, 13).

[6] Encyclopedia Astronautica. *TR-106 Low Cost Pintle Engine (LCPE)*. https://www.astronautix.com/t/tr-106.html. Accessed: 2026-01-03. 2000 (cit. on p. 7).

[7] Space Exploration Technologies Corp. *Falcon 9 Launch Vehicle Payload User's Guide*. Rev 2.0. SpaceX. Hawthorne, CA, 2020. URL: https://www.spacex.com/media/falcon-users-guide-2021-09.pdf (cit. on p. 7).

[8] European Space Agency. *Chang'e-5 — eoPortal Directory: Satellite Missions*. eoPortal by ESA. [Online; accesso 3-Gennaio-2026]. 2020. URL: https://www.eoportal.org/satellite-missions/chang-e-5#spacecraft (cit. on p. 8).

[9] Jiancheng Cheng, Hao Zhang, Haibin Zhang, Bofeng Bai, and Liang Zhao. "Review of Atomization and Mixing Characteristics of Pintle Injectors". In: *Acta Astronautica* 200 (2022), pp. 400–419. DOI: 10.1016/j.actaastro.2022.08.042 (cit. on pp. 9, 76).

[10] Yibing Chang, Jianjun Zou, Qinglian Li, Peng Cheng, and Kang Zhou. "Numerical Study on Combustion and Heat Transfer of a GOX/GCH4 Pintle Injector". In: *The Proceedings of the 2018 Asia-Pacific International Symposium on Aerospace Technology (APISAT 2018)*. Vol. 459. Lecture Notes in Electrical Engineering. Springer Singapore, 2019, pp. 1806–1825. DOI: 10.1007/978-981-13-3305-7_145. URL: https://doi.org/10.1007/978-981-13-3305-7_145 (cit. on p. 10).

[11] Erin M. Betts and Robert A. Frederick Jr. "A Historical Systems Study of Liquid Rocket Engine Throttling Capabilities". In: *American Institute of Aeronautics and Astronautics (AIAA)*. AIAA Paper. NASA Marshall Space Flight Center; University of Alabama in Huntsville. 2010 (cit. on p. 10).

[12] William R. Jr. Hammock, Eldon C. Currie, and Arlie E. Fisher. *Apollo Experience Report: Descent Propulsion System*. Technical Note NASA TN D-7143. Public domain NASA technical note on the design and performance of the Apollo Lunar Module descent propulsion system. Washington, D.C., USA: National Aeronautics and Space Administration, Mar. 1973. URL: https://ntrs.nasa.gov/citations/19730011150 (cit. on p. 11).

[13] Zhao Yao, Yufeng Qi, Weimin Bao, and Tao Zhang. "Thrust Control Method and Technology of Variable-Thrust Liquid Rocket Engine for Reusable Launch Rocket". In: *Aerospace* 10.1 (2023), p. 32. DOI: 10.3390/aerospace10010032. URL: https://www.mdpi.com/2226-4310/10/1/32 (cit. on pp. 12, 13).

[14] Alan Frew. "TRW-Built Pintle Rocket Engine Promises Lower Launch Costs". In: *SpaceDaily* (2000). URL: https://www.spacedaily.com/news/booster-00d.html (cit. on p. 15).

[15] National Aeronautics and Space Administration. *Apollo 13 Mission Report*. Technical Report NASA-MSC-02680. NASA, 1970. URL: https://www.nasa.gov/wp-content/uploads/static/history/alsj/a13/A13_MissionReport.pdf (cit. on p. 15).

[16] I. A. Klepikov, B. I. Katorgin, and V. K. Chvanov. "The new generation of rocket engines, operating by ecologically safe propellant". In: *Acta Astronautica* 41.4–10 (1997). 48th IAF Congress, pp. 209–217 (cit. on p. 17).

[17] Jihyoung Cha, Erik Andersson, and Alexis Bohlin. "A Numerical Approach to Optimize the Design of a Pintle Injector for LOX/GCH4 Liquid-Propellant Rocket Engine". In: *Aerospace* 10.7 (2023), p. 582. DOI: 10.3390/aerospace10070582. URL: https://doi.org/10.3390/aerospace10070582 (cit. on pp. 17, 18, 21, 22, 33–35, 37, 38, 43, 50–57).

[18] J. V. Mageean. *Space Storage Propellant Performance: Final Report*. Contractor Report NASA-CR-72486. Accession No. 69N27975; Work of the US Government – Public Use Permitted. Redondo Beach, CA, USA: TRW Systems Group, National Aeronautics, and Space Administration, Mar. 1969. URL: https://ntrs.nasa.gov/citations/19690018597 (cit. on pp. 18–20).

[19] Donghyuk Kang, Sanghoon Han, Chulsung Ryu, and Youngsung Ko. "Design of pintle injector using Kerosene–LOx as propellant and solving the problem of pintle tip thermal damage in hot firing test". In: *Acta Astronautica* 201 (2022), pp. 48–58. DOI: 10.1016/j.actaastro.2022.08.029. URL: https://www.sciencedirect.com/science/article/pii/S0094576522004416 (cit. on p. 18).

[20] B. B. Vasques and O. J. Haidn. "Effect of Pintle Injector Element Geometry on Combustion in a Liquid Oxygen/Liquid Methane Rocket Engine". In: *Proceedings of the 7th European Conference for Aeronautics and Space Sciences (EUCASS 2017)*. Conference paper. Milan, Italy, 2017. DOI: 10.13009/EUCASS2017-88. URL: https://www.eucass.eu/doi/EUCASS2017-088.pdf (cit. on pp. 18, 19).

[21] Leandro Lucchese. "Numrerical modeling of sub-critical pressure injection for variable thrust engine with Pintle injector". PhD thesis. Roma, Italy: Sapienza Università di Roma, 2023 (cit. on pp. 19, 20).

[22] Suji Lee, Jaye Koo, and Youngbin Yoon. "Effects of skip distance on the spray characteristics of a pintle injector". In: *Acta Astronautica* 178 (2021), pp. 471–480. DOI: 10.1016/j.actaastro.2020.09.043. URL: https://doi.org/10.1016/j.actaastro.2020.09.043 (cit. on p. 20).

[23] Hobin Ryu, Isang Yu, Wanchan Kim, Donghae Shin, Youngsung Ko, and Seonjin Kim. "Experimental Investigation on Combustion Performance of a Pintle Injector Engine with Double-row Rectangular Slot". In: *Journal of the Korean Society of Propulsion Engineers* 21.3 (2017), pp. 25–33. DOI: 10.6108/KSPE.2017.21.3.025. URL: https://doi.org/10.6108/KSPE.2017.21.3.025 (cit. on p. 21).

[24] Xuan Jin, Yang Yang, Xiaomei Cao, and Jinshui Wu. "Effect of Local Momentum Ratio on Spray Windward Distribution of a Gas–Liquid Pintle Injector Element". In: *Aerospace* 9.9 (2022), p. 494. DOI: 10.3390/aerospace9090494. URL: https://doi.org/10.3390/aerospace9090494 (cit. on p. 22).

[25] George P. Sutton and Oscar Biblarz. *Rocket Propulsion Elements*. 9th ed. Hoboken, NJ, USA: John Wiley & Sons, 2017 (cit. on p. 24).

[26] Pastrone D. and Martelli E. *Endoreattori – Lecture Notes*. Lecture notes, Master's degree course. Unpublished teaching material. 2023 (cit. on p. 24).

[27] Wooseok Song, Juhyun Hwang, and Jaye Koo. "Atomization of gelled kerosene by multi-hole pintle injector for rocket engines". In: *Fuel* 285 (2021), p. 119212. DOI: 10.1016/j.fuel.2020.119212. URL: https://doi.org/10.1016/j.fuel.2020.119212 (cit. on p. 29).

[28] Simone Conti and Alessio Salciccia. "Modellazione CFD in OpenFOAM del processo d'iniezione acqua/urea con formazione ed evaporazione di film liquido a parete per applicazioni SCR". Master's thesis, Corso di Laurea Specialistica in Ingegneria Energetica. MA thesis. Milano, Italy: Politecnico di Milano, 2011.

URL: https://www.politesi.polimi.it/retrieve/a81cb059-fe6e-616b-e053-1605fe0a889a/2012_04_Conti_Salciccia.pdf (cit. on p. 30).

[29] Min Son, Kanmaniraja Radhakrishnan, Jaye Koo, Oh Chae Kwon, and Heuy Dong Kim. "Design Procedure of a Movable Pintle Injector for Liquid Rocket Engines". In: *Journal of Propulsion and Power* 33.4 (2017), pp. 858–869. DOI: 10.2514/1.B36301. URL: https://doi.org/10.2514/1.B36301 (cit. on pp. 30, 32).

[30] D. B. Spalding. "The Combustion of Liquid Fuels". In: *Proceedings of the International Symposium on Combustion, Vol. 4*. Symposium (International) on Combustion. 1953, pp. 847–864. DOI: 10.1016/S0082-0784(53)80110-4. URL: https://doi.org/10.1016/S0082-0784(53)80110-4 (cit. on p. 31).

[31] Yibing Chang, Jianjun Zou, Qinglian Li, Peng Cheng, and K. Zhou. "Numerical Study on Combustion and Heat Transfer of a GOX/GCH4 Pintle Injector". In: *Proceedings of the 2018 Asia-Pacific International Symposium on Aerospace Technology (APISAT 2018)*. Ed. by Editor(s) Unknown. Lecture Notes in Mechanical Engineering. Singapore: Springer, 2019, pp. 1806–1825. DOI: 10.1007/978-981-13-3305-7_145. URL: https://doi.org/10.1007/978-981-13-3305-7_145 (cit. on p. 45).

[32] Vadiraj V. Katti and S. V. Prabhu. "Experimental Study and Theoretical Analysis of Local Heat Transfer Distribution between Smooth Flat Surface and Impinging Air Jet from a Circular Straight Pipe Nozzle". In: *International Journal of Heat and Mass Transfer* 51.17-18 (2008), pp. 4480–4495. DOI: 10.1016/j.ijheatmasstransfer.2007.12.024. URL: https://doi.org/10.1016/j.ijheatmasstransfer.2007.12.024 (cit. on pp. 46, 47).

[33] Lin Chen, Keisuke Asai, Taku Nonomura, Guannan Xi, and Tianshu Liu. "A review of Backward-Facing Step (BFS) flow mechanisms, heat transfer and control". In: *Thermal Science and Engineering Progress* 6 (2018), pp. 194–216. DOI: 10.1016/j.tsep.2018.04.004. URL: https://doi.org/10.1016/j.tsep.2018.04.004 (cit. on p. 47).

[34] Patrick Jenny, Dirk Roekaerts, and Nijso Beishuizen. "Modeling of Turbulent Dilute Spray Combustion". In: *Progress in Energy and Combustion Science* 38.6 (2012), pp. 846–887. ISSN: 0360-1285. DOI: 10.1016/j.pecs.2012.07.001 (cit. on pp. 60, 61, 66–68).

[35] Andrea Ferrero and Leonardo Stumpo. *Dispense di Fluidodinamica Computazionale*. Italian. Materiale didattico universitario. Corso di Fluidodinamica Computazionale. 2024/2025 (cit. on pp. 62, 65, 94).

[36] Zhiyu Han and Rolf D. Reitz. "A Temperature Wall Function Formulation for Variable-Density Turbulent Flows with Application to Engine Convective Heat Transfer Modeling". In: *International Journal of Heat and Mass Transfer* 40.3 (1997), pp. 613–625. DOI: 10.1016/S0017-9310(96)00117-2 (cit. on p. 77).

[37] Brian Bjelde, Max Vozoff, and Gwynne Shotwell. “The Falcon 1 Launch Vehicle: Demonstration Flights, Status, Manifest, and Upgrade Path”. In: *21st Annual AIAA/USU Conference on Small Satellites*. SSC07-III-6. Utah State University. Logan, UT, 2007. URL: https://digitalcommons.usu.edu/smallsat/2007/all2007/23/ (cit. on p. 92).

[38] Håkan Nilsson. *CFD with OpenSource Software: OpenFOAM Course*. Materiale didattico e dispense del corso OpenFOAM. Corso universitario sull’uso di OpenFOAM per la fluidodinamica computazionale. 2022. URL: http://www.tfd.chalmers.se/~hani/kurser/OS_CFD_2022/ (visited on 01/11/2026) (cit. on pp. 95, 96).